TECHNISCHE UNIVERSITÄT MÜNCHEN
LEHRSTUHL FÜR AERODYNAMIK UND STRÖMUNGSMECHANIK

Wall Modeling for Implicit Large-Eddy Simulation

Zhenli Chen

Vollständiger Abdruck der von der Fakultät für Maschinenwesen der Technischen Universität München zur Erlangung des akademischen Grades eines

Doktors-Ingenieurs

genehmigten Dissertation.

Vorsitzender: Univ.-Prof. Dr.-Ing. Horst Baier
Prüfer der Dissertation: 1. Univ.-Prof. Dr.-Ing. Nikolaus A. Adams
                         2. Prof. Dr. Yong Yang,
                            Northwestern Polytechnical University / VR China

Die Dissertation wurde am 24.01.2011 bei der Technischen Universität München eingereicht und durch die Fakultät für Maschinenwesen am 12.04.2011 angenommen.

Zhenli Chen

P.O. box 114, Youyi West Road 127,

Xi'an 710072, Shannxi, China.

zl.chen@mytum.de

Released May 05, 2011

Typesetting LaTeX 2_ε

Abstract

A wall-modeling method is proposed for implicit large-eddy simulation (LES) using an adaptive local deconvolution methods (ALDM), to simulate flows along complex geometries at high Reynolds numbers. The wall-shear stress is employed as approximate boundary condition, resulting in the wall-shear force as a source term in the momentum equations of the exterior LES in the framework of a conservative immersed interface method (CIIM). Three kinds of wall-stress models are investigated in detail for attached and separated flows, including a generalized wall function with pressure correction, an integral form of the Werner and Wengle two-layer power law and a wall-layer model based on the simplified turbulent boundary layer equations (TBLE).

The effect of wall modeling is to compensate the SGS-modeling error, especially in the near-wall cells through the wall-tangential momentum balance, in comparison with a coarse-mesh LES without wall modeling. The SGS-modeling and the wall-modeling errors should be distinguished clearly and should be eliminated/compensated separately. The former is accomplished by using a physically motivated coherent-structures based SGS-modeling parameter instead of the van-Driest damping function, which leads to improved streamwise-momentum balance at high Reynolds numbers. The latter is realized by using a TBLE-based model to account for the wall-layer flow dynamics at very low computational cost.

Secondary flow features are very sensitive to wall-modeling and numerical errors. In the framework of CIIM, LES of exterior flows is insensitive to the modeled wall-shear stress when massive separation occurs, either induced by an abrupt change of wall geometry or by a

strong adverse pressure gradient at a smooth surface. However, it is sensitive to the modeled wall-shear stress when shallow separations at a smooth surface occur, especially in the recovery region. The simulation results can only recover direct numerical simulation (DNS) or resolved LES for increasing grid resolution in a global sense, if the wall model can account for the near-wall flow dynamics. All turbulence states are realizable in wall-modeled LES, and the grid resolution can be evaluated *a posteriori* by spectral analysis of the time sequence of velocity components.

The TBLE based model is superior to the other two wall models concerning its ability to account better for the near-wall flow dynamics. However, its deficiencies can be attributed to dependent on the pressure gradient term due to the omission of nonlinear convective terms. We also confirm a prior finding that only the wall-shear stress is not enough as an approximate boundary condition for exterior LES, even if the wall-shear stress from the DNS is used, but additional turbulence information is required.

With these wall models reasonable results are obtained. The application on a flow over a circular cylinder combined with adaptive mesh refinement (AMR) at very high Reynolds number shows that a proper wall modeling procedure for implicit LES using ALDM in the framework of CIIM and AMR method is a valid simulation tool for practical engineering problems.

Acknowledgements

I really appreciate my mentor Prof. N. A. Adams for giving me a chance as his student. I wish to thank him for his kindness and supports. He has guided me in the region of turbulence investigation and has introduced me from an outdoor man of turbulence to be a turbulence modeler. His deep insights into the relationship between mathematics and physics make a strong impression on me. I am also indebted to Prof. B. Q. Zhang for his encouragements on this work. Many thanks to the chair of the examination committee Prof. H. Baier for his lots of work. And many thanks to my co-examiner Prof. Y. Yang for showing his interest in my work.

I wish to thank all my colleges in Institute of Aerodynamics and Fluid Mechanics, especially Dr. A. Devesa, Dr. S. Hickel, Mr. M. Meyer, Dr. C. Stemmer, Mr. K. K. So and Dr. X. Y. Hu. They offered heartfelt help and showed their kindness when I discussed with them. I will miss the group meeting on Tuesday. I like that kind of discussion environment.

At last, but not least, I would like to thank my family for their everlasting supports and love.

Contents

List of Tables

List of Figures

Nomenclature

Roman Symbols

A face aperture

$\langle u_i u_j \rangle$ component of Reynolds stress tensor

b_{ij} component of anisotropy tensor

C_f local friction coefficient

C_p local pressure coefficient

H length scale, height of half channel, periodic hill or backward-facing step

h bump height

$E(\kappa)$ turbulent kinetic energy density at frequency κ

K maximum order of reconstruction polynomials

k order of reconstruction polynomial

Re_θ Reynolds number based on the momentum thickness

l turbulent length scale

$\mathbf{n}$ outward unit normal vector

$\mathbf{n}_\perp$ immersed interface normal vector

Re_τ Reynolds number based on friction velocity

Re_L Reynolds number based on integral scale

t   wall-tangential vector

t time

u   velocity vector

u_p velocity scale based on pressure gradient

u_τ friction velocity

x   coordinate vector

Greek Symbols

α volume fraction

β smoothness-measure function

δ boundary layer thickness

η Kolmogorov dissipation scale

η variable defined from the second invariant of anisotropy tensor

γ modeling parameter of ALDM

κ frequency

κ von Kármán constant

λ grid shift

$\boldsymbol{\lambda}$ grid shift vector

Γ area of immersed interface

ν kinematic viscosity

ϕ scalar variable

ρ density

σ modeling parameter of ALDM in flux function

$\boldsymbol{\tau}$ subgrid stress

τ shear stress

ξ variable defined from the third invariant of anisotropy tensor

$\boldsymbol{\xi}$ general coordinate

Superscripts

B backward

D downward

$'$ fluctuation

F forward

U leftward

$+$ normalized, frequently for scaling in wall units or friction velocity

D rightward

U upward

Subscripts

o property at the coupling position

N grid function obtained by projecting a continuous function onto a numerical grid

τ based on wall friction

w property at the wall

Other Symbols

$\langle \cdot \rangle$ mean value (Reynolds filter)

$\overline{\cdot}$ convolution operator

$\widehat{\cdot}$ face averaging operation

$\widetilde{\cdot}$ numerical approximation

Acronyms

$ALDM$ Adaptive Local Deconvolution Method

AMR Adaptive Mesh Refinement

CFL Courant-Friedrichs-Lewy number

CG Conjugate Gradient

$CIIM$ Conservative Immersed Interface Method

CS Coherent Structures based damping

DES Detached Eddy Simulation

DNS Direct Numerical Simulation

$EDQNM$ Eddy-Damped Quasinormal Markovian

FFT Fast Fourier Transform

$GWFP$ Generalized Wall Function with Pressure gradient based wall model

IB Immersed Boundary

LES Large-Eddy Simulation

$MDEA$ Modified-Differential Equation Analysis

MPI Message Passing Interface

$RANS$ Reynolds-Averaged Navier-Stokes equations

SGS SubGrid Scale

$TBLE$ Thin Boundary Layer Equations /based wall model

TCF Turbulent Channel Flow

VD Van Driest damping

$WENO$ Weighted Essentially Non Oscillatory

WW Wener-Wengle function based wall model

Chapter 1

Introduction

1.1 Background and motivation

Turbulent flows are encountered in daily life and are very important in practical engineering, where they are crucial for the performance of a system. Such as with the flow over an airplane, the turbulence is responsible for the high friction drag generation, and directly relates to the fuel consumption. On the other hand, the transportation and mixing in a turbulent flow are much more effective than in a comparable laminar flow. The turbulent flow field $\mathbf{u}(\mathbf{x}, t)$ is characterized by its significant and irregular variations both in space $\mathbf{x}$ and time t, and exhibits rich multiple ranges of space and time scales. Statistical methods are traditionally used to describe turbulence. However, turbulence can not be viewed as fully random field, but has an inner structure defined by Navier-Stokes dynamics and boundary conditions. For an incompressible constant-property Newtonian fluid, the Navier-Stokes Equations

$$\frac{\partial \mathbf{u}}{\partial t} + \nabla \cdot (\mathbf{u}\mathbf{u}) = -\frac{1}{\rho}\nabla p + \nu\nabla^2\mathbf{u}, \tag{1.1a}$$

$$\nabla \cdot \mathbf{u} = 0. \tag{1.1b}$$

describe the instantaneous turbulent flow under the continuum hypothesis. Proper initial and boundary data are required for a well-posed problem. Only for very

simple cases there are analytical solutions of these equations. Otherwise, in order to understand, use and control turbulence, numerical methods have to be used to solve them. With these methods, three problems occur concerning the turbulent kinetic energy production and transportation, the anisotropy of the turbulent field representation, and the reduction of the necessary number of degrees of freedom.

In turbulence theory the Kolmogorov hypotheses provide us productive information on the scaling of a series of turbulence scales l which have characteristic velocity scale $u(l)$ and time scale $\tau(l) \equiv l/u(l)$, and quantify Richardson energy cascade [146] at sufficiently high Reynolds number. Based on the local isotropic assumption of small-scale turbulent motions, the smallest dissipation scales are supposed to be uniquely determined by the kinematic viscosity ν and the local mean dissipation rate ε, which results in the Kolmogorov scales

$$\eta \equiv \left(\nu^3/\varepsilon\right)^{1/4}, u(\eta) \equiv (\varepsilon\nu)^{1/4}, \tau(\eta) \equiv (\nu/\varepsilon)^{1/2}, \tag{1.2}$$

where ε is proportional to $(u(l_0))^3/l_0$ and is imposed by the large energy-containing scales l_0 which are proportional to the flow scale L. The ratio of the largest scales and smallest ones L/η is proportional to $Re_L^{3/4}$, where Re_L is Reynolds number based on the flow scale. This ratio indicates the number of degrees of freedom in a certain spatial direction. For the scales $\eta \ll l \ll L$, their statistic is uniquely determined by ε, independent of ν,

$$\begin{aligned}
u(l) &= \quad (\varepsilon l)^{1/3} = u(\eta) \left(l/\eta\right)^{1/3}, \\
\tau(l) &= \left(l^2/\varepsilon\right)^{1/3} = \tau(\eta) \left(l/\eta\right)^{2/3},
\end{aligned} \tag{1.3}$$

which indicate scale similarity. The energy transfer rate from eddies larger than l to those smaller than l can be expected to be order of $(u(l))^2/\tau(l) = \varepsilon$, which is constant through this inertial range. The energy cascade can be summarized as the turbulent kinetic energy is driven from mean flow of rate ε at large scales, then it is transferred at that constant rate through the inertial range by turbulent transport, at last it is dissipated into internal energy by molecular viscosity in the dissipation range. As the time scales in the inertial and dissipation ranges are much shorter than that in the energy-containing range, these small scales adjust themselves almost immediately to the change of the large scales, therefore, they
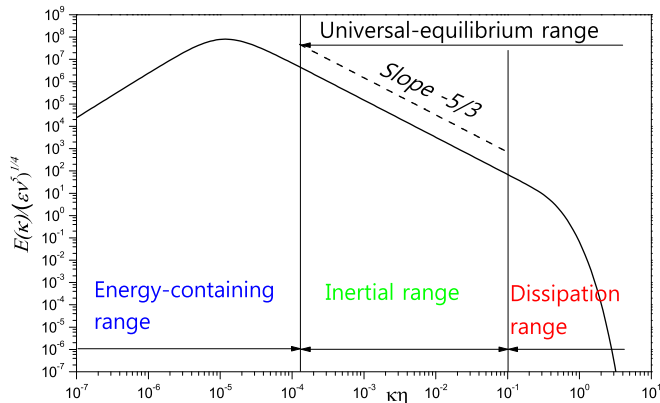
Figure 1.1: Model energy spectrum [143] for isotropic turbulence at $Re_\lambda = 10,000$ normalized by Kolmogorov scales. Solid line: model energy spectrum; dashed line: the line with slope $-5/3$.

can be considered to be in equilibrium. The energy distribution among these three scale ranges using a model energy spectrum in Ref. [143] is sketched in Fig. 1.1 for isotropic turbulence.

1.1.1 Motivation for wall modeling

The Navier-Stokes equations can be solved directly. The energy transfer up to the dissipation range is fully represented, and the anisotropy of the flow can be taken into account on suitably fine grids. Therefore, all turbulence scales are resolved directly without any modeling, consequently this method is called Direct Numerical Simulation (DNS). However, some difficulties are encountered as described in the following.

Since partial derivatives have to be represented numerically, on one hand, special high-order low-dissipation discretization schemes, such as spectral schemes, are required. These high-order numerical schemes are not suitable for complex boundaries and complex geometries. On the other hand, to resolve all the turbulence scales, the discretization grids need to be fine enough to represent all small dynamically important flow structures up to the dissipation scale, and the number of grid points is proportional to $Re_L^{9/4}$ due to the three space directions [143]. The ratio of time scale between largest turbulence structures and the smallest ones is

proportional to $Re_L^{1/2}$, and the use of an explicit time-integration scheme leads to a linear dependency of the time step with respect to the mesh size. Therefore, in order to simulate the flow evaluation on the order of the characteristic time of the largest flow structures, the required total computational resources is proportional to Re_L^3, which is not affordable for high Reynolds numbers according to current computer systems [86].

One alternative to overcome these difficulties is to solve the Reynolds-Averaged Navier-Stokes equations (RANS) for obtaining a statistically averaged flow field, while modeling all turbulence scales by a statistical turbulence model. The turbulent kinetic energy is modeled, and the anisotropy of turbulence scales are also left to the turbulence model. Hence the number of degrees of the freedom is largely reduced and the number of grid points depends only weakly on Re_L. This method is well developed [183] and is widely used in practical engineering.

Most of the statistical turbulence models are of eddy-viscosity type based on the Boussinesq hypothesis, or of second-order-moment-closure type based on Reynolds stress transport equations, which focus on different modeling quantities and spatial information, respectively. For the former, it is very difficult to set length scales and/or turbulent energy dissipation rate. The principle axes of the Reynolds-stress tensor are empirically related to the mean strain-rate tensor, which is only valid for simple shear flows. The latter invokes more consistent models for the physics of turbulence, *e.g.* based on tensor invariants, and especially requires accurate modeling of the pressure-strain rate tensor [57]. Most of this kind of models are calibrated for specific flows, which links their preferred capability to flows of similar kind [80]. Another obvious shortcoming for this kind of method is their inability to account for flows under strong adverse pressure gradient, the process of flow separation and highly unsteady flows, due to its basic modeling and Reynolds average assumptions [80, 83, 115]. Few statistical models can reliably predict even fixed 2D flow separation induced by a sharp corner of a backward-facing step [160].

An intermediate method called Large-Eddy Simulation (LES) has been investigated intensely during last three decades [137, 152], in which only the energy-containing boundary-dependent large structures are resolved directly, while the more universal small scales are left to a model. The separation of large scales from
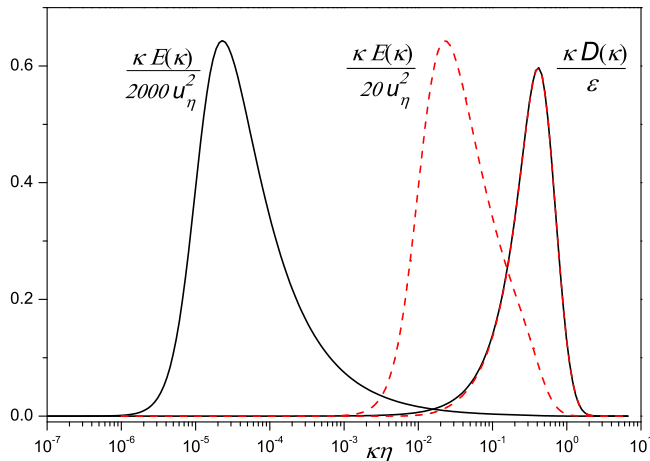
Figure 1.2: Model energy and dissipation spectra [143] for isotropic turbulence. Solid line: $Re_\lambda = 10,000$; dashed line: $Re_\lambda = 100$.

the full scale range is obtained by a low pass filter operating on the Navier-Stokes equations, which leaves the filtered Navier-Stokes equations for large flow scales with subfilter-stress terms. (Mostly filter operations are not carried out explicitly, but by implicit projection onto the background grids and by the discretization scheme, therefore, the subfilter scale is mostly called subgrid scale, and subfilter stresses are called subgrid scale stresses). This low-pass filter operation leads to a large reduction in the number of degrees of freedom due to the filtered-out high-frequency motions. Therefore, a large number of grid points required to resolve the scales below the filter width can be saved compared with DNS.

The subgrid scale (SGS) stress has to be modeled by a SGS model to account for the effect of the subgrid scales on the resolved large scales. The SGS model is expected to be universal for all turbulent flows due to the isotropy and universality of the filtered subgrid scales, when the filter-width is far enough within the inertial range. This expectation is reasonable for flows without wall boundaries at high Reynolds numbers, such as free shear flows and isotropic turbulence, due to the existence of a long inertial range. However, in the wall layer, there is no long inertial range that separates the large energy-containing scales and the small dissipative ones, but there is some overlap between them [77], resembling isotropic turbulence at low Reynolds numbers, as shown in Fig. 1.2.

On the other hand, in the wall layer, the small scales are highly anisotropic and are far from local equilibrium. Therefore, differences between near-wall and isotropic turbulence can not be totally attributed to the low Reynolds number effect, but some dynamically important anisotropic small structures, such as longitudinal streaks [85, 134] with high aspect ratio. They develop in the wall layer and are scaled with wall units. These small scales are responsible for high local energy production and transport. Since these highly anisotropic small structures are beyond the scope of the original concept of LES, and most of the SGS model are based on a homogenous spatial filter, there is no SGS model that can handle reliably the effect of these small scales. To represent them directly, the filter width should be as small as the dissipation scale, which requires the number of grid points to be proportional to Re_τ^2 ($Re_\tau = \delta u_\tau/\nu$ based on the friction velocity u_τ, boundary layer thickness δ and kinematic viscosity ν), approaching the resolution requirement of DNS [8]. This is not affordable at high Reynolds numbers.

In the spirit of LES, when the large scales are well resolved, the statistical variables that are crucial in practical engineering, such as first- and second-order moments of velocities, can be obtained directly from the resolved scales. This means that stress-production events are contained within the large energetic structures or comparable with them, and are well separated from the small dissipative structures, as sketched in Fig. 1.3. This is also not true for wall-bounded turbulence within the wall layer [86], where the near-wall small coherent structures scale with wall units and should be resolved to represent correctly the kinetic-energy production and transportation events. Therefore, the resolution should be high enough to resolve these crucial coherent structures.

To overcome the prohibitive resolution requirement, at high Reynolds numbers, there are generally four ways. First, wall layer resolved LES are carried out on adaptively refined grids by multi-resolution methods [105, 155]. Because it is difficult to construct compact discretization schemes and as it is complicated to measure necessary refinement, this method has limited robustness and grid-point reduction capability. Another alternative is to use a robust SGS model on coarse grids (at least in wall-tangential directions) with the framework of LES. In the simulations no-slip boundary conditions are used without resolved wall layer, by
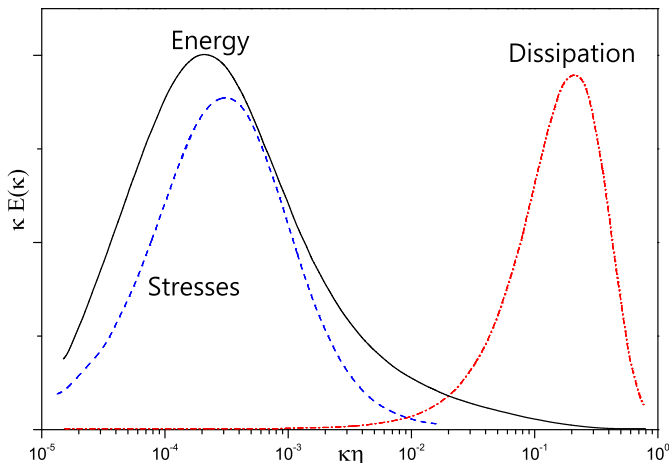
Figure 1.3: Spectra for the turbulent kinetic energy, Reynolds stresses, and dissipation in the logarithmic region of a turbulent boundary layer flow at $Re_\theta = 370,000$ [151]. Solid line: turbulent kinetic energy; dashed line: Reynolds stresses; dashdotted line: dissipation.

which the anisotropy and inhomogeneity of near-wall turbulence enter into the subgrid scales. Therefore, this method requires a very robust SGS model that can account well for the anisotropy of subgrid scale stresses and the production and transport of turbulent kinetic energy [148]. When such dynamically important events are not well resolved, the SGS model depends strongly on the boundary conditions and becomes strongly configuration dependent, similarly as statistical turbulence models for RANS. Although some attempts, *e.g.* very large-eddy simulation [82, 106] inspired from the statistical turbulence modeling have been made, there is no such SGS model well established until now [111, 166]. A third alternative is when a SGS model is used to describe the dynamics of near-wall coherent structures. The simulation is carried out on coarse grids without resolved wall layer. Starting from the information of resolved scales the dynamic process of subgrid scales can be modeled. This requires the deep understanding of wall turbulence and phenomenological descriptions of the near-wall structures, which at the time is still incomplete. The last alternative is to bypass the wall layer with its effect approximated by a wall model [138, 139] or another well established method such as RANS [53], which reduces the wall layer to an approximate wall boundary condition for the exterior LES or a hybrid LES/RANS method, respec-

tively. Here the key issue is what information is required for the exterior LES. Among these alternatives the last one is feasible, and can be based on established near-wall turbulence knowledge. The technical and modeling difficulties are to assess the suitable coupling and information between wall layer and exterior LES.

1.1.2 Knowledge of wall turbulence for wall modeling

Wall turbulence can be described by turbulent boundary layer theory, scaling laws, near-wall coherent structures and the interaction between the wall layer and exterior flows. These subjects are related to wall modeling and are reviewed with main focus on their applicabilities to wall modeling in this subsection.

The boundary layer concept was pioneered by Prandtl [144] under the assumptions that in the very thin wall region the wall-tangential length scales are much larger than the wall-normal ones, and wall-normal derivatives are much larger than the wall-tangential ones at high Reynolds numbers. Since, boundary layer theory has been well developed [153]. In the framework of this theory, laminar and turbulent boundary layer with moderate pressure gradient can be treated until flow separation occurs. Transition from laminar to turbulent flow can not be taken into account without empirical theory. In turbulent boundary layer calculations the Reynolds shear stress should be modeled by a turbulence model for closure of the equations, which limits the capability of this method. For certain reattached boundary layers the flow is far from equilibrium and a secondary near-wall layer develops, for which methods based on mixing-length eddy-viscosity models fail. Nevertheless, this method is widely used in combination with potential method for flow simulations because of its more physical reasonability and high efficiency [31].

With RANS a higher order approximation of the turbulent boundary layer is obtained. As introduced in last section, this method is limited by the available statistical turbulence models. The pressure Poisson equation must be solved within the thin layer, which results in comparably high computational cost.

The turbulent boundary layer under a mild pressure gradient can be separated into viscous sublayer, buffer layer, logarithmic layer and wake region [143]. There are scaling laws for the mean streamwise velocity within the viscous sublayer,

logarithmic layer and wake region, the law of the wall, the logarithmic law, and the wake-defect law, respectively. These laws are deduced using asymptotical analysis and empirical correlations. Therefore, there is no a closed formulation that can represent the mean velocity of the entire boundary layer. The buffer layer can be formulated as smooth transition from sublayer to the logarithmic layer using a single formulation [165], or be omitted using only a two-layer power law [182]. There is still some debate on the validity of the standard logarithmic law [22, 59]. Several generalized wall functions have been constructed and applied in RANS computation [156, 179]. Although there are scaling laws for the mean velocity profile of separated flows [159], they are still under debate [5, 112]. The laws for attached boundary layers under mild pressure gradients can be adopted as wall functions to calculate the wall-shear stress using the mean velocity within the logarithmic region, especially in statistical turbulence models to avoid excessive grid resolution [92, 124] in the wall-normal direction. The scaling laws for separated boundary layer are rarely used as wall functions [94].

Besides asymptotical analyses near-wall coherent structures are subject of research to understand the dynamics of near-wall turbulence [134]. Although structures such as longitudinal streaks are well established, their self-sustaining mechanism is not fully understood. Modeling of sublayer streaks has been accomplished with some encouraging results [29]. Based on self-sustaining coherent structures, it can be expected that the near-wall layer is autonomous and is only weakly affected by the footprint of the large scales in the outer layer [28, 87, 88]. It is found, however, that this dependence becomes stronger when the Reynolds number increases [79, 118]. These particular characteristics of the wall layer constitute the basis of the wall-layer modeling.

The buffer layer, where most of streamwise streaks are located, can be viewed as the motor of wall turbulence [116] as most of the turbulent kinetic energy is produced there. Some part of turbulent kinetic energy is dissipated locally, but most is transported both to the wall by diffusion and away from the wall through the logarithmic region. The outward transport sustains the turbulence of the exterior flow. The net energy transport in the buffer layer is from the small scales to the large scales, which is called backscatter.

From the above analysis, a feasible way to construct a wall model for LES

is based on classical methods, such as boundary layer theory, laws of the mean velocity and RANS. Although detailed physics of the wall layer can be obtained by DNS, wall-resolved LES or experiments [52, 108], it needs to be assessed what information can be directly incorporated in a wall model [19, 20], which will be discussed in the next section.

1.2 Wall modeling for LES

Three points are discussed in this section. The first one is what the problem is encountered in the coarse LES of wall-bounded flows and what should be focused on. The second one is what information the exterior LES requires and what a wall model can supply. Finally wall models are reviewed.

1.2.1 Coarse LES

When only the exterior flow is resolved, the grid size is based on the outer length scale δ (boundary layer thickness), and the grid resolution is weakly dependent on the Reynolds number as $Re_L^{0.4}$ [32, 139]. Since in the wall layer the length scales decrease dramatically as the wall is approached, the near-wall grid size is so large that it can be interpreted as an ensemble average. Therefore, it is appropriate to consider the near-wall turbulence in a statistical sense.

When LES are implemented on coarse grids without resolved wall layer, errors arise from numerical discretization and SGS modeling. On one hand, the velocity gradient is large in the near-wall region, and it is under predicted by a discretization scheme using no-slip boundary conditions on coarse grids, which leads to an underestimation of the wall-shear stress and incorrect kinetic energy production, and distorts the exterior LES. On the other hand, the SGS model cannot account for the near-wall anisotropic turbulence and cannot model the correct dissipation.

1.2.2 Information supplied by a wall model

A question arises naturally as to what kind of information is enough for the coarse LES of the exterior flow. For the synthetic boundary conditions shifted to

a plane away from the wall, proposed by Baggett [6], Dirichlet velocity boundary conditions are sufficient for an accurate exterior flow, however the imposed velocity needs to have correct spectral distributions of auto- and cross-correlations. Investigations of Nicoud *et al.* [129] and Jiménez *et al.* [89] confirm that some information of near-wall turbulence structures needs to be passed to the exterior flow. Although this condition is better than the mixed boundary condition with transpiration velocity and wall-normal gradients of the horizontal velocities, in practice it is very difficult to generate accurate velocities with these turbulence structures. Therefore, the wall stress is widely used as an option, as it leads to simple and robust synthetic boundary data. As boundary conditions one commonly imposes the wall-parallel stress components, while the wall-normal velocity component is set to zero.

Cabot [25] has used instantaneous accurate wall stresses as approximate wall boundary condition in the simulation of flow over a backward-facing step, however the result for the exterior flow is not better than that using wall stresses supplied by the Thin Boundary Layer Equations (TBLE). The SGS modeling errors and numerical errors on the coarse mesh are supposed to be responsible for some of the modeling failures, which is often overlooked in the framework of wall modeling [138] . Even in the simulation of canonical plane Turbulent Channel Flow (TCF), the effect of numerical errors can be so significant that the logarithmic velocity profile is not well predicted by algebraic or TBLE based wall-stress models, especially at high Reynolds numbers [26, 27, 128]. By the contamination due to these errors an artificial layer develops in several near-wall cells, which makes the velocity away from these cells under-predicted.

In the work of Medic [119] the near-wall model consists of imposing wall stress and an eddy viscosity and is investigated on turbulent channel flow. The eddy viscosity is obtained from an averaged LES velocity profile and is tabulated for instantaneous usage. Improved mean velocities are obtained using this wall model compared with that of just using wall stress as boundary conditions. A further improvement is obtained with a corrected eddy viscosity using the resolved turbulent stress. This also shows that just the wall-shear stress is not sufficient information for coarse LES. What is learned from these investigations is in the following. First, numerical and modeling errors should be reduced in the near-wall

region or compensated by other methods [128, 172, 173]. Second, it is not feasible to adopt Dirichlet velocity boundary with correct turbulent information, rather one should impose the wall stress with zero transpiration velocity as approximate boundary condition, although even that does not appear to be sufficient.

1.2.3   Review of wall models

In this subsection, wall stress model, hybrid LES/RANS method and some specific near-wall treatments are reviewed.

1.2.3.1   Wall-stress models

Generally a wall stress model can be written as

$$\boldsymbol{\tau}_w = f(\mathbf{u}_o, p_o, \nu, \mathbf{x_o}), \tag{1.4}$$

where f is used to relate the wall stresses in wall-tangential directions to the velocity $\mathbf{u_o}$ and the pressure p_o of the exterior flow at the coupling position $\mathbf{x_o} = (x_{1o}, x_{2o}, x_{3o})$. f can be an algebraic function such as a logarithmic law, or a differential equations such as the thin boundary layer equation with a simple algebraic turbulence model, or even RANS with various turbulence models, solved on embedded grids. Even an experiment was set up to search for the relationship Eq. 1.4 between the instantaneous wall-shear stress and streamwise velocities [147].

When algebraic functions are used to relate the wall stresses to the exterior flow parameters, there are several ways according to classical turbulent boundary layer theory. In the pioneering work of Schumann [154], the wall stresses were related to the instantaneous exterior velocities at first off-wall grid point

$$\tau_{w12}(x_1, x_3) = \frac{u_1(x_1, x_{2o}, x_3)}{\langle u_1(x_1, x_{2o}, x_3)\rangle} \langle \tau_{w12}\rangle,$$

$$u_{w2} = 0,$$

$$\tau_{w32}(x_1, x_3) = \frac{2}{Re_\tau} \frac{u_3(x_1, x_{2o}, x_3)}{x_{2o}}, \tag{1.5}$$

where $\langle \cdot \rangle$ is some type of averaging operation, and $\langle \tau_{w12} \rangle$ should be known *a priori*, as in plane turbulent channel flow driven by a known pressure gradient. This mean wall stress can be obtained using the logarithmic law [65] or by *a priori* RANS calculation [184]. Piomelli *et al* [142] suggested an improvement to this model by shifted correlation based on the observation that the correlation between the wall-shear stress and the velocity increases when a relaxation time is considered. While this formulation and its extensions are only effective for attached boundary layers in approximate equilibrium, for separated and non-equilibrium flows it does not perform well [10, 181].

The logarithmic law can be adopted directly to calculate the instantaneous wall stress using the exterior velocity without the mean operation discussed above. Werner and Wengle proposed a model based on a power law of the mean velocity profile and the instantaneous tangential velocities are associated with wall-shear stresses directly [182]. For separated flows, the wall-shear stress can also be related to the maximum backflow velocity [160] by an algebraic function.

To include more physics in the wall modeling the thin boundary layer equations can be adopted to relate the wall stress to the exterior flow parameters. These equations are written as

$$\frac{\partial}{\partial x_2}(\nu + \nu_t)\frac{\partial \overline{u}_i}{\partial x_2} \;=\; \frac{\partial \overline{u}_i}{\partial t} + \frac{1}{\rho}\frac{\partial \overline{p}}{\partial x_i} + \frac{\partial \overline{u}_i \overline{u}_j}{\partial x_j}, \quad (i = 1,3; j = i,2), \qquad (1.6)$$

where $(\bar{\cdot})$ denotes the averaging operation, x_2 is the wall-normal coordinate, and $x_i(i = 1,3)$ are wall-tangential coordinates. The mixing-length eddy-viscosity model with a damping function is adopted which accounts for near-wall turbulence

$$\nu_t \;=\; \kappa x_2 u_\tau (1 - e^{-x_2^+/A})^2, \qquad (1.7)$$

where $\kappa = 0.4$, $A = 19.0$ and $x_2^+ = x_2 u_\tau/\nu$. The wall-normal velocity can be obtained from the continuity equation as

$$\overline{v}_2(x_1, x_2, x_3) \;=\; -\int_0^{x_2} \left(\frac{\partial \overline{u}_1}{\partial x_1} + \frac{\partial \overline{u}_3}{\partial x_3}\right) dx_2' \;. \qquad (1.8)$$

These equations are solved on embedded grids all the way down to the wall, to obtain the gradients of the tangential velocities in the wall-normal direction. No-slip boundary conditions are used at the wall, and the outer boundary conditions are predicted by the exterior LES. The computational savings come from avoiding solving the pressure Poisson equation within the near wall region, and from the coarse grids in the wall-tangential directions. However, if the convective terms are retained, an iterative solver needs to be used. In order to resolve the wall-normal velocity gradient, the first off-wall grid points must have a small wall distance in wall units, typically of the order unity. If geometric grid stretching is used the number of grid points is proportional to $log(Re_\tau)$ [131], which is weakly dependent on the Reynolds number. This approach was investigated in detail by Cabot [23, 24] to find out the relative importance of terms in TBLE of the backward-facing step flow. The results suggest that the separation and reattachment regions are very sensitive to the near-wall balance between pressure gradients and advection terms in the sublayer. Similar methods without using right hand of Eq. 1.6 and only keeping the pressure gradient are applied to a flow over an asymmetric trailing edge with separation [181]. Improved results are reported compared to algebraic function based models, especially near the small separation zone. From canonical attached plane turbulent channel flow to separation on a 3D axisymmetric hill [176] this method has performed well for a reasonably wide range of flows. Note that RANS can also be used to provide the wall-shear stress for coarse LES as approximately boundary conditions, however, there is no usage of this method reported in literature.

To compensate unknown numerical and SGS modeling errors in coarse LES a wall model based on the suboptimal control theory is constructed to supply an optimized wall-shear stress for exterior flow simulations [128, 172, 173]. The resulting wall-shear stress is of no physical meaning but rather a numerical value to drive the exterior mean velocity to a desired distribution. Although improved results are obtained, this method is limited by its additional computational cost and the requirement of *a priori* mean velocity to generate the desired cost function.

1.2.3.2   Hybrid LES/RANS

This group of methods is based on the idea that using RANS to simulate the near-wall region and LES in the exterior region on a single mesh and is called hybrid LES/RANS [53] or Detached Eddy Simulation (DES) [163] (In some literatures, these two methods are defined differently depending on the turbulence model adopted and the region simulated by RANS). The wall-tangential grid sizes are determined by the resolution requirement of exterior LES, and the number of wall-normal grids required by RANS to resolve the wall-normal velocity gradient is proportional to $log(Re_\tau)$ with grid stretching. But its computational cost is much higher than the TBLE based wall stress model as the full evolution equations must be solved all the way down to the wall. An advantage of this kind of method is the possibility to adopt different turbulence models in different RANS and LES regions. This means that proper turbulence models can be chosen in different regions when approaching the wall. In theory this method could provide accurate results for a wide range of flows, as the range of applicability is determined by the specific turbulence models used. In practice most studies have shown that the results are significantly improved compared to simulations without any near-wall modeling on similar coarse grids, especially for separated flows. But the skin friction is consistently underpredicted by around 10-15% for attached boundary layers [131, 141], which is caused by the interface mismatch between the RANS and LES zones. There are artificial structures so called 'superstreaks' generated. From several investigations [7, 41, 67, 141, 169, 177], it can be concluded that such unphysical structures are typical feature of hybrid LES/RANS methods. Although this problem was mitigated by using stochastic forcing [97, 141], the results are very sensitive to the forcing term. In author's opinion, this is caused by the inconsistent turbulence modeling methodology and by the fact that the velocity requirement of correct spectral distributions of auto- and cross-correlations can not be satisfied at the interface.

1.2.3.3   Other specific treatments

There are some other wall-modeling methods based on the DNS or highly resolved LES for specific flows [19], which are not generally applicable. An alternative

approach employing approximation theory, such as the filtered representation of the boundary condition [15], has led to considerable new insight but has not yet resulted in practically useful wall models.

1.3 Objectives

So far, wall models are almost exclusively used in combination with explicit subgrid-scale models and on body-conforming structured grids limited by the contamination of numerical and modeling errors. A notable exception to the former observation is the work of Grinstein and Fureby, see [63]. However, on one hand, a detailed investigation of wall models within the framework of implicit LES has not yet been performed, where the SGS model is functioned implicitly by the truncation error of discretization schemes [64]. On the other hand, these wall models are constrained to body-fitted grids. There are a very few works [37, 40, 149, 175] focusing on the wall modeling for LES in the framework of Immersed Boundary (IB) methods to overcome this difficulty, despite the fact that IB methods are rather well established [81, 123]. All existing works use explicit SGS models and have adopted the discrete-forcing method [49, 125] using local velocity reconstruction and finite difference methods. This method cannot ensure mass conservation near the IB, although this is crucial for viscous flow prediction [95, 96, 99]. It is found that a large extent of flow field is affected by the loss of mass conservation near the IB [96]. This influence becomes severe at high Reynolds numbers, because the boundary layers tend to be very thin and the inaccuracies introduced at the IB can completely modify the flow development. Therefore, the main objective is to construct a wall modeling methodology for the implicit LES in the framework of a Conservative Immersed Interface Method (CIIM) at high Reynolds numbers on complex geometries towards practical engineering applications. With implicit LES the truncation error functions as implicit SGS model. Here the Adaptive Local Deconvolution Method (ALDM) [3], based on the approximate deconvolution concept [168] is used. CIIM is used to deal with complex geometries and can ensure the discrete conservation of mass and momentum [121]. Local grid refinement is accomplished using Adaptive Mesh Refinement (AMR) method.

The main objectives and accomplishments are:

a. A wall modeling framework for implicit LES is established on body-conforming
grids. Two wall functions and a simplified TBLE based wall-layer model
are used to supply the wall-shear stress to exterior implicit LES as approx-
imated boundary conditions. The near-wall SGS-modeling errors of coarse
LES and wall-modeling errors are distinguished and investigated in detail
on canonical plane turbulent channel flows at very high Reynolds numbers.
A method to compensate or eliminate SGS-modeling errors is promoted.
The characteristics of different wall models are emphasized. In order to
know the capability of different wall models to represent separated flows,
they are assessed for a flow along a backward-facing step, where a separated
bubble is induced by the sharp corner.

b. A wall modeling method within the framework of CIIM is proposed to deal
with complex geometries. Three wall models are adopted to calculate the
wall-shear force as a source term in the momentum equations and to supply
the exterior LES with an approximate boundary condition. First, they
are validated with plane turbulent channel flow and the backward-facing
step flow, and are compared with the cases on the body-conforming grids.
Then the wall models are applied to different separated flows, including a
bump with shallow separation, and a periodic hill with massive separation.
At last, the wall modeling methodology is applied to a flow over a circular
cylinder in the framework of adaptive mesh refinement method at very high
Reynolds number $Re_D = 1.0 \times 10^6$, to show its potential as a simulation
tool for practical engineering.

Chapter 2

Implicit LES using ALDM and CIIM

First, the mathematic framework of LES is introduced, then the motivation of implicit subgrid-scale (SGS) modeling is analyzed, and the construction of ALDM is described in detail. In the following sections, immersed boundary methods are reviewed briefly, and the associated difficulties are highlighted. To apply ALDM to complex geometries, a conservative immersed interface method (CIIM) has been developed and is presented in detail. An adaptive mesh refinement method (AMR) is outlined which allows to overcome the difficulty of local grid refinement. At last the formulations of boundary conditions are described.

2.1 Implicit LES using ALDM

2.1.1 Motivation of implicit SGS modeling

2.1.1.1 Conventional explicit SGS modeling

SGS modeling is based on the separation of a flow variable $\phi(\mathbf{x}, t)$ into a large-scale resolved part $\overline{\phi}(\mathbf{x}, t)$ and a small-scale residual part $\phi^{'}(\mathbf{x}, t)$ by a spatial

convolution filter $\mathbf{G}(\mathbf{x})$,

$$\phi(\mathbf{x}, t) = \overline{\phi}(\mathbf{x}, t) + \phi^{'}(\mathbf{x}, t), \tag{2.1}$$

$$\overline{\phi}(\mathbf{x}, t) = \int_{-\infty}^{+\infty} \phi(\boldsymbol{\xi}, t)\mathbf{G}(\mathbf{x} - \boldsymbol{\xi})d^3\boldsymbol{\xi}. \tag{2.2}$$

To obtain the governing equations of the resolved flow quantities, convolution filter is applied to the Navier-Stokes equations, Eqs. 1.1. The following filtered equations are obtained

$$\frac{\partial \overline{\mathbf{u}}}{\partial t} + \nabla \cdot (\overline{\mathbf{u}\mathbf{u}}) = -\frac{1}{\rho}\nabla\overline{p} + \nu\nabla^2\overline{\mathbf{u}}, \tag{2.3a}$$

$$\nabla \cdot \overline{\mathbf{u}} = 0. \tag{2.3b}$$

The non-linear term $\overline{\mathbf{u}\mathbf{u}}$ in the momentum equations is not expressed as a function of the resolved velocity $\overline{\mathbf{u}}$, which makes these equations unclosed. A subgrid stress $\boldsymbol{\tau}$ can be introduced into the momentum equation as

$$\boldsymbol{\tau} = \overline{\mathbf{u}\mathbf{u}} - g(\overline{\mathbf{u}}), \tag{2.4}$$

which requires modeling, where the function $g(\overline{\mathbf{u}})$ is defined on the filtered velocity. Mostly, the relation $g(\overline{\mathbf{u}}) = \overline{\mathbf{u}}\,\overline{\mathbf{u}}$ is used, and the momentum equation Eq. 2.3a becomes

$$\frac{\partial \overline{\mathbf{u}}}{\partial t} + \nabla \cdot (\overline{\mathbf{u}}\,\overline{\mathbf{u}}) = -\frac{1}{\rho}\nabla\overline{p} + \nu\nabla^2\overline{\mathbf{u}} - \nabla \cdot \boldsymbol{\tau}. \tag{2.5}$$

Most SGS models are based on this framework, assume isotropic spatial filter (*i.e.* G only depends on $|\mathbf{x} - \boldsymbol{\xi}|$) and uniform Cartesian coordinates. However, in practice, inhomogeneous flows are always simulated on non-uniform grids on a bounded computational domain. Inhomogeneous spatial filters arise at the boundaries so that commutation errors between filter and derivative operation can not be neglected [61]. An alternative non-uniform filter that can be applied to an arbitrary computational domain has been proposed in Ref. [61]. Well-defined filters commute with the derivative to second order in space. Higher-order commutative filters are analyzed by Van der Ven [43], and this analysis has been

generalized by Vasilyev *et al.* [180]. Although these methods result in high order commuting filters, they are rarely used in practice.

The explicit modeling paradigm is mainly followed in SGS model development for LES, where an explicit model expression is performed to the unclosed term $\nabla \cdot \boldsymbol{\tau}$ or $\boldsymbol{\tau}$. For this purpose functional or structural approaches can be used. The former follows resolved energy-transfer consideration based on the knowledge about the interaction of resolved scales and subgrid scales, leading *e.g.* to eddy-viscosity models. With the latter one tries to reproduce the eigenvectors of the statistical correlation tensors of the subgrid modes based on some assumptions about the subgrid structures, leading *e.g.* to scale-similarity models [152].

2.1.1.2   Contamination by discretization errors

With the explicit SGS modeling paradigm a presumption is that the associated numerical errors are small compared to the contribution of the explicit SGS model. However, in practice the significant numerical errors contaminate the effect of explicit SGS modeling terms, especially at high wavenumbers. The most important contamination is due to the spatial-truncation error [38, 60, 104]. This situation can not be improved by increasing the grid resolution as long as DNS resolution is not reached, because the errors can increase faster than the subgrid terms when no explicit filtering is used [60]. An explicit filter operation with a proper filter to grid width ratio or high order discretzation schemes can be used to diminish these errors. The required filter to grid ratio results in a substantial increase of computational cost for explicitly filtered LES. In practice, it is hard to use the high-order discretization scheme for simulations of flow along complex geometries. However, numerical errors can be exploited as an implicit SGS model. This approach is proposed by Boris *et al.* [16] using nonlinearly stable schemes and it is presented in Ref. [64].

An important theoretical tool to exploit the interference between truncation error and SGS model is the Modified-Differential Equation Analysis (MDEA) method. Using Taylor series expansions of the solution, MDEA allows to analyze the relation between the implicit model and a given explicit SGS model [3, 54]. However, it becomes tedious when MDEA is used to analyze more complicated

nonlinear discretization schemes of nonlinear three-dimensional differential equations. An alternative using an effective spectral eddy viscosity concept proposed by Domaradzki *et al.* [44] can match numerical dissipation to a given explicit SGS model or to theoretical models. However, most of the implicit SGS models are using discretization schemes off-the-shelf by *a posteriori* validation. Without strict physical motivation, implicit SGS models have been considered as inferior to explicit models by construction, since SGS dissipation is generated essentially by a nonlinear numerical stabilization mechanisms, such as that provided by shock-capturing schemes. It has been shown by Garnier *et al.* [56] that a straightforward application of shock-capturing schemes for implicit LES does not lead to satisfactory results in general. Despite theoretical limitations, in practice, however, often good results with such implicit SGS models have been obtained [46, 54, 55, 63, 66].

A systematic approach for a general, nonlinear-discretization framework that allows for physically motivated implicit SGS modeling, has been introduced by Adams *et al.* [3], based on the approximate deconvolution concept [168]. It has been developed for solving three-dimensional Navier-Stokes equations by ALDM. ALDM is nonlinear and solution adaptive and incorporates a physically motivated implicit SGS model [71].

2.1.2   Adaptive Local Deconvolution Method

The adaptive local deconvolution method (ALDM) is based on a nonlinear deconvolution operator and a numerical flux function which are formulated such that the truncation error functions as an implicit SGS model [71]. In this method, the filtering operation is not performed explicitly, but by using a finite-volume discretization as a top-hat filter on the background staggered Cartesian mesh. The filter can be written as

$$\mathbf{G}(\mathbf{x}_{i,j,k}, \mathbf{x}) = \frac{1}{\Delta x_i \Delta y_j \Delta z_k} \begin{cases} 1, & \text{if } (\mathbf{x}_{i,j,k} + \mathbf{x}) \in \mathbf{I}_{i,j,k}, \\ 0, & \text{otherwise}, \end{cases} \quad (2.6)$$

where a computational cell is

$$\mathbf{I}_{i,j,k} = [x_{i-\frac{1}{2}}, x_{i+\frac{1}{2}}] \times [y_{j-\frac{1}{2}}, y_{j+\frac{1}{2}}] \times [z_{k-\frac{1}{2}}, z_{k+\frac{1}{2}}], \tag{2.7}$$

and Δx_i, Δy_j and Δz_k are the widths of the cell in three coordinate directions. This filter returns a cell average of a function

$$\overline{\varphi}(\mathbf{x}_{i,j,k}, t) = \frac{1}{\Delta x_i \Delta y_j \Delta z_k} \iiint_{\mathbf{I}_{i,j,k}} \varphi(\mathbf{x}_{i,j,k} - \mathbf{x}, t) d\mathbf{x}. \tag{2.8}$$

When this filter is applied to Eqs. 1.1, the governing equations of the resolved velocity are obtained as

$$\frac{\partial \overline{\mathbf{u}}_{i,j,k}}{\partial t} + \mathbf{G}(\mathbf{x}_{i,j,k}, \mathbf{x}) * (\nabla \cdot \mathbf{F}(\mathbf{u})) - \nu \nabla^2 (\overline{\mathbf{u}}_{i,j,k}) + \nabla \overline{p}_{i,j,k} = \mathbf{0}, \tag{2.9a}$$

$$\nabla \cdot \overline{\mathbf{u}}_{i,j,k} = 0, \tag{2.9b}$$

where $\mathbf{F}(\mathbf{u}) = \mathbf{u}\mathbf{u}$ is the convective flux. Since the unfiltered velocity $\mathbf{u}$ is unknown, these equations are not closed. Using the deconvolved velocity $\mathbf{u_N} = \mathbf{G}^{-1} * \overline{\mathbf{u}}_\mathbf{N}$ to approximate the unfiltered velocity $\mathbf{u}$ in Eq. 2.9a results in

$$\frac{\partial \overline{\mathbf{u}}_{i,j,k}}{\partial t} + \mathbf{G}(\mathbf{x}_{i,j,k}, \mathbf{x}) * (\nabla \cdot \mathbf{F}(\mathbf{u_N})) - \nu \nabla^2 (\overline{\mathbf{u}}_{i,j,k}) + \nabla \overline{p}_{i,j,k} = \mathbf{G}(\mathbf{x}_{i,j,k}, \mathbf{x}) * (\nabla \cdot \boldsymbol{\tau}_{SGS}), \tag{2.10}$$

where N indicates the grid functions obtained by projecting continuous functions onto the numerical grid, and the subgrid stress is $\boldsymbol{\tau}_{SGS} = \mathbf{F}(\mathbf{u_N}) - \mathbf{F}(\mathbf{u})$. The subgrid stress is $\boldsymbol{\tau}_{SGS} \neq \mathbf{0}$, because the non-represented scales cannot be recovered by soft deconvolution. With ALDM the explicit modeling of this term is avoided by the following construction. First, the volume integral of $\mathbf{G}$ is evaluated using Gauss' and Green's theorems, then the nonlinear term can be written as

$$\mathbf{G}(\mathbf{x}_{i,j,k}, \mathbf{x}) * (\nabla \cdot \mathbf{F}(\mathbf{u_N})) = \frac{1}{V_{i,j,k}} \iint_{\partial \mathbf{I}_{i,j,k}} \mathbf{n} \cdot \mathbf{F}(\mathbf{u_N}) dS, \tag{2.11}$$

where $\mathbf{n}$ is the outward unit normal vector on the cell faces, $V_{i,j,k} = \Delta x_i \Delta y_j \Delta z_k$ is the control volume, $\partial \mathbf{I}_{i,j,k}$ is the boundary of the control volume. To evaluate

this integral, one has to define the average of the flux over the cell face at the face center. Denote $\mathbf{F} = [\mathbf{f}^1, \mathbf{f}^2, \mathbf{f}^3]$, and the face-averaged flux $\widehat{\mathbf{F}} = [\widehat{\mathbf{f}^1}, \widehat{\mathbf{f}^2}, \widehat{\mathbf{f}^3}]$, where the operation $(\widehat{\cdot})$ indicates the face average. The numerical computation of $\mathbf{f}^l$ ($l = 1, 2, 3$) involves approximations, which are explained on the example of the flux in x-direction

$$\widehat{\mathbf{f}^1}(x_{i+\frac{1}{2}}, y_j, z_k) = \frac{1}{\Delta y \Delta z} \int_{y_{j-\frac{1}{2}}}^{y_{j+\frac{1}{2}}} \int_{z_{k-\frac{1}{2}}}^{z_{k+\frac{1}{2}}} \mathbf{f}^1(x_{i+\frac{1}{2}}, y, z) dy dz. \qquad (2.12)$$

This integral can be computed numerically using a Gaussian quadrature rule with $(2m + 1)^2$ numerical integration points,

$$\widehat{\mathbf{f}^1}(x_{i+\frac{1}{2}}, y_j, z_k) \approx \sum_{\alpha=1}^{2m+1} \sum_{\beta=1}^{2m+1} C_{\alpha\beta} \mathbf{f}^1(x_{i+\frac{1}{2}}, y_{j+\alpha-m}, z_{k+\beta-m}). \qquad (2.13)$$

With 3^2 nodes it reduces to two different integration schemes, the corresponding coefficient matrixes are

$$\mathbf{C_2} = \begin{bmatrix} 0 & 0 & 0 \\ 0 & 1 & 0 \\ 0 & 0 & 0 \end{bmatrix} \quad \text{and} \quad \mathbf{C_4} = \begin{bmatrix} 0 & 1 & 0 \\ 1 & 20 & 1 \\ 0 & 1 & 0 \end{bmatrix}. \qquad (2.14)$$

The coefficient matrix $\mathbf{C_2}$ yields a second-order accurate solution on equidistant grids, and the coefficient matrix $\mathbf{C_4}$ leads to a fourth-order integration scheme.

Second, since an exact inverse filter operation is ill-posed, a solution adaptive deconvolution scheme $\widetilde{\mathbf{G}}^{-1}$ is designed to approximate $\mathbf{G}^{-1}$, which results in the approximately deconvolved velocity $\widetilde{\mathbf{u}}_\mathbf{N} = \widetilde{\mathbf{G}}^{-1} * \overline{\mathbf{u}}_\mathbf{N}$ used in numerical flux computation. At last, a modified Lax-Fridriches flux function $\widetilde{\mathbf{F}}_N$ is adopted to approximate the physical flux function $\mathbf{F}$. The Eq. 2.10 becomes

$$\frac{\partial \overline{\mathbf{u}}_{i,j,k}}{\partial t} + \frac{1}{V_{i,j,k}} \sum_{\partial \mathbf{I}_{i,j,k}} \widehat{\widetilde{\mathbf{F}}}_\mathbf{N}(\widetilde{\mathbf{u}}_\mathbf{N}) \cdot \mathbf{n} \Delta S - \nu \nabla^2(\overline{\mathbf{u}}_{i,j,k}) + \nabla \overline{p}_{i,j,k} =$$

$$\mathbf{G}(\mathbf{x}_{i,j,k}, \mathbf{x}) * (\nabla \cdot \boldsymbol{\tau}_{SGS}) - \boldsymbol{\epsilon}_{i,j,k}^{num}, \qquad (2.15)$$

where the numerical errors

$$\boldsymbol{\epsilon}_{i,j,k}^{num} = \mathbf{G}(\mathbf{x}_{i,j,k}, \mathbf{x}) * (\nabla \cdot \mathbf{F}(\mathbf{u_N})) - \frac{1}{V_{i,j,k}} \sum_{\partial \mathbf{I}_{i,j,k}} \widehat{\widetilde{\mathbf{F}}}_{\mathbf{N}}(\widetilde{\mathbf{u}}_\mathbf{N}) \cdot \mathbf{n} \Delta S \qquad (2.16)$$

are expected to function as an implicit SGS model. ΔS is the cell-face area. The discretized equations then become

$$\frac{\partial \overline{\mathbf{u}}_{i,j,k}}{\partial t} + \frac{1}{V_{i,j,k}} \sum_{\partial \mathbf{I}_{i,j,k}} \widehat{\widetilde{\mathbf{F}}}_{\mathbf{N}}(\widetilde{\mathbf{u}}_\mathbf{N}) \cdot \mathbf{n} \Delta S - \nu \nabla^2(\overline{\mathbf{u}}_{i,j,k}) + \nabla \overline{p}_{i,j,k} = \mathbf{0}, \qquad (2.17a)$$

$$\nabla \cdot \overline{\mathbf{u}}_{i,j,k} = 0. \qquad (2.17b)$$

The numerical discretization and the SGS model are merged entirely.

The approximated deconvolved velocity $\widetilde{\mathbf{u}}_\mathbf{N} = \widetilde{\mathbf{G}}^{-1} * \overline{\mathbf{u}}_\mathbf{N}$ is computed locally by a solution-adaptive combination of deconvolution polynomials, which is inspired by the idea of the Weighted-Essentially-Non-Oscillatory (WENO) scheme [158]. And the deconvolution operator can be decomposed as successive deconvolution in three directions

$$\widetilde{\mathbf{G}}^{-1}(\mathbf{x}) = \widetilde{\mathbf{G}}_x^{-1}(x) * \widetilde{\mathbf{G}}_y^{-1}(y) * \widetilde{\mathbf{G}}_z^{-1}(z). \qquad (2.18)$$

The adaptive local deconvolution of the solution is obtained at the left and right cell faces and at the cell centers, *e.g.* in x direction as

$$\widetilde{u}_N^\lambda(x_{i+\lambda}) = \widetilde{\mathbf{G}}_x^{-1}(x_{i+\lambda}) * \overline{u}_N = \sum_{k=1}^{K} \sum_{r=0}^{k-1} \omega_{k,r}^\lambda(\overline{u}_N, x_i) \widetilde{p}_{k,r}^\lambda(x_{i+\lambda}), \qquad (2.19)$$

with $\lambda = \mp 1/2$ and $\lambda = 0$ respectively, where the approximation polynomials are

$$\widetilde{p}_{k,r}^\lambda(x_{i+\lambda}) = \sum_{l=0}^{k-1} c_{k,r,l}^\lambda(x_i) \overline{u}_{i-r+l}. \qquad (2.20)$$

The grid-dependent coefficients $c_{k,r,l}^\lambda$ are chosen as given by Shu [158], such that

$$\widetilde{p}_{k,r}^\lambda(x_{i+\lambda}) = u(x_{i+\lambda}) + \mathcal{O}(\Delta x_i^k). \tag{2.21}$$

Therefore different-order polynomials in the range $[1, K]$ are permitted to contribute to the truncation error. For consistency, the sum of the weights should be unity. Specifically, the following restrictions

$$\sum_{r=0}^{k-1} \omega_{k,r}^\lambda = \frac{1}{K}, \tag{2.22}$$

are used. And the weights are designed as

$$\omega_{k,r}^\lambda(\overline{u}_N, x_i) = \frac{1}{K} \frac{\gamma_{k,r}^\lambda \beta_{k,r}(\overline{u}_N, x_i)}{\sum_{s=0}^{k-1} \gamma_{k,r}^\lambda \beta_{k,s}(\overline{u}_N, x_i)}, \tag{2.23}$$

where the free discretization parameters $\gamma_{k,r}^\lambda$ are introduced to control the error cancelations. For $K = 3$, they are reduced to four independent modeling parameters $\left\{\gamma_{2,0}^{+1/2}, \gamma_{3,0}^{+1/2}, \gamma_{3,1}^{+1/2}, \gamma_{3,1}^0\right\}$, due to the restrictions of symmetries required by an isotropic discretization for the statistically homogeneous case

$$\gamma_{k,r}^{-1/2} = \gamma_{k,k-1-r}^{+1/2} \quad \text{and} \quad \gamma_{k,r}^0 = \gamma_{k,k-1-r}^0, \tag{2.24}$$

and the consequence of Eq. 2.22

$$\sum_{r=0}^{k-1} \gamma_{k,r}^{+1/2} = 1 \quad \text{and} \quad \sum_{r=0}^{k-1} \gamma_{k,r}^0 = 1. \tag{2.25}$$

The solution adaptivity of ALDM is accomplished by the smoothness-measure function

$$\beta_{k,r}(\overline{u}_N, x_i) = \left(\varepsilon_\beta + \sum_{l=-r}^{k-r-2} (\overline{u}_{i+l+1} - \overline{u}_{i+l})^2\right)^{-2} \tag{2.26}$$

where ε_β ia s small parameter to prevent division by zero values.

The 3D adaptive local deconvolution operator $\widetilde{\mathbf{G}}^{-1}(\mathbf{x})$ can be accomplished

Table 2.1: Interpolation directions for 3D reconstruction of ALDM

Positions	Relative target index $\boldsymbol{\lambda}$	Example
(R) rightward	$[+\frac{1}{2}, \quad 0, \quad 0]$	$\widetilde{u}^R_{i,j,k} \approx u(x_{i+\frac{1}{2}}, y_j, z_k)$
(L) leftward	$[-\frac{1}{2}, \quad 0, \quad 0]$	$\widetilde{u}^L_{i,j,k} \approx u(x_{i-\frac{1}{2}}, y_j, z_k)$
(F) forward	$[\quad 0, +\frac{1}{2}, \quad 0]$	$\widetilde{u}^F_{i,j,k} \approx u(x_i, y_{j+\frac{1}{2}}, z_k)$
(B) backward	$[\quad 0, -\frac{1}{2}, \quad 0]$	$\widetilde{u}^B_{i,j,k} \approx u(x_i, y_{j-\frac{1}{2}}, z_k)$
(U) upward	$[\quad 0, \quad 0, +\frac{1}{2}]$	$\widetilde{u}^U_{i,j,k} \approx u(x_i, y_j, z_{k+\frac{1}{2}})$
(D) downward	$[\quad 0, \quad 0, -\frac{1}{2}]$	$\widetilde{u}^D_{i,j,k} \approx u(x_i, y_j, z_{k-\frac{1}{2}})$

by three successive 1D operators,

$$\widetilde{u}^{\boldsymbol{\lambda}}_N(x_{i+\lambda_1}, y_{j+\lambda_2}, z_{k+\lambda_3}) = \widetilde{\mathbf{G}}^{-1}_z(z_{k+\lambda_3}) * \left(\widetilde{\mathbf{G}}^{-1}_y(y_{j+\lambda_2}) * \left(\widetilde{\mathbf{G}}^{-1}_x(x_{i+\lambda_1}) * \overline{u}_N \right) \right), \tag{2.27}$$

where $\boldsymbol{\lambda} = (\lambda_1, \lambda_2, \lambda_3)$ denotes the relative target-reconstruction positions. The required operations are performed at the centers of the cell faces, as summarized in Tab. 2.1. Note that each operator consists of two centered and one shifted steps, reconstruction operations with $\lambda = \pm 1/2$ should be performed last. Additionally, the order should be chosen by cyclic permutation to achieve rotational invariance of the implicit SGS model. The reconstructed velocities at these positions can be used in the following flux computation.

There are two steps in the numerical flux construction. The flux function $\widetilde{\mathbf{F}}_{\mathbf{N}}$ is defined as in Eq. 2.28, and the face-averaged numerical flux $\widehat{\widetilde{\mathbf{F}}}_{\mathbf{N}}$ is approximated using Eq. 2.13 . First, the consistent flux function $\widetilde{\mathbf{F}}_{\mathbf{N}} = \left[\widetilde{\mathbf{f}}^1, \widetilde{\mathbf{f}}^2, \widetilde{\mathbf{f}}^3 \right]$ is constructed as

$$\widetilde{\mathbf{F}}_{\mathbf{N}} = \mathbf{F}((\widetilde{\mathbf{u}}^-_{\mathbf{N}} + \widetilde{\mathbf{u}}^+_{\mathbf{N}})/2) + \boldsymbol{\sigma}|\delta\overline{\mathbf{u}}_{\mathbf{N}}|(\delta\widetilde{\mathbf{u}}_{\mathbf{N}}). \tag{2.28}$$

Its components can be expressed on staggered Cartesian grids in detail as

$$\widetilde{\mathbf{f}}^1_{i+\frac{1}{2},j,k} = \quad \frac{1}{4} \begin{bmatrix} (\widetilde{u}^L_{i+1,j,k} + \widetilde{u}^R_{i,j,k})(\widetilde{u}^L_{i+1,j,k} + \widetilde{u}^R_{i,j,k}) \\ (\widetilde{u}^B_{i,j+1,k} + \widetilde{u}^F_{i,j,k})(\widetilde{v}^L_{i+1,j,k} + \widetilde{v}^R_{i,j,k}) \\ (\widetilde{u}^D_{i,j,k+1} + \widetilde{u}^U_{i,j,k})(\widetilde{w}^L_{i+1,j,k} + \widetilde{w}^R_{i,j,k}) \end{bmatrix} \tag{2.29a}$$

$$- \sigma^1_{i,j,k} \begin{bmatrix} |\overline{u}_{i+1,j,k} - \overline{u}_{i,j,k}|(\widetilde{u}^L_{i+1,j,k} - \widetilde{u}^R_{i,j,k}) \\ |\overline{v}_{i+1,j,k} - \overline{v}_{i,j,k}|(\widetilde{v}^L_{i+1,j,k} - \widetilde{v}^R_{i,j,k}) \\ |\overline{w}_{i+1,j,k} - \overline{w}_{i,j,k}|(\widetilde{w}^L_{i+1,j,k} - \widetilde{w}^R_{i,j,k}) \end{bmatrix},$$

$$\widetilde{\mathbf{f}^2}_{i,j+\frac{1}{2},k} = \quad \frac{1}{4} \begin{bmatrix} (\widetilde{v}^L_{i+1,j,k} + \widetilde{v}^R_{i,j,k})(\widetilde{u}^B_{i,j+1,k} + \widetilde{u}^F_{i,j,k}) \\ (\widetilde{v}^B_{i,j+1,k} + \widetilde{v}^F_{i,j,k})(\widetilde{v}^B_{i,j+1,k} + \widetilde{v}^F_{i,j,k}) \\ (\widetilde{v}^D_{i,j,k+1} + \widetilde{v}^U_{i,j,k})(\widetilde{w}^B_{i,j+1,k} + \widetilde{w}^R_{i,j,k}) \end{bmatrix} \qquad (2.29b)$$

$$- \sigma^2_{i,j,k} \begin{bmatrix} |\overline{u}_{i,j+1,k} - \overline{u}_{i,j,k}|(\widetilde{u}^B_{i,j+1,k} - \widetilde{u}^F_{i,j,k}) \\ |\overline{v}_{i,j+1,k} - \overline{v}_{i,j,k}|(\widetilde{v}^B_{i,j+1,k} - \widetilde{v}^F_{i,j,k}) \\ |\overline{w}_{i,j+1,k} - \overline{w}_{i,j,k}|(\widetilde{w}^B_{i,j+1,k} - \widetilde{w}^F_{i,j,k}) \end{bmatrix},$$

$$\widetilde{\mathbf{f}^3}_{i,j,k+\frac{1}{2}} = \quad \frac{1}{4} \begin{bmatrix} (\widetilde{w}^L_{i+1,j,k} + \widetilde{w}^R_{i,j,k})(\widetilde{u}^D_{i,j,k+1} + \widetilde{u}^U_{i,j,k}) \\ (\widetilde{w}^B_{i,j+1,k} + \widetilde{w}^F_{i,j,k})(\widetilde{v}^D_{i,j,k+1} + \widetilde{v}^U_{i,j,k}) \\ (\widetilde{w}^D_{i,j,k+1} + \widetilde{w}^U_{i,j,k})(\widetilde{w}^D_{i,j,k+1} + \widetilde{w}^U_{i,j,k}) \end{bmatrix} \qquad (2.29c)$$

$$- \sigma^3_{i,j,k} \begin{bmatrix} |\overline{u}_{i,j,k+1} - \overline{u}_{i,j,k}|(\widetilde{u}^D_{i,j,k+1} - \widetilde{u}^U_{i,j,k}) \\ |\overline{v}_{i,j,k+1} - \overline{v}_{i,j,k}|(\widetilde{v}^D_{i,j,k+1} - \widetilde{v}^U_{i,j,k}) \\ |\overline{w}_{i,j,k+1} - \overline{w}_{i,j,k}|(\widetilde{w}^D_{i,j,k+1} - \widetilde{w}^U_{i,j,k}) \end{bmatrix},$$

where $\boldsymbol{\sigma}$ is used to compensate for different grid-size effects and is obtained as

$$\boldsymbol{\sigma}_{i,j,k} = \sigma \left(\frac{L_0}{\Delta_0} \frac{\boldsymbol{\Delta}\mathbf{x}_{i,j,k}}{L_{i,j,k}} \right)^{-1/3}. \qquad (2.30)$$

L_0 and Δ_0 denote a reference integral length scale and a reference grid size respectively. As a result of the parameter optimization process, it is $L_0/\Delta_0 = 32$. The σ introduced here is another modeling parameter of ALDM.

All the values of the five free parameters are determined so that the truncation error $\epsilon^{num}_{i,j,k}$ functions as physically motivated implicit SGS model. This purpose is achieved by a spectral analysis of the effective numerical viscosity of ALDM. The model parameters are optimized to minimize the difference between the effective numerical viscosity of ALMD and that of the Eddy-Damped Quasinormal Markovian (EDQNM) theory for isotropic turbulence in spectral space in the limit of vanishing molecular viscosity [71]. The resulting modeling parameters are listed in the Tab. 2.2.

For wall-bounded flows, for ALDM it is found that it can reproduce flow anisotropy in the near-wall region. However, the implicit SGS dissipation there is overestimated so that it leads to an under-estimated wall-shear stress. Therefore

Table 2.2: Modeling parameters of ALDM

Parameter	Optimal value
$\gamma_{3,1}^{0}$	0.0500300
$\gamma_{2,0}^{+1/2}$	1.0000000
$\gamma_{3,0}^{+1/2}$	0.0190200
$\gamma_{3,1}^{+1/2}$	0.0855000
σ	0.0689100

the van Driest damping function is used to correct the local length scale $L_{i,j,k}$ as

$$L_{i,j,k} = L_0 \left(1 - \exp\left[-\left(\frac{l_w u_\tau}{50\nu} \right)^3 \right] \right), \tag{2.31}$$

where l_w is the wall distance and u_τ is the friction velocity that is calculated from a general wall function [69]. Note that Eq. 2.31 is not a wall model but corrects near-wall SGS dissipation and holds for complex flows.

2.1.3 Numerical method

A projection method is used to solve the incompressible Navier-Stokes equations. The solution procedure consists of the following steps.

Step1 : Use ALDM to compute the convective flux $\widehat{\overline{\mathbf{F}}}_{\mathbf{N}}$ and a second-order central discretization scheme to calculate the diffusive flux and pressure gradient at time step n.

Step2 : Use a third-order Runge-Kutta scheme to advance the semi-discretization equations Eq. 2.17a in time and obtain the intermediate velocity $\overline{\mathbf{u}}^*$.

Step3 : Solve the pressure-correction Poisson equation in divergence form as

$$\iint_{\partial \Omega_{i,j,k}} \nabla \overline{\phi} \cdot \mathbf{n} dS = \frac{1}{\Delta t} \iint_{\partial \Omega_{i,j,k}} \overline{\mathbf{u}}^* \cdot \mathbf{n} dS, \tag{2.32}$$

with Neumann boundary condition $\nabla \overline{\phi} \cdot \mathbf{n} = 0$ on the fixed solid wall. $\partial \Omega_{i,j,k}$

is the boundary of the pressure cell and Δt is the time step.

Step4 : Update the velocity and pressure as

$$\overline{\mathbf{u}}^{\mathbf{n+1}} = \overline{\mathbf{u}}^* - \Delta t \nabla \overline{\phi}, \tag{2.33}$$

$$\overline{p}^{n+1} = \overline{p}^n + \overline{\phi}. \tag{2.34}$$

The pressure Poisson equation can be solved every sub-step of the Runge-Kutta scheme. Several highly efficient methods are employed to solve the pressure Poisson equation, including Fast Fourier Transform (FFT) solvers, Conjugate Gradient (CG) solver, and Krylov subspace solver with algebraic multigrid preconditioning.

The validity of the implicit SGS model has been demonstrated for a wide range of increasingly complex flows, such as isotropic turbulence [71], plane turbulent channel flow [69], passive-scalar mixing in a wide range of Schmidt numbers [72], turbulent channel flow with periodic constrictions [73], zero-pressure gradient boundary layer transition and turbulent boundary layer separation under strong adverse pressure gradient [70]. All the results show excellent agreement with the reference data from theory, DNS or experiments. The simplified version of ALDM is accomplished to reduce the amount of computational operations. It performs similarly to the ALDM without affecting the quality of the results [68]. All these validation cases are carried out using the same modeling parameters optimized from the isotropic turbulence at infinite Reynolds number, which indicates that the implicit SGS using ALDM is insensitive to the modeling parameters and is robust for a wide range of flows.

2.2 Conservative Immersed Interface Method

2.2.1 Motivation of immersed boundary methods

In LES of complex flows along complex geometries, large computational cost are required to generate suitable body-fitted grids, and the accuracy of the discretiza-

tion schemes deteriorate due to the limited grid smoothness and orthogonality. The time-consuming preprocessing has two problems: to simplify and patch the CAD geometry for surface mesh generation, and to improve the orthogonality and smoothness of spatial grids always by solving partial differential equations. Although overlapping orthogonal grids (Chimera grids) and multi-block techniques for structured grids are used to deal with complex geometries, some difficulties associated with conservative interpolation and information transformation across grid interfaces are encountered. The grid quality of unstructured meshes deteriorates with increased geometrical complexity especially in the boundary-layer regions, and the numerical truncation error can exhibit large local variations and pollutes the effect of either implicit or explicit SGS models. In particular for implicit LES approaches, where the spatial truncation error of the discretization scheme functions as SGS model, regular meshes are desirable. When simulations on moving boundaries are required, grid regeneration or deformation is necessary, which makes the traditional body-conformal method much more complex and inaccurate.

In order to decouple the grid generation with the complexity of the geometry, and to maintain the accuracy of high order numerical schemes an alternative approach combining the advantage of Cartesian mesh with the ability to deal with complex geometries has been well developed in recent years [81, 123]. These methods can simulate viscous flows with mapping of complex boundaries onto the background Cartesian meshes that do not conform to the boundary of the geometry. They are usually named according to the way to impose the boundary condition, generally immersed boundary (IB) methods. They can automatically generate underlying grids for complex geometries and are allowed for local grid refinement. This approach can treat moving geometries, multiphase or multi-material problems in a natural way while keeping the background grids fixed.

2.2.2 Brief review of IB methods

Immersed boundaries are generally not aligned with the grids, therefore, there are two key issues with IB methods: the way to impose the boundary condition and the grid refinement near the wall to resolve the near-wall region at high Reynolds

numbers. In most IB methods it is difficult to impose the boundary condition directly and sharply as using body-conformal grid. Among various boundary treatments, momentum forcing and Cartesian cut-cell methods are well developed and widely used. In the momentum forcing method, the complex object is accounted for by prescribing an appropriate continuous or discrete body force in the momentum equations. The discrete forcing method is easy to implement and more stable, which is pioneered by Mohd-Yosuf [125] and is developed by Fadlun *et al.* [49]. In this kind of method, the momentum forcing are realized implicitly by reconstruction of the flow variables using interpolation or extrapolation method in the vicinity of IB. This can eliminate the stability constraint and a delta distribution function of the continuous forcing methods as in works of Peskin [136] and Goldstein *et al.* [62], hence it is more robust and can avoid the artificial diffusion by the delta distribution function. Various linear interpolation methods are used to reconstruct the velocity which base on the assumption that the first off-wall grid points lie in the viscous sublayer. Therefore, these methods are limited to laminar flow simulations and DNS or LES computations at low to moderate Reynolds numbers [9, 49, 121, 185]. Although various multidimensional and high order polynomial interpolation schemes are investigated, they are keen to introduce wiggles and spurious extrema, and show no superiority over linear interpolation at low to moderate Reynolds numbers[114]. All the momentum forcing methods can not guarantee mass and momentum conservation near the IB, which is crucial for viscous flow simulation, especially at high Reynolds numbers. It is more challenging for LES to satisfy the requirement of mass and momentum conservation and high-order accuracy near the IB.

In the Cartesian cut-cell method, rather than adding forcing terms to the governing equations, the grid cells intersecting with the boundary are truncated to conform to the local shape of the geometry, called cut cells. The Dirichlet boundary condition can be directly adopted in the convective fluxes calculation on immersed boundary, and the mass conservation can be naturally achieved in the framework of the finite volume method. Difficulties encountered are viscous-flux reconstruction on the boundary, arbitrary shape of the cut cells and the stability constraint caused by very small cut cells, which need specific treatments. The cell-merging method in 2D [186], cell-linking [100] and mass-redistributing [39]

methods in 3D are formulated to address the stability constraint for viscous flow simulation. Very recently, the conservative immersed interface method (CIIM) using momentum-mixing procedure for small cut cells on complex geometries [121] has been constructed to remedy the difficulties of previous methods and can solve the stability problem, which is adopted here for its simplicity and high order accuracy.

Another key issue for all the aforementioned IB methods is grid refinement near the wall boundary, which can be done easily by body-conforming grids using directional refinement. There are three levels of near-wall grid refinement. The basic requirement is that the grid should represent the geometry well. This is easy to accomplish near a smooth immersed boundary, but it becomes challenging when the curvature of immersed boundary is high or has singularity, such as sharp corners. The grid should be fine enough to accurately calculate the high gradient of variables near the IB. This always requires grid refinement in the wall-normal direction. At last, when DNS or LES are used, the grid should fine enough to physically simulate the dynamics of small scales near the wall. This limits the capability of the IB method in DNS or LES at high Reynolds numbers. Adaptive mesh refinement [13], octree based methods [33], unstructured grid methods [12] and local grid refinement [48] are established to refine local grids using different data structures. Also, the IB method can be combined with curvilinear structured grids [58, 150]. This makes the grid refinement near the immersed boundary easy, but compromises the advantages of IB methods on Cartesian grids.

2.2.3 Realization of the CIIM

With CIIM, the surface of the configuration is described by a standard CAD file using STL format. A signed wall-distance level-set function is computed on Cartesian grids based on the geometry and its zero value corresponds to the immersed interface. The use of level-set function makes CIIM easy to be extended to moving boundaries, fluid-solid interaction and multi-fluid problems. The Cartesian grid cells are categorized by level-set values at their nodes, and fall into three different groups: fluid cells, solid cells and cut cells containing both fluid and solid. For fluid cells the momentum equations and pressure Poisson equation
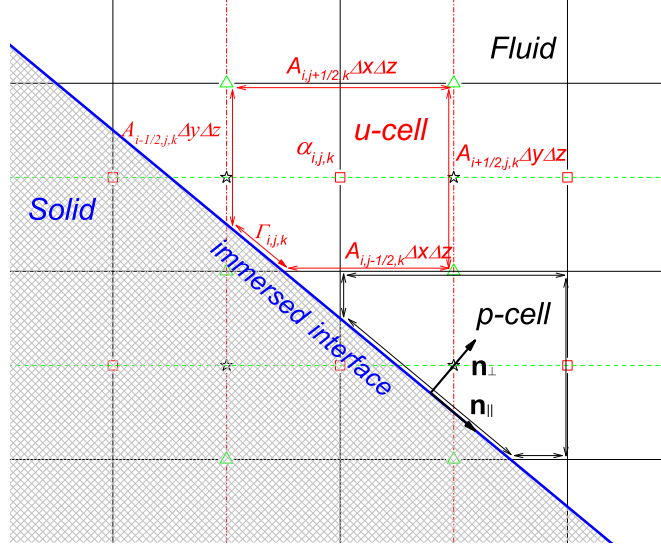
Figure 2.1: Flux calculation on a cut cell.

are solved using the same algorithm as in section 2.1.3. Solid cells are blocked out in the computation. However, the cut cells as sketched in the Fig. 2.1 need specific treatments, and the Eq. 2.17 is modified as

$$\frac{\partial \overline{\mathbf{u}}_{i,j,k}}{\partial t} + \frac{1}{V_{i,j,k}} \sum_{\partial \mathbf{I}_{i,j,k}} [\widehat{\widetilde{\mathbf{F}}}(\widetilde{\mathbf{u}}_{\mathbf{N}}) - \nu \nabla(\overline{\mathbf{u}})] \cdot \mathbf{n}\Delta S + \nabla \overline{p}_{i,j,k} + \mathbf{M}_{i,j,k} = \mathbf{0}. \qquad (2.35)$$

The control volume $V_{i,j,k}$ immersed in the fluid is computed using the volume fraction $\alpha_{i,j,k}$,

$$V_{i,j,k} = \alpha_{i,j,k} \Delta x_i \Delta y_j \Delta z_k. \qquad (2.36)$$

The area of cell faces ΔS immersed within the fluid is obtained by the face apertures $A_{l,m,n}$, as sketched in Fig. 2.1,

$$\Delta S = \begin{cases} A_{i-\frac{1}{2},j,k}\Delta y_j \Delta z_k, & \text{west,} \\ A_{i+\frac{1}{2},j,k}\Delta y_j \Delta z_k, & \text{east,} \\ A_{i,j-\frac{1}{2},k}\Delta x_i \Delta z_k, & \text{south,} \\ A_{i,j+\frac{1}{2},k}\Delta x_i \Delta z_k, & \text{north,} \\ A_{i,j,k-\frac{1}{2}}\Delta x_i \Delta y_j, & \text{back,} \\ A_{i,j,k+\frac{1}{2}}\Delta x_i \Delta y_j, & \text{front,} \\ \Gamma_{i,j,k}, & \text{immersed interface,} \end{cases} \qquad (2.37)$$

The convective fluxes and diffusive fluxes are calculated at the face centers of cut cells as with normal fluid cells, which allows the computation to use ALDM and central discretization scheme without modification. The convective flux $\mathbf{C}_{\Gamma_{i,j,k}}$ across the immersed interface

$$\mathbf{C}_{\Gamma_{i,j,k}} = \widehat{\widetilde{\mathbf{F}}}(\widetilde{\mathbf{u}}_\mathbf{N})|_{\Gamma_{i,j,k}} \cdot \mathbf{n}\Gamma_{i,j,k} \qquad (2.38)$$

can be directly calculated when the Dirichlet boundary conditions are used. It is exactly zero when applying a no-slip boundary condition. The diffusive flux $\mathbf{D}_{\Gamma_{i,j,k}}$ across the immersed interface can be calculated from the wall-shear stress as

$$\mathbf{D}_{\Gamma_{i,j,k}} = -\nu\nabla(\overline{\mathbf{u}})|_{\Gamma_{i,j,k}} \cdot \mathbf{n}\Gamma_{i,j,k} = \boldsymbol{\tau}_w \Gamma_{i,j,k}. \qquad (2.39)$$

For a rigid immersed interface the wall-shear stress can be expressed on a local frame of reference as

$$\boldsymbol{\tau}_w = \nu\nabla(\overline{\mathbf{u}})|_{\Gamma_{i,j,k}} \cdot \mathbf{n}_\perp. \qquad (2.40)$$

A linear approximation of the wall-normal velocity gradient is used to calculate the wall-shear stress [121], as shown in Fig. 2.2. To implement the linear approximation the wall-parallel velocities are required. Since the immersed interface generally does not align with the cell faces these velocities have to be interpolated from the background Cartesian grids. For this purpose trilinear interpolation method is used. As mentioned before it is very hard to refine the mesh near the boundaries having high curvature. The linear approximation has a large error when the interpolation points are located outside of the viscous sublayer, especially at high Reynolds numbers.
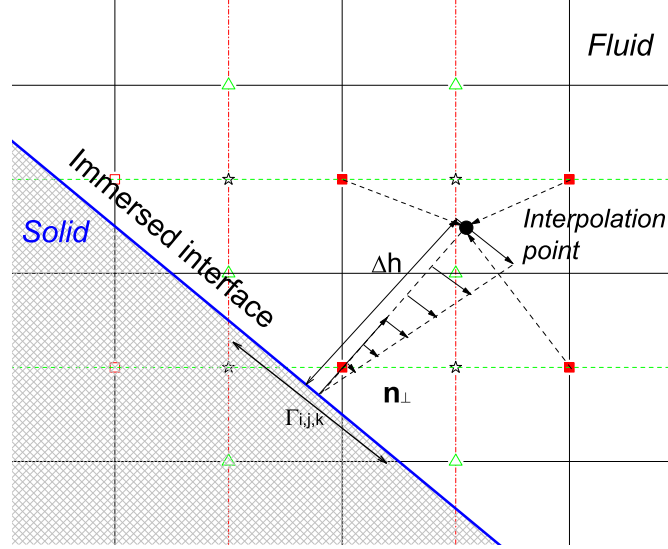
Figure 2.2: Wall-parallel velocity interpolation.

For very small cut cells that do not contribute to the pressure Poisson equation, the impermeability condition of the interface can not be achieved by a Neumann condition on the pressure, but by an acceleration of the wall-normal velocity to satisfy the wall-normal momentum balance. This is accomplished by a momentum-exchange term in the wall-normal direction

$$\mathbf{M}_{i,j,k} = -\frac{\overline{\mathbf{u}}_{\perp,i,j,k}}{\Delta t}. \tag{2.41}$$

For small cut cells the time step is restricted due to the small cell size. It is hard to obtain a stable solution using the time step calculated according to the full cell size. To alleviate this constriction a conservative-mixing procedure proposed by Hu *et al.* [78] is adapted for staggered grids. The mixing is carried out on the small cut cells and its neighbors, so-called target cells in the fluid. The target cells are determined from the interface-normal vector $\mathbf{n}_{\perp} = [n_{\perp,x}, n_{\perp,y}, n_{\perp,z}]$. There are three target cells in two dimensions, as shown in Fig. 2.3, and seven target cells in three dimensions. In the x direction, the conservative exchange of flow properties between the small cell, say (i, j, k), and its target cells is calculated by

$$X^x_{i,j,k} = \frac{\beta^x_{i,j,k}}{\beta^x_{i,j,k} V_{i,j,k} + V_{tgt}} [V_{i,j,k}(Vq^*)_{tgt} - V_{tgt}(Vq^*)_{i,j,k}], \tag{2.42}$$
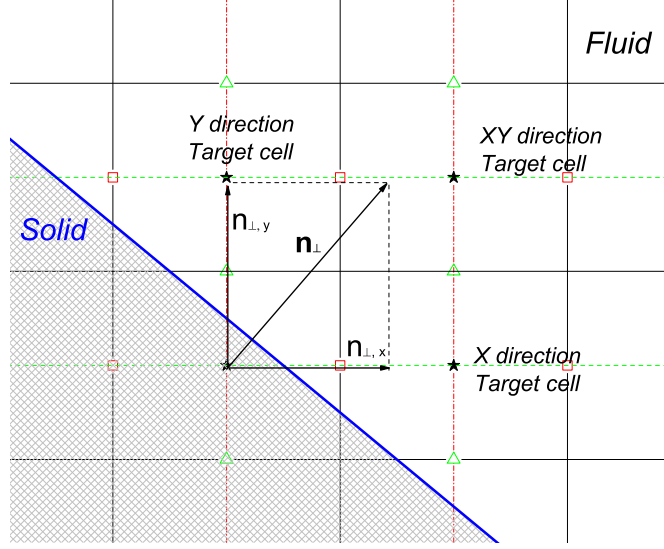
Figure 2.3: Conservative mixing procedure.

where 'tgt' is the index of the target cells and q^* is the mixed conservative quantity, which can be the divergence of flux, the velocity or a scalar concentration. And $\beta_{i,j,k}^x$ is the weight of mixing with the target cell in the x direction. In the other directions the conservative exchange can be formulated in the same way. The mixing weights of the seven target cells in three dimensions are defined as

$$
\begin{aligned}
\beta_{i,j,k}^x &= n_{\perp,x}^2 \alpha_{tgt}^{x\,\gamma}, & \beta_{i,j,k}^y &= n_{\perp,y}^2 \alpha_{tgt}^{y\,\gamma}, \\
\beta_{i,j,k}^z &= n_{\perp,z}^2 \alpha_{tgt}^{z\,\gamma}, & \beta_{i,j,k}^{xy} &= |n_{\perp,x} n_{\perp,y}| \alpha_{tgt}^{xy\,\gamma}, \\
\beta_{i,j,k}^{yz} &= |n_{\perp,y} n_{\perp,z}| \alpha_{tgt}^{yz\,\gamma}, & \beta_{i,j,k}^{zx} &= |n_{\perp,z} n_{\perp,x}| \alpha_{tgt}^{zx\,\gamma}, \\
\beta_{i,j,k}^{xyz} &= |n_{\perp,x} n_{\perp,y} n_{\perp,z}|^{2/3} \alpha_{tgt}^{xyz\gamma}. &&
\end{aligned}
\tag{2.43}
$$

They are normalized subsequently in order to satisfy

$$
\beta_{i,j,k}^x + \beta_{i,j,k}^y + ... + \beta_{i,j,k}^{xyz} = 1.
\tag{2.44}
$$

The parameter $\gamma \geqslant 1$ is used to amplify the contributions of target cells with large volume fractions. This can enhance numerical stability due to the stronger contribution of target cells having large volume fractions. A small cell obtains each conservative quantity $X_{i,j,k}$ from its target cell in the corresponding direction,

which is exactly the same as the loss X_{tgt} of that target cell, hence conservation is ensured.

When the mixing exchanges are determined for all small cells the solution q is then obtained by

$$q_{i,j,k} = q_{i,j,k}^* + \frac{1}{V_{i,j,k}}(\sum X^x + \sum X^y + ... + \sum X^{x,y,z}), \qquad (2.45)$$

where q^* is the solution before mixing. The mixing is carried out before the final pressure projection, therefore, the solution is divergence free after each time step.

In cut cells the pressure-correction Poisson equation is modified by the face apertures of pressure cell as shown in Fig. 2.1. It can be written in discretized form as

$$\sum_{\partial \Omega_{i,j,k}} \nabla \overline{\phi} \cdot \mathbf{n} \Delta S = \frac{1}{\Delta t} \sum_{\partial \Omega_{i,j,k}} \overline{\mathbf{u}}^* \cdot \mathbf{n} \Delta S, \qquad (2.46)$$

where ΔS has the same form as in Eq. 2.37, while the face apertures are different due to the staggered grids. The pressure gradients are calculated using the second-order central scheme on the cell faces as normal fluid cells. An extra term $\nabla \overline{\phi} \cdot \mathbf{n} \Gamma_{i,j,k}$ comes from the immersed interface, which is zero under homogeneous Neumann condition $\nabla \overline{\phi} \cdot \mathbf{n} = 0$. The intermediate velocities at centers of cell faces are used to calculate the divergence and corrected by the face apertures. Another extra term $\overline{\mathbf{u}}_{\Gamma_{i,j,k}}^* \cdot \mathbf{n} \Gamma_{i,j,k}$ appears on the right-hand side of the equation, and it has no contribution under the no-slip boundary condition.

Note that for fluid cells the volume fraction and face apertures are unity, therefore the fluxes and divergence of fluxes can be uniformly computed in fluid cells and cut cells. Hence, the solution procedure is as follows:

Step1 : Compute the level-set function using CAD geometry. Based on level-set function calculate the volume fractions and face apertures.

Step2 : Calculate the convective and diffusive fluxes using ALDM and central discretization scheme respectively. Then correct the fluxes using face apertures. Obtain the divergence of fluxes using volume fractions after applying the friction term.

Step3 : Perform the momentum-mixing procedure, and add the pressure gradi-

ent terms. Then apply the momentum-exchange term for small cut cells.

Step4 : Solve the semi-discretization momentum equations using third-order Runge-Kutta scheme to get the intermediate velocity.

Step5 : Solve pressure-correction Poisson equation with face-aperture correction.

Step6 : Update the velocity and pressure to the next time step.

This method has been introduced in Ref. [121] and is validated on several complex turbulent flows, including the flow over a circular cylinder at $Re_D = 3900$ and the flow along a periodic hill with massive separation. The results indicate that this method is suitable for implicit LES using and exhibits second order accuracy. The implicit LES using ALDM has been successfully implemented for incompressible Navier-Stokes equations on three-dimensional block-structured, body-fitted grids [74]. The CIIM is further compared with the body-fitted methods [122] to assess its accuracy. The assessment is carried out on the flow over the same circular cylinder using comparable numerical resolution. The results of both methods have similar accuracy for turbulence statistics and mean integral quantities comparing experimental reference data, which demonstrates that CIIM is a feasible and efficient approach to simulate turbulent flows on complex domains.

2.3   Adaptive Mesh Refinement method

At high Reynolds numbers the grid resolution near the wall is required to be high enough to resolve the near-wall flow dynamics, especially in the wall layer. When a single computational domain is used the grid refinement near the boundary should be extended to the boundary of the domain, which increases the grid resolution in all areas of the computational domain. Adaptive mesh refinement (AMR) is adopted to refine the grids locally.

There are several crucial issues for AMR, such as the data structure, refining/coarsening process and interface information communication. A pointer chain is used to link one block to another. Each block is assigned a different

integer number which corresponds to a pointer. For all blocks the integer number is continuous. The topologies including two blocks with common block vertex, common edge and common face, are explicitly established. This is different from the traditional octree data structure to index blocks. When the loop over all the blocks is required, there is no need to search tree branches but the pointer chain or the sequence of the block numbers is looped. In each block, a structured Cartesian mesh is used and its size is $N_x \times N_y \times N_z$. Every grid point can be easily established using its integer index i, j, k in three directions. Therefore, the same solver can be used for all blocks.

In the refinement process first a refinement criterion is checked. Based on the criterion a block can be refined, coarsened or divided. The refinement level of a new block is maintained correspondingly. When a block is refined, the solution on the finer block is predicted from the old coarser block using high-order conservative interpolation. If a block is coarsened, the solution on the coarser block is restricted from the old finer block conservatively. If a block is divided, the solutions on the sub-blocks are copied from the original block directly. Second, the boundaries of the new blocks are reinitialized. The old block is deleted from the block pointer chain, the new ones are added to it. The global blocks are balanced to ensure that the difference of refinement levels of two neighboring blocks is not large than one. At last, the topologies of the blocks are reestablished. This process is looped until the required refinement criterion is satisfied. The criterion could be the cut-cell size near the immersed interface, a gradient of flow variables, or some specified regions.

The inner interfaces are communicated by sending and receiving buffer regions. There are two different situations either the resolutions of two neighboring blocks having a common face are the same or may differ. In the former situation flow data in the sending-block buffer are copied to the sending buffer directly. If these two blocks are on the same computational node, the receiving buffer points to the sending buffer. If the sending and receiving blocks are on different nodes the flow data of the sending buffer are sent to the receiving buffer using MPI. At last flow data in the receiving buffer are copied to the receiving-block buffer. The communication is accomplished now. This process is sketched in Fig. 2.4.

In the latter situation conservative interpolation has to be used when the flow
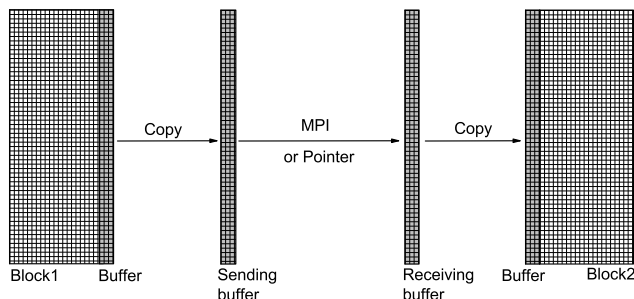
Figure 2.4: Communication of two blocks having the same resolution.

data are communicated. In order to minimize the communication bandwidth, the size of the sending and receiving buffer is the same as that of the coarser resolution of the two blocks. If the receiving block has finer resolution, the flow data in the sending-block buffer are copied to the sending buffer directly, otherwise, the flow data in the sending-block buffer are reconstructed on the sending buffer using conservative interpolation. The receiving buffer obtains the flow data by pointing to the sending buffer when both blocks are in the same computational node, or by MPI when both blocks are in different nodes. Because the resolution of the receiving buffer is coarse, when the receiving block is the coarse one, the flow data in the receiving buffer are copied to the receiving-block buffer directly, otherwise an interpolating buffer is required. The interpolating buffer has the same resolution as the fine block, and the flow data are predicted using conservative interpolation from the receiving buffer, then they are copied to the receiving-block buffer. The communication is finished now. This procedure is sketched in Fig. 2.5 for clarity. One should note that before the communication between two blocks, a regularization is applied to fluxes at hanging nodes on the fine side.

This interface communication method is very convenient for parallel implementation, and has been used in Ref. [121, 122] successfully with a large number of blocks. The flow-field continuity is preserved across interface and second-order accuracy is obtained.
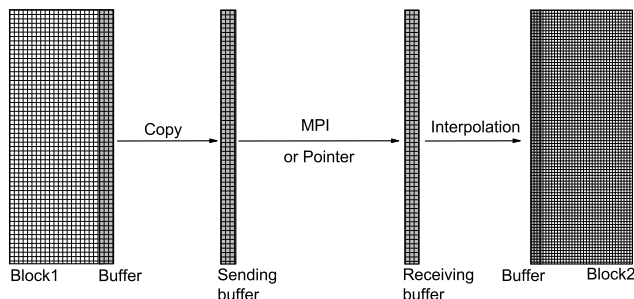
Figure 2.5: Communication of two blocks having different resolutions.

2.4 Boundary conditions

In practice a simulation is performed on a bounded flow domain. Therefore, additional source terms arise at the boundaries of the computational domain when a convolution filter applied explicitly. In the conventional mathematic framework of LES the filtered Eqs. 2.3 become

$$\frac{\partial \overline{\mathbf{u}}}{\partial t} + \nabla \cdot (\overline{\mathbf{u}\mathbf{u}}) + \frac{1}{\rho}\nabla \overline{p} - \nu \nabla^2 \overline{\mathbf{u}} =$$
$$- \iint_{\partial \Omega} \mathbf{G}(\mathbf{x} - \boldsymbol{\xi}) \left[\mathbf{u}(\boldsymbol{\xi})\mathbf{u}(\boldsymbol{\xi}) + p(\boldsymbol{\xi}) - \nu \nabla \mathbf{u}(\boldsymbol{\xi})\right] \cdot \mathbf{n}(\boldsymbol{\xi}) dS, \qquad (2.47\text{a})$$

$$\nabla \cdot \overline{\mathbf{u}} = - \iint_{\partial \Omega} \mathbf{G}(\mathbf{x} - \boldsymbol{\xi})\mathbf{u}(\boldsymbol{\xi}) \cdot \mathbf{n}(\boldsymbol{\xi}) dS, \qquad (2.47\text{b})$$

where $\mathbf{n}$ is the outward unit normal vector along the boundary $\partial \Omega$ of the computational domain Ω. In the additional boundary terms the filtered flow variables can not be obtained, but have to be modeled, because they involve the non-filtered flow variables. Therefore, it is difficult to construct a suitable boundary condition for a well-posed problem. There are two possibilities to avoid this requirement. The first one is considering that the filter width decreases as approaching the boundaries such that the interaction term cancels out. As a consequence the source term can be neglected and the basic filtered equations are the same as Eqs. 2.3. The remaining problem is to define classical boundary conditions for the filtered flow variables. The second possibility is filtering through the bound-

Figure 2.6: Well-defined filtering and the approximate deconvolution at the boundary.

ary. As a consequence, a layer exists along the boundary whose width is of the order of the filter cutoff lengthscale, where the source term cannot be neglected. This source term must then be explicitly computed, *i.e.* modeled.

In the framework of ALDM the top-hat finite-volume filter can be well-defined locally when the buffer cells along the boundary are used, as sketched in the Fig. 2.6. This results in the well-posed Eq. 2.17 on the boundary with well-defined filtered and approximately deconvolved flow variables. Thus, the classical boundary conditions for the filtered field can be used without modeling [47].

When the flow is simulated in a bounded computational domain the influence of the exterior flow is accounted for by the boundary conditions. In the framework of LES the subgrid scales are filtered out by the filtering operation and the resolved motion are described by the resolved flow variables. Therefore, the required information on the boundary is the resolved velocity and the influence of the subgrid scales, *i.e.* the subgrid stress or the divergence of the subgrid stress. The characteristics of the boundary conditions depend on the position of the boundary and the flow state. When the boundary is in the laminar-flow region the situation is simple and the mean velocity with the incoming turbulent intensity is enough. If the boundary is in the transition region, besides the

mean quantities and turbulent intensity, additional perturbations should be provided also. If the boundary is in the fully developed turbulent region, a turbulent fluctuation field has to be provided.

When the boundary is in the turbulent region the resolved velocity is time-dependent and exhibits multiple scales in space and time. Therefore, a consistent velocity boundary condition is a function of space and time. This data should provide correct first and second moments, a spectrum, and the phase information between individual modes. In principle, matching the moments and the spectra using stochastic methods is possible, whereas the specification of the phase information is much more difficult [98]. The phase information relates to the structure and shape of the resolved large scales, which strongly depends on the type of the flow. On the other hand, the influence of the subgrid scales is also difficult to be obtained or modeled, and it is usually neglected in practice. The inflow boundary is crucial for the downstream flow evolution. Without phase information inflow conditions cannot be expected to be accurate, and the flow has to undergo an adjustment, during which turbulent eddies evolve, until correct turbulence structures are established. An intuitive solution is to place the boundary into the laminar region, which means that a sufficiently large domain is needed, and that the inflow has to be located far from the region of interest. Turbulence arise naturally due to laminar-turbulent transition. This procedure makes the computation very expensive due to the extremely long computational domain, and in some situations, this procedure is not even an option, such as for the flow in a short diffuser. The main effort of the inflow generation is to shorten the developing/adjusting distance from the inlet to a streamwise station where the fully developed turbulence with correct structures are well established. Another challenge is the wall boundary condition as highlighted in the last Chapter. In the following sections, the inflow, outflow and wall boundary conditions will be introduced and their implementations in the framework of ALDM and CIIM are specified in detail.

2.4.1 Inflow boundary conditions

Temporally developing flows, such as homogeneous isotropic decay, shear layers, mixing layers and plane channels, employ periodic boundary conditions. When spatially developing flows are considered, the specification of instantaneous turbulent inlet boundary conditions is required. According to Keating *et al.* [98] inflow generation methods can be classified into three groups: precursor simulation, recycling/rescaling methods and synthetic turbulence.

The precursor simulation is carried out on an equilibrium flow. The required inflow data for an LES are extracted from this precursor simulation. This method has been successfully implemented in several LES [110, 140]. It has the advantage that the extracted data represents exactly the large scales of the flow, thus there is no or very short adjustment distance. It is easy to control boundary-layer parameters such as friction coefficient, momentum thickness *etc.* However, it has some obvious disadvantages. First, it requires much more computational effort and large storage space. Second, it is restricted to some simple flows under equilibrium [93, 113] and therefore lacks generality.

The recycling/rescaling method is a more robust technique as an extension of the Spalart modification of periodic conditions [162, 164]. This method has first been proposed by Lund *et al.* [113] for an auxiliary simulation of a spatially developing boundary layer. The auxiliary simulation of a zero pressure gradient boundary layer generates its own inflow conditions through a sequence of operations, where the instantaneous velocity field at a downstream station is rescaled in the inner and outer regions separately according to different scaling laws. The rescaled velocity profiles are reintroduced at the inlet. The recyling/rescaling methods based on the formulations of Lund *et al.* [113] are probably the most effective and the less expensive ones to generate the inflow conditions for spatially developing wall-bounded flows. However, this kind of methods still has some drawbacks: an equilibrium state is required for application of scaling laws at the inlet, the memory of the streamwise-periodic origin of the inflow may introduce a spurious periodicity into flow direction [130], and there may be a strong influence of the flow initialization [50].

Synthetic-turbulence methods generate a series of fluctuations with assigned

moments and spectra from random sequences. The simplest procedure is to take a mean velocity profile with superimposed random fluctuations. Due to the lack of phase information the levels of this synthetic turbulence decay rapidly [101, 108]. An improved method using an inverse Fourier transform of a prescribed energy spectrum is proposed by Lee *et al.* [109]. This method is limited to generate periodic signals on an uniform mesh. An alternative for arbitrary inlet meshes is accomplished by Klein *et al.* [101] and is particularly suitable for inhomogeneous turbulence. Keating *et al.* [98] point out that even complex synthesization procedures can lead to adjustment distances of order 20 times the turbulent boundary layer thickness. To incorporate some information of turbulence structures, a synthetic eddy method is proposed by Jarrin *et al.* [84] using analytical eddy structures having Gaussian shape function. A short adjustment distance is obtained in the simulation of turbulent plane channel flow. Recently, an extension of the original synthetic eddy method is proposed to account for the inhomogeneity of the scales in the direction normal to the wall using elongated streamwise vortices in the near-wall region and hairpinlike vortices in the logarithmic layer and wake region [133]. It has been tested on an LES of a spatially developing turbulent boundary layer, which shows that it is better than the original synthetic eddy method of Jarrin *et al.* [84], and is comparable to the recycling/rescaling method.

The inflow boundary condition adopted here belongs to the recycling/rescaling approach, but has some differences. First, target mean velocity and its fluctuations are prescribed or scaled from the turbulence database or other computations of the same type, assuming they obey the same scaling laws. The velocity and its fluctuations are extracted from a plane downstream. Then the velocity fluctuations are rescaled and reintroduced at the inlet. At last, mass conservation is ensured. This procedure is described in the following in detail.

In implicit LES using ALDM, the resolved flow variables are well defined on the boundary, therefore they can be applied as boundary conditions. The resolved velocity can be decomposed into a mean part and a fluctuation part at the inlet as

$$\overline{\mathbf{u}}_{\mathbf{N}} = \langle \overline{\mathbf{u}}_{\mathbf{N}} \rangle + \overline{\mathbf{u}}'_{\mathbf{N}}, \tag{2.48}$$

which means that the required velocity can be obtained using its mean value and

fluctuations. Even though the scaling laws are not expressed explicitly, the target mean velocity and its fluctuation can be prescribed as

$$\frac{\langle u \rangle_t (y_t/\delta_t)}{\langle u \rangle_{\delta_t}} = \frac{\langle u \rangle_d (y_d/\delta_d)}{\langle u \rangle_{\delta_d}} = f_u \left(\frac{y}{\delta} \right), \tag{2.49}$$

$$\frac{\langle u' \rangle_t (y_t/\delta_t)}{\langle u \rangle_{\delta_t}} = \frac{\langle u' \rangle_d (y_d/\delta_d)}{\langle u \rangle_{\delta_d}} = f_{u'} \left(\frac{y}{\delta} \right), \tag{2.50}$$

where index t and d denote 'target' and 'database', respectively. δ denotes the boundary layer thickness. f_u and $f_{u'}$ are the scaling laws for mean velocity and fluctuations respectively. When the target boundary layer thickness and mean velocities at the edge of the boundary layer are specified, the target mean velocity and its fluctuation can be obtained accordingly.

At a plane P downstream, the instantaneous velocity u_p, mean velocity $\langle u \rangle_p$ and mean second moments $\langle uu \rangle_p$ are extracted. Then the scaled velocity u_s is computed using

$$u_s = \langle u \rangle_t + \sqrt{\frac{\langle u'u' \rangle_t}{\langle u'u' \rangle_p}} (u_p - \langle u \rangle_p), \tag{2.51}$$

where $\langle u'u' \rangle_p = \langle uu \rangle_p - \langle u \rangle_p^2$. Using this scaling, the structures of fluctuation at the downstream plane P are introduced, defining the phase information. At last, mass conservation is ensured using

$$\overline{u}_N = u_s - u_{bs} + u_{bt}, \tag{2.52}$$

where b denotes the bulk velocity. It is defined as

$$u_b = \frac{1}{S_{inlet}} \iint_{S_{inlet}} \mathbf{u} \cdot \mathbf{n} dS, \tag{2.53}$$

in which S_{inlet} is the area of the inlet plane, and $\mathbf{n}$ is the normal direction of this plane. Three velocity components can be computed using the above procedure. For pressure, the Neumann boundary condition is applied there.

2.4.2 Outflow boundary conditions

The outflow boundary of the computational domain should be placed far enough from the region of interest to eliminate contaminations. The convective condition proposed by Orlanski for the problems governed by hyperbolic system of equations [132] is widely used due to its good characteristics. It had been shown by Pauley *et al.* [135] that for unsteady flows the convective condition at outlet is suitable for moving structures out of the computational domain without severe effects in the computational domain. The resolved velocity component $\overline{u}$ at outlet is updated using

$$\frac{\partial \overline{u}}{\partial t} + U_c \frac{\partial \overline{u}}{\partial x} = 0, \tag{2.54}$$

where the convection velocity U_c is loosely defined by different authors. It can be either the maximum streamwise velocity, the mean streamwise velocity [108, 127] at outlet or a local velocity [113].

Another option is to apply Neumann boundary conditions for velocity at outlet using buffer cells. This method is often as good as convective condition. The Dirichlet or Neumann boundary condition for pressure can be used at outlet.

2.4.3 Wall boundary conditions

In the simulation without wall model, a no-slip boundary condition is used. The Neumann boundary condition for pressure $\partial p / \partial \mathbf{n}$ is applied at the wall. Wall modeling to approximate the wall boundary condition for coarse meshes and turbulent flow is the subject of the next chapter.

Chapter 3

Wall Modeling

3.1 Wall modeling overview

The main purpose of wall modeling is to approximate the wall layer (viscous sublayer and buffer layer) with a proper model to avoid the prohibitive resolution requirements of wall-resolved LES. These models have to provide information to the exterior LES, resulting in well established exterior turbulence dynamics. However, near-wall turbulence details are not recovered by the wall-layer approximation, such as laminar-turbulent transition.

Despite the fact that ALDM gives improved predictions of turbulence anisotropy compared with common explicit SGS models [69], the fundamental problem of having to resolve the near-wall region in turbulent flows is shared with all other implicit or explicit LES approaches. This results in the high computational cost to simulate wall-bounded flows at high Reynolds numbers. When the CIIM is used with ALDM, on one hand, the position of the interpolation point is required to lie within the viscous sublayer, on the other hand, it is hard to use an anisotropic mesh refinement method to get the required resolution near the immersed interface on the Cartesian grids. Therefore, wall models are applied to implicit LES using ALDM to reach high Reynolds numbers.

Wall models should use some information from exterior LES and feed back some information to the exterior flow simulation, as sketched in Fig. 3.1. Following the analysis in Chapter 1, a feasible way is to use wall-stress models to supply
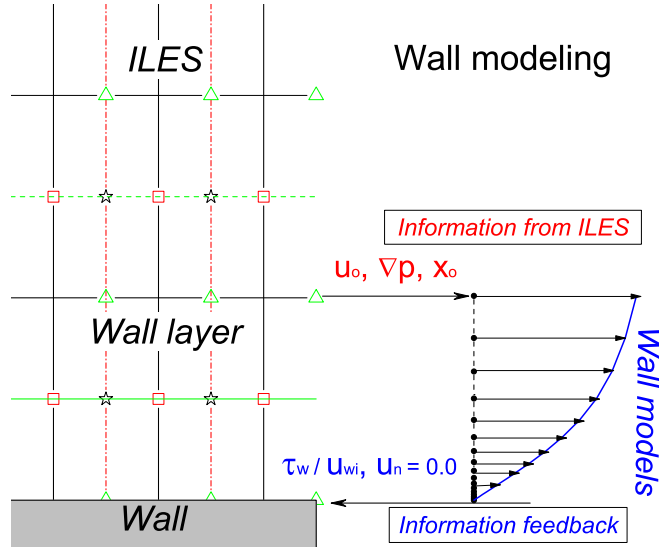
Figure 3.1: Sketch of wall modeling.

the wall-shear stress as an approximate wall boundary condition to the exterior LES. A slip-wall boundary condition derived from the wall-shear stress can also be enforced at the wall. Other concerns are the accuracy and computational cost of a wall model. As the formulation of wall boundary conditions differs between using body-conforming mesh and CIIM, respective wall-modeling frameworks are introduced separately in the following.

3.2 Wall modeling on body-conforming grids

On body-conforming grids, it is straightforward to exploit the information from the exterior LES. The information from wall models can be fed back in a natural way. Since the wall conforms with the mesh velocity and pressure gradient at a certain position $\mathbf{x}_o$ of the LES can be obtained directly by one-dimensional interpolation method. In a simulation with an unresolved wall-layer, the diffusive flux at the wall cannot be accurately calculated by applying the usual no-slip condition. Consequently, a wall stress model needs to provide a more physical wall-shear stress τ_{wi}, $(i = 1, 3)$ in the two wall-tangential directions. These stresses can be used directly to specify the wall diffusive flux without coordinate

transformation, and the wall-normal velocity u_{w2} is set to zero,

$$\mu \frac{\partial u_i}{\partial x_2}\bigg|_{x_2=0} = \tau_{wi}, \tag{3.1}$$

$$u_{w2} = 0.$$

Another option is to apply a slip-wall boundary condition in wall-tangential directions. The slip velocity can be derived from the wall-shear stress by a linear friction approximation, while the wall-normal velocity is set to zero. Hence, in this case the velocity boundary condition at the wall can be written as

$$u_{wi} = u_{1i} - \Delta x_2 \tau_{wi}/\mu, \quad (i = 1, 3), \tag{3.2}$$

$$u_{w2} = 0,$$

where u_{wi} is the slip-velocity component at the wall, u_{1i} is the wall-tangential velocity component at the first off-wall point, and the Δx_2 is the wall distance of the first off-wall point. The slip-wall approximation often tends to convergence problems with the iterative pressure Poisson solver and is not as robust as wall-shear stress boundary. Therefore, it is left out of further consideration. Three different types of wall-stress model are further investigated. They are based on a generalized wall function, a two-layer power law, and a simplified TBLE.

3.2.1 Generalized wall function

The basic idea of the generalized wall function [156] is to use a hybrid velocity scale to formulate the scaling laws, which can take the effect of a pressure gradient into account. The hybrid velocity scale u_c is defined as

$$u_c = u_\tau + u_p, \tag{3.3}$$

where u_τ and u_p are velocity scales defined by the wall-shear stress and the wall-tangential pressure gradient, respectively,

$$u_\tau = \left(\frac{|\tau_{wi}|}{\rho}\right)^{1/2}, \quad u_p = \left(\frac{\nu}{\rho}\left|\frac{dp_w}{dx_i}\right|\right)^{1/3}. \tag{3.4}$$

In the inertial layer, the hybrid velocity scale is used to blend the standard wall function

$$\frac{u_{oi}}{u_\tau} = \frac{1}{\kappa} \ln \left(\frac{u_\tau y}{\nu} \right) + C, \tag{3.5}$$

and the asymptotic solution of Tennekes and Lumley [174]

$$\frac{u_{oi}}{u_p} = \alpha \ln \left(\frac{u_p y}{\nu} \right) + \beta. \tag{3.6}$$

u_{oi} is the wall-tangential velocity from the exterior LES, as sketched in Fig. 3.1. The former is only valid for a zero-pressure-gradient boundary layer, and the latter is derived under a large adverse pressure gradient and zero wall stress. The resulting blended function based on the hybrid scaling velocity u_c is

$$\frac{u_{oi}}{u_c} = \frac{\tau_{wi}}{\rho u_\tau^2} \left[\frac{1}{\kappa} \frac{u_\tau}{u_c} \ln \left(y_c^+ \right) + C_1 \right] + \frac{\nu}{\rho} \frac{\partial p_w / \partial x_i}{u_c^3} \left[\alpha \ln \left(y_c^+ \right) + \beta \right], \tag{3.7}$$

and the coefficient C_1 is

$$C_1 = \frac{u_\tau}{u_c} \left[\frac{1}{\kappa} \ln \left(\frac{u_\tau}{u_c} \right) + C \right]. \tag{3.8}$$

where the constant coefficients κ, C, and α, β are listed in Tab. 3.1 and Tab. 3.2, respectively, and $y_c^+ = y u_c / \nu$.

In the viscous sublayer, the wall function is scaled using u_c as

$$\frac{u_{oi}}{u_c} = \frac{\tau_{wi}}{\rho u_c^2} y_c^+ + \frac{1}{2} \frac{\nu}{\rho} \frac{\partial p_w / \partial x_i}{u_c^3} (y_c^+)^2, \tag{3.9}$$

which also takes the effect of pressure gradient into account.

The scaling laws in the inertial layer Eq. 3.7, and in the viscous sublayer Eq. 3.9, are unified by introducing a turbulent stress model in the buffer layer similarly as done by Spalding [165]. Therefore, the resulting generalized wall function covers the viscous sublayer, buffer layer and inertial layer. But the analytic formula is not very convenient for application, hence a curve-fitting version is

used, which is written as

$$\frac{u_{oi}}{u_c} = \frac{\tau_{wi}}{\rho u_\tau^2}\frac{u_\tau}{u_c}f_1(y_\tau^+) + \frac{\nu}{\rho}\frac{\partial p_w/\partial x_i}{u_c^3}f_2(y_c^+), \qquad (3.10)$$

where $y_\tau^+ = yu_\tau/\nu$, f_1 and f_2 are the piecewise fitting functions. They are defined as

$$f_1(y_\tau^+) = \begin{cases} a_1 y_\tau^+ + a_2(y_\tau^+)^2 + a_3(y_\tau^+)^3 & \text{if } \quad y_\tau^+ \leq 5; \\ b_0 + b_1 y_\tau^+ + b_2(y_\tau^+)^2 + b_3(y_\tau^+)^3 + b_4(y_\tau^+)^4 & \text{if } \ 5 < y_\tau^+ \leq 30; \\ c_0 + c_1 y_\tau^+ + c_2(y_\tau^+)^2 + c_3(y_\tau^+)^3 + c_4(y_\tau^+)^4 & \text{if } 30 < y_\tau^+ \leq 140; \\ \frac{1}{\kappa}\ln(y_\tau^+) + C & \text{if } \quad y_\tau^+ \geq 140. \end{cases} \qquad (3.11)$$

$$f_2(y_c^+) = \begin{cases} a_2(y_c^+)^2 + a_3(y_c^+)^3 & \text{if } \quad y_c^+ \leq 4; \\ b_0 + b_1 y_c^+ + b_2(y_c^+)^2 + b_3(y_c^+)^3 + b_4(y_c^+)^4 & \text{if } \ 4 < y_c^+ \leq 15; \\ c_0 + c_1 y_c^+ + c_2(y_c^+)^2 + c_3(y_c^+)^3 + c_4(y_c^+)^4 & \text{if } 15 < y_c^+ \leq 30; \\ \alpha\ln(y_c^+) + \beta & \text{if } \quad y_c^+ \geq 30. \end{cases} \qquad (3.12)$$

The coefficients of f_1 and f_2 are also listed in Tab. 3.1 and Tab. 3.2 respectively.

First, the velocity u_{oi} and the wall-tangential pressure gradient are interpolated from exterior LES at a certain wall distance y. Then the generalized wall function is solved by a Newton-iteration method to obtain u_τ, and the wall-shear stress can be computed as

$$\tau_{wi} = \left\{\frac{u_{oi}}{u_c} - \frac{\nu}{\rho}\frac{\partial p_w/\partial x_i}{u_c^3}f_2\right\}\frac{\rho u_\tau^2}{\frac{u_\tau}{u_c}f_1}. \qquad (3.13)$$

This model is denoted as GWFP hereafter.

3.2.2 Wener-Wengle function

A simple two-layer approximation, proposed by Werner and Wengle [182], is based on an assumption of a power-law outside the viscous sublayer, interfaced with the linear profile in the viscous sublayer. This model is chosen according to its good performance in Ref. [171] and its simplicity without need for an iterative solver,

Table 3.1: Coefficients of f_1

κ	C			
0.41	5.0			
a_1	a_2	a_3		
1.0	1.0E-02	-2.9E-03		
b_0	b_1	b_2	b_3	b_4
-0.872	1.465	-7.02E-02	1.66E-03	-1.495E-05
c_0	c_1	c_2	c_3	c_4
8.6	0.1864	-2.006E-03	1.144E-05	-2.551E-08

Table 3.2: Coefficients of f_2

α	β			
5.0	8.0			
a_2	a_3			
0.5	-7.31E-03			
b_0	b_1	b_2	b_3	b_4
-15.138	8.4688	-0.81976	3.7292E-02	-6.3866E-04
c_0	c_1	c_2	c_3	c_4
11.925	0.93400	-2.7805E-02	4.6262E-04	-3.1442E-06

and reads as

$$u^+ = \begin{cases} x_2^+, & x_2^+ \leq 11.81, \\ A(x_2^+)^B, & x_2^+ > 11.81, \end{cases} \tag{3.14}$$

where $A = 8.3$ and $B = 1/7$. Werner and Wengle [182] proposed the use of spatial average of the velocity distribution profile from the wall to the interpolation point to obtain a mean velocity. This mean velocity $|u_{oi}|$ is used to calculate the wall-shear stress written as

$$|\tau_{wi}| = \begin{cases} \frac{2\mu|u_{oi}|}{\Delta x_2}, & |u_{oi}| \leq \frac{\mu}{2\rho\Delta x_2}A^{\frac{2}{1-B}}, \\ \rho[\frac{1-B}{2}A^{\frac{1+B}{1-B}}(\frac{\mu}{\rho\Delta x_2})^{1+B} \\ +\frac{1+B}{A}(\frac{\mu}{\rho\Delta x_2})^B|u_{oi}|], & |u_{oi}| > \frac{\mu}{2\rho\Delta x_2}A^{\frac{2}{1-B}}, \end{cases} \tag{3.15}$$

and the sign of the wall-shear stress is the same as for the interpolated velocity u_{oi} at point 'o'. Δx_2 is the wall distance from the interpolation point 'o' to the wall. This model is denoted as WW hereafter.

3.2.3 Wall modeling based on simplified TBLE

In order to include more details of the near-wall flow dynamics and still to maintain high computational efficiency, the unsteady boundary layer equations

$$\frac{\partial u_i}{\partial x_i} = 0, \quad (i = 1, 2, 3) \tag{3.16a}$$

$$\nu \frac{\partial^2 u_i}{\partial x_2^2} = \frac{\partial u_i}{\partial t} + \frac{1}{\rho}\frac{\partial p}{\partial x_i} + \frac{\partial u_i u_j}{\partial x_j}, \quad (i = 1, 3; j = i, 2), \tag{3.16b}$$

are chosen as basis of wall-modeling equations, where x_2 is the wall-normal direction, and $x_i(i = 1, 3)$ are wall-tangential. The momentum equations Eq. 3.16b are integrated from the wall to the interpolation point $x_{2o} = \delta$ in the wall-normal direction, incorporating the Reynolds decomposition. The wall-shear stress can be obtained from

$$\frac{\tau_{wi}}{\rho} = \nu\frac{\partial \overline{u}_i}{\partial x_2}\Big|_\delta - (\overline{u}_i\overline{u}_2 + \overline{u_i' u_2'})\Big|_\delta - \int_0^\delta (\frac{\partial \overline{u}_i\overline{u}_i}{\partial x_i} + \frac{\partial \overline{u_i' u_i'}}{\partial x_i})dx_2$$
$$-\frac{\partial}{\partial t}\int_0^\delta \overline{u}_i dx_2 - \frac{\partial \overline{p}}{\partial x_i}\delta. \tag{3.17}$$

Hoffman and Benocci [75] pointed out that the sum of the two mean-convective terms can be neglected, but it is not legitimate to neglect just one of them. Furthermore, Wang and Moin [181] showed that the nonlinear terms are responsible for an overprediction of the wall-shear stress on the flat section of an airfoil. As they are not very significant in the near-wall layer, the nonlinear convective terms are neglected to avoid the need for using an expensive iterative solver. The Reynolds normal stresses are assumed be small, and a turbulent eddy viscosity is used to relate the Reynolds shear stress to the mean-velocity gradient in the wall-normal direction. The pressure is constant using zero wall-normal pressure gradient under the boundary layer assumption in the wall-normal direction. The wall-parallel pressure gradient is kept to account for its contribution to the near-wall momentum balance. The time derivative is kept to account for the effect of flow unsteadiness on the wall-shear stress. At last, based on the work of Refs.

[34, 35, 36], the following simplified TBLE are returned

$$\frac{\partial}{\partial x_2}(\nu + \nu_t)\frac{\partial \overline{u}_i}{\partial x_2} = \frac{\partial \overline{u}_i}{\partial t} + \frac{1}{\rho}\frac{\partial \overline{p}}{\partial x_i}, \quad (i = 1, 3). \tag{3.18}$$

A mixing-length eddy-viscosity model with a damping function is adopted to account for near-wall turbulence

$$\nu_t = \kappa x_2 u_\tau (1 - e^{-x_2^+/A})^2, \tag{3.19}$$

where $\kappa = 0.4$, $A = 19.0$ and $x_2^+ = x_2 u_\tau/\nu$. The simplified TBLE, Eqs. 3.18 are ordinary differential equations. Therefore they can be integrated as in Eq. 3.17 from $x_{2o} = \delta$ down to the wall to give a closed-form expression of the wall-shear stress components

$$\tau_{wi} = \mu\frac{\partial \overline{u}_i}{\partial x_2}\Big|_{x_2=0} = \frac{\rho}{\int_0^\delta \frac{dx_2}{\nu+\nu_t}}\left\{u_{oi} - \frac{1}{\rho}\frac{\partial \overline{p}}{\partial x_i}\int_0^\delta \frac{x_2 dx_2}{\nu + \nu_t} - \int_0^\delta \frac{\int_0^{x_2}\frac{\partial \overline{u}_i}{\partial t}dx_2'}{\nu + \nu_t}dx_2\right\}. \tag{3.20}$$

If the time derivative is eliminated, and as the turbulent viscosity ν_t only depends on the friction velocity and the wall distance, the above equation can be integrated numerically to obtain the final wall-shear stress. Otherwise, the velocity distribution in the wall layer has to be constructed. Eq. 3.18 is discretized using a second-order central scheme on an embedded stretched grids between the wall and the interpolation point in the wall-normal direction. The no-slip boundary condition is imposed at the wall. The upper boundary conditions for velocity and pressure gradients are interpolated from the exterior LES. The resulting three-diagonal linear equation systems are solved by a tridiagonal matrix solver. Note that TBLE are solved at every Runge-Kutta substep, the velocities on the embedded grids are updated by the Runge-Kutta method of the time-derivative term. This model is denoted as TBLE hereafter.

3.3   Wall modeling with CIIM

In the framework of CIIM, the boundary in general does not conform to the background Cartesian mesh, and the wall stress cannot be used as wall flux directly without tensor transformation. Sondak and Pletcher [161] introduced a procedure to perform a transformation of the stresses from the generalized coordinate system $\boldsymbol{\xi}$ to the Cartesian coordinate system $\mathbf{x}$. The adopted standard tensor transformation is written as

$$\tau_{\alpha\beta} = \frac{\partial \xi_\alpha}{\partial x_i}\frac{\partial \xi_\beta}{\partial x_j}\tau_{ij}, \tag{3.21}$$

where α and β represent the components of the geodesic coordinate, and i and j are the components of the Cartesian coordinate. In three dimensions, a 6×6 coordinate-transformation matrix needs to be inverted to obtain the stresses τ_{ij} in Cartesian coordinates. This approach is rather expensive and can introduce significant numerical errors when performing the coordinate transform.

In very few sources, several ways are proposed to implement wall models using immersed boundary methods. In a preliminary investigation on the hydrofoil at high Reynolds number [175], the filtered Navier-Stokes equations are solved down to the second off-wall grid points near the IB, and the velocities at the first off-wall grid points are reconstructed by solving the thin boundary layer equations only keeping the diffusion term, called equilibrium-stress-balance model, in the wall-normal direction. Only the improved mean velocities are presented in comparison with those of coarse LES using the IB method. In an application to the same hydrofoil by Cristallo and Verziccoin [40], the same simplified thin boundary layer equations are solved to provide the LES with a wall-shear stress as an approximate boundary condition, and the filtered Navier-Stokes equations are solved down to the first off-wall grid points. There is no detail given on how the wall-shear stress is implemented. It is stated that this particular implementation is better than that of Ref. [175], without further validation. Choi *et al.* [37] have used a power law function to interpolate the velocities in the wall-normal direction, which is claimed to be suitable for flow simulations at high Reynolds numbers. Recently, a detailed investigation has been carried out for the simulation of plane

56

turbulent channel flow using IB method on both Cartesian and curvilinear grids by Roman *et al* [149]. A linear interpolation method and the logarithmic law are chosen to reconstruct the local wall-normal and wall-tangential velocities at the first off-wall grid points, according to different nondimensional wall distance. A RANS-like eddy viscosity is constructed at the cell faces between the first off-wall cell and its next neighbors to apply the wall-shear stress through a turbulent diffusive flux. The results show that to use only a velocity-reconstruction near the IB is insufficient and leads to a wrong mean-velocity profile. A RANS-like eddy viscosity is necessary and crucial for a proper mean velocity prediction. The mean velocity and RMS velocities are reproduced well through a proper parametrization of the viscous flux. However, this method is not suitable for general flows because of the underlying logarithmic law assumption and difficulties in associated with the dependence of viscous flux reconstruction on the wall distance. Almost all these methods use wall models to reconstruct the velocity near the IB, which is consistent with the discrete-forcing IB method in the finite-difference framework. However, this leads to violation of the divergence-free constrain of the velocity field, and the satisfaction of the wall boundary condition is not straightforward.

Rather than applying the wall-shear stress directly, the wall-shear force as Eq. 2.39 is computed from the wall-shear stress $\boldsymbol{\tau_w}$ provided by a wall model. This force is added to momentum equations to include the effect of the wall layer on the exterior LES. It also provides the diffusive flux at the immersed interface for the CIIM. This method is consistent with the underlying finite volume method and can be easily and accurately implemented.

To calculate the wall-shear stress, the local wall-normal vector $\mathbf{n}$ and wall-tangential directions $\mathbf{t}_i (i = 1, 3)$ should be defined. The wall-normal vector is obtained by the normalized gradient of the level-set function. Since the wall-shear stress is not known, the wall-tangential directions can not be defined by the directions of the main axes of the wall-shear stress. But one wall-tangential direction $\mathbf{t}_1$ is defined by projection of one axis of the Cartesian coordinate along the wall-normal direction onto the local wall-tangential plane. The other $\mathbf{t}_3$ is obtained by the cross product of the wall-normal and the first wall-tangential vectors. The interpolation point 'o' having a certain wall distance d is defined along the wall-normal direction in the fluid. Its coordinate $\mathbf{x}_o$ can be expressed
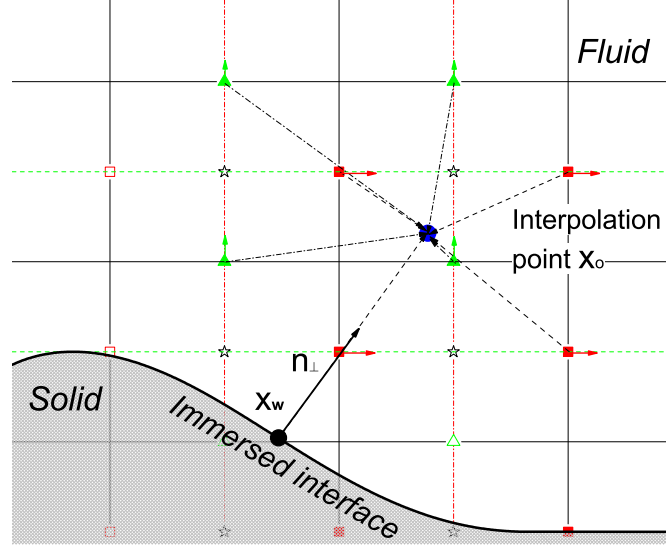
Figure 3.2:   Interpolation for wall modeling with CIIM.

as

$$\mathbf{x}_o = \mathbf{x}_w + \mathbf{n}d, \tag{3.22}$$

where $\mathbf{x}_w$ is the coordinate of the projection of the cut cell center on the wall, as shown in Fig. 3.2. Grid points around the interpolation point are identified for interpolation. It has to be noted that the velocity components and pressure gradients should be interpolated separately due to the background staggered Cartesian grids, which increases the interpolation effort. A linear least square interpolation method, a trilinear interpolation method and a pseudo-Laplacian weighted averaging method, are used to perform the interpolation, which are given in the App. A. After the required velocity and pressure gradient are interpolated from the exterior LES, either one of the wall models described in the last section 3.2 can be used to obtain the wall-shear stresses τ_{wi} in the wall-tangential direction $\mathbf{t}_i$ accordingly. The wall-shear force $\mathbf{F}_w$ can be computed from

$$\mathbf{F}_w = (F_{wx}, F_{wy}, F_{wz}) = V_{i,j,k}^{-1} \left(\mathbf{t}_1 \tau_{w1} + \mathbf{t}_3 \tau_{w3}\right) \Gamma_{i,j,k}, \tag{3.23}$$

where F_{wx}, F_{wy} and F_{wz} are the three components of wall-shear force in the Cartesian coordinate system. They can be added to the momentum equations as source terms directly.

Chapter 4

Analysis and Validation

The canonical plane Turbulent Channel Flow (TCF) and the flow through a backward-facing step according to the experiment of Jovic and Driver [91] are chosen to investigate the wall models. TCF is the most basic wall-bounded flow of practical relevance in the historical study of the turbulence. Many experiments have been performed to validate scaling laws of turbulent flows, and many turbulence modeling methods have been tested for this canonical flow. For the backward-facing step the flow is comparably complex including turbulent separation, recirculation bubble, reattachment and flow recovery. It is a suitable case for validating the capability of a wall model to account for flow separation, and it has been extensively considered in the development of wall modeling. In the following sections, first, wall models are investigated on body-conforming meshes. Subsequently they are studied in conjunction with CIIM to validate the findings with respect to the body-conforming-mesh results and to extend the framework of wall modeling to deal with complex geometries.

4.1 Wall modeling for canonical flows on body-fitted meshes

In this section, the characteristics of coarse LES without wall modeling are investigated, then the wall models are applied at the wall under original ALDM formulation which employs a van Driest damping function to one of the model

parameters, Eq. 2.31, denoted as VD. In conjunction with wall models this near-wall treatment is found to be unsuitable and a modified formulation based on coherent structures is developed for wall modeling at high Reynolds numbers. The influence of coupling position between TBLE and exterior LES is studied. The parameters of TBLE and the grid resolution of exterior LES are also investigated. At last the wall models are investigated on the backward-facing step using multi-block body-fitted structured meshes to check their ability to reproduce the complex separated flow.

4.1.1 Investigations on TCF

The computational domain is $2\pi H \times 2H \times \pi H$ in streamwise, wall-normal and spanwise directions, respectively, where H is the half channel height. The flow is driven by a constant streamwise pressure gradient to sustain constant mass flux. Periodic boundary conditions are applied in the streamwise and spanwise directions. A no-slip boundary condition is used at the wall when the wall models are not adopted. Otherwise, the wall-shear stress obtained from the wall model is imposed at the wall as diffusive flux when computing the cell flux balance. The time step is dynamically adapted to satisfy a Courant-Friedrichs-Lewy (CFL) condition with $CFL = 1.0$ for all cases. The pressure Poisson equation is solved at every Runge-Kutta substep. Fast Fourier transform is employed in the spanwise and streamwise directions, and a direct tridiagonal matrix inversion is used in the wall-normal direction. The simplified version of ALDM is adopted due to its improved computational efficiency [68].

4.1.1.1 Coarse LES without wall modeling

Simulations are performed at $Re_\tau = 395$ on several coarse meshes. The grids are equally distributed in the streamwise and spanwise directions. In the wall-normal direction, the grid points are equally distributed or stretched by a hyperbolic tangent function

$$y_j = -\frac{H}{\tanh(C_G)} \tanh\left(C_G - 2C_G \frac{j}{N_y}\right), \tag{4.1}$$

Table 4.1: Cases of coarse LES without wall modeling

case	$N_x \times N_y \times N_z$	C_G	y_1^+	$-dP/dxH$	$\langle \tau_{w1} \rangle$	$-\langle \tau_{12}^{sgs} \rangle|_0$
LES_CR1	$16 \times 16 \times 16$	$HOMO$	24.7	8.488e-3	1.221e-3	7.267e-3
LES_CR2	$16 \times 16 \times 16$	1.5	8.8	3.606e-3	2.085e-3	1.521e-3
LES_CR3	$32 \times 32 \times 32$	$HOMO$	12.3	6.339e-3	2.057e-3	4.282e-3
LES_CR4	$32 \times 32 \times 32$	1.5	4.0	3.336e-3	2.976e-3	0.360e-3

(a) Mean velocity profiles

(b) Reynolds stresses
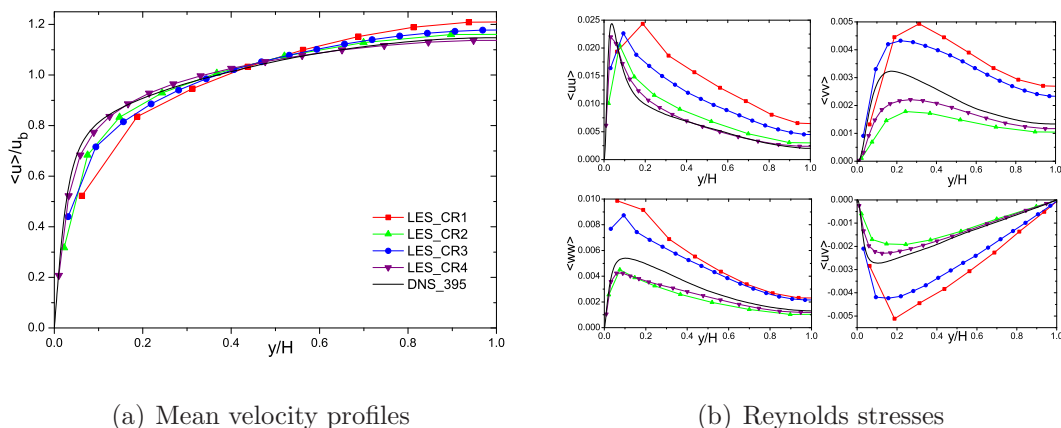
Figure 4.1: Comparisons of mean flow variables scaled by bulk velocity for coarse LES and DNS [126] at $Re_\tau = 395$.

where C_G is the stretching factor. All the cases are detailed in Tab. 4.1, where $N_x \times N_y \times N_z$ is the resolution in the streamwise, wall-normal and spanwise directions respectively, and $HOMO$ means equidistant mesh in wall-normal direction. On coarse meshes, since the wall-shear stresses are heavily under predicted, mean velocity and Reynolds stresses are nondimensionalized using the bulk velocity. The results are shown in Fig. 4.1 and are compared with those of DNS [126]. In cases LES_CR2 and LES_CR4 with wall-normal grids stretched near the wall, the flows are much better predicted than in the cases LES_CR1 and LES_CR3 having the same resolution. The behavior of the mean velocity is similar, with underpredicted near-wall values, but overpredicted values near the channel center, see Fig. 4.1(a), due to the constraint of constant mass flux. Therefore, the mean velocity gradient of the exterior LES is larger than that of DNS, which can

(a) Mean velocity profiles

(b) Local von Kármán constant κ
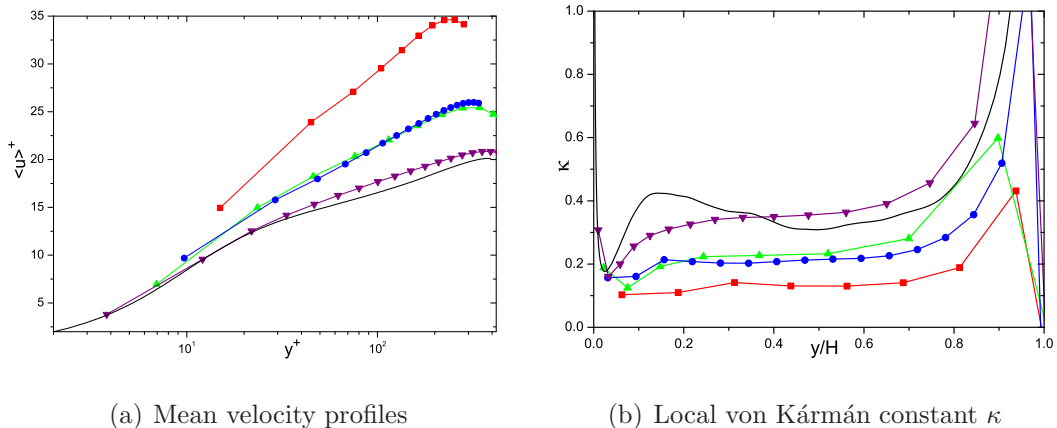
Figure 4.2: Comparisons of mean velocity and κ for coarse LES and DNS at $Re_\tau = 395$. Lines labeled as in Fig. 4.1(a).

be observed in Fig. 4.2, where the local von Kármán constant is defined as

$$\kappa = \frac{1}{y^+ d\overline{u}^+ / dy^+}. \tag{4.2}$$

In this equation " $+$ " means that the mean velocity is scaled by friction velocity u_τ, or the wall distance is scaled by wall units ν/u_τ. It can be seen from the result of DNS that there is no pronounced logarithmic region with constant κ at this relatively low Reynolds number. However, in the coarse LES, the profiles of κ are much more flat and exhibit an equivalent logarithmic region. All κ are underpredicted except for LES_CR4, as shown in Fig. 4.2(b).

The behavior of the Reynolds stresses is much different. In cases with stretched wall-normal grids, the Reynolds stresses are underpredicted, except for the streamwise normal stress. In cases with wall-normal homogeneous grids, Reynolds stresses are all heavily overpredicted, as shown in Fig. 4.1(b). This means that the resolved turbulence production on coarse meshes is overpredicted, as shown in Fig. 4.3(a), which is consistent with their overpredicted shear stress and velocity gradient of exterior LES. The nondimensional resolved production is defined as

$$P^+ = -\langle \overline{u}\,\overline{v} \rangle^+ \frac{d\overline{u}^+}{dy^+}. \tag{4.3}$$

In case LES_CR2, the resolution is globally coarser than in case LES_CR3,
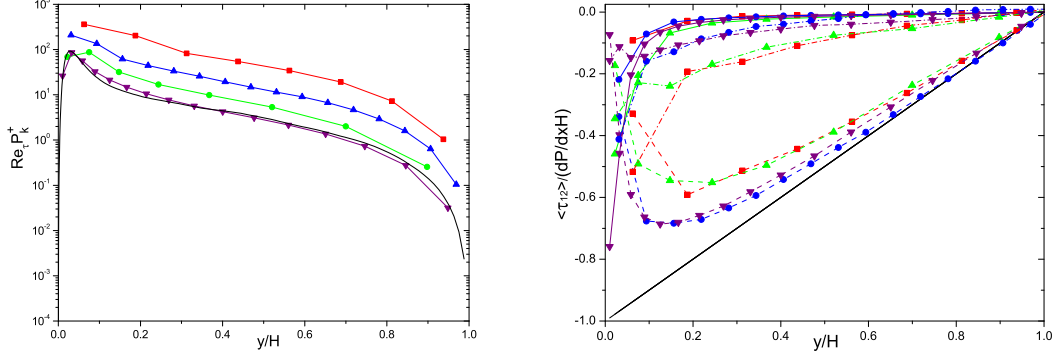
(a) Comparisons of turbulence production for coarse LES and DNS [126] at $Re_\tau = 395$. Lines labeled as in Fig. 4.1(a).

(b) Streamwise shear stress balance. Solid lines: total shear stress; solid lines with symbols: viscous stress; dashed lines with symbols: resolved shear stress; dashdotted lines with symbols: subgrid stress. Symbols denote different cases as in Fig. 4.1(a).

Figure 4.3: Comparisons of turbulence production and streamwise shear stress balance for coarse LES.

however, the former has better predicted mean velocity and Reynolds stresses, since its wall distance of first off-wall grid point is smaller as presented in Tab. 4.1. Hence, it can be deduced that the position of the first off-wall grid point is very important for mean-flow variable prediction.

In order to analyze the streamwise momentum balance the following mean-streamwise momentum equation of TCF is used:

$$\frac{\partial}{\partial y} \left\langle -\overline{u}\,\overline{v} + \nu \frac{\partial \overline{u}}{\partial y} - \tau_{12}^{sgs} \right\rangle - \frac{dP}{dx} = 0. \qquad (4.4)$$

If the above equation is integrated from the wall to a certain wall-normal position y, the following equation can be obtained:

$$\left\langle -\overline{u}\,\overline{v}|_y + \overline{u}\,\overline{v}|_0 + \nu \frac{\partial \overline{u}}{\partial y}\bigg|_y - \tau_{w1} - \tau_{12}^{sgs}|_y + \tau_{12}^{sgs}|_0 \right\rangle = \frac{dP}{dx}y. \qquad (4.5)$$

At the wall, under no-slip boundary condition, $\langle \overline{u}\,\overline{v}\rangle|_0 = 0$. At the channel center $y = H$, under the symmetry constriction, $-\langle \overline{u}\,\overline{v}\rangle|_H = 0$, $\langle \nu \partial \overline{u}/\partial y \rangle|_H = 0$ and

$-\langle \tau_{12}^{sgs} \rangle|_H = 0$, then Eq. 4.5 becomes

$$\langle \tau_{12}^{sgs} \rangle|_0 - \langle \tau_{w1} \rangle = \frac{dP}{dx} H, \qquad (4.6)$$

which means the pressure gradient is balanced not only by the wall shear stress, but also by the residual subgrid-shear stress on the wall $\tau_{12}^{sgs}|_0$. This residual subgrid stress denotes the modeling errors of subgrid-stress model on the wall. When the flow is highly resolved or the wall model is used, the normal relationship between the wall-shear stress and the pressure gradient, $-\langle \tau_{w1} \rangle = dP/dxH$, can be obtained. In coarse cases LES_CR1 and LES_CR3 having very large near wall grid cells, the wall-shear stress is heavily underpredicted. However, the residual subgrid-shear stress is so large that in order to maintain the constant mass flux, a large favorable pressure gradient is required, as shown in Tab. 4.1. The smaller is the wall-shear stress, the larger is the SGS-modeling error. Although the pressure gradient is large, it can be observed that in cases LES_CR1 and LES_CR3 the flows resemble those at lower Reynolds numbers, because the wall-normal position of maximum Reynolds normal stresses is shifted further away from the wall than those of DNS, as shown in Fig. 4.1(b). This means that some large artificial flow structures are created near the wall and drain much energy from the mean flow. The balance of the streamwise stresses is shown in Fig. 4.3(b), which indicates that for different cases the balance of modeled- and resolved-shear stress is crucial and the wall-shear stress is very important for streamwise momentum balance. Therefore, it can be concluded that the correct wall-shear stress is crucial to drive the required flow and that a well-modeled near-wall subgrid stress is also very important for the flow near-wall streamwise momentum balance. When the wall-layer flow dynamics are not resolved well large SGS-modeling error will be observed, which drive the flow into a unphysical state resembling a physical flow at much lower Reynolds number.

4.1.1.2 Coarse LES with wall models using van Driest damping

The results of coarse LES in the last subsection show that a wall model is required to account for the near-wall region and to provide a correct wall-shear stress in the momentum balance. In this section, wall models are used to supply the crucial

Table 4.2: Cases of coarse LES using wall modeling

case	Re_τ	$N_x \times N_y \times N_z$	C_G	N_{TBLE}	y_{c1}^+
wm_1	395	$16 \times 16 \times 16$	$HOMO$	20	24.7
wm_2	590	$16 \times 16 \times 16$	$HOMO$	20	36.9
wm_3	950	$16 \times 16 \times 16$	$HOMO$	20	59.4
wm_4	2,000	$16 \times 16 \times 16$	$HOMO$	20	125.0
wm_5	25,000	$32 \times 32 \times 32$	$HOMO$	30	1,562.5
wm_6	100,000	$32 \times 32 \times 32$	1.5	30	1,019.3

wall-shear stress, and the van Driest damping Eq. 2.31 is used near the wall in the SGS model. This damping function also influences the near-wall momentum balance through the implicitly modeled subgrid stress.

All three wall models are used to supply the wall-shear stress as an approximate boundary condition to exterior coarse LES at friction Reynolds numbers from $Re_\tau = 395$ up to 1.0×10^5. The boundary conditions are the same as for coarse LES without wall modeling in the streamwise and spanwise directions. The resolutions of all the cases are detailed in Tab. 4.2. In cases $wm_i(i = 1 \sim 5)$, the grids are equally distributed in three directions. In case wm_6, the Reynolds number is so high that the wall-normal grids are stretched near the wall using Eq. 4.1, and the grids in the other directions are equally distributed. The mean-velocity profiles of GWFP, WW and TBLE are shown in Fig. 4.4, 4.5, and 4.6, respectively. It can be seen that GWFP overpredicts wall-shear stress in cases $wm_{1\sim2}$ at relatively low Reynolds numbers, although this generalized wall function can take the viscous sublayer and buffer layer into account. In cases $wm_{3\sim5}$, it behaves better as expected, since the coupling points lie in the logarithmic region. Till $Re_\tau = 2000$, the mean-velocity profiles exhibit a long logarithmic region from first off-wall points. However, at higher Reynolds numbers, the mean-velocity profiles have mismatched logarithmic region and exhibit a near-wall artificial layer, especially for case wm_6, when the grids are stretched in the wall-normal direction. For the WW model, the mean velocity profiles in Fig. 4.5 are all underpredicted due to the overpredicted wall-shear stress. However, they also exhibit well-established logarithmic region at relatively low Reynolds numbers and curved mean-velocity profiles at higher Reynolds numbers as GWFP. The results of TBLE also have the same tendency of mean velocity profiles, while the difference is that TBLE
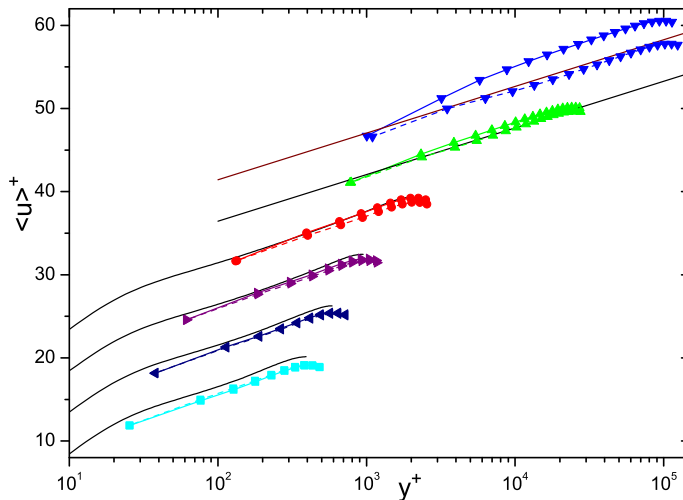
Figure 4.4: Mean velocity comparisons of cases $wm_i(i = 1 \sim 6)$ using GWFP from bottom to top, the velocity profiles are shifted upward by $(i-1)5$ for clarity. The solid lines: from bottom to top DNS at $Re_\tau = 395$ [126], $Re_\tau = 590$ [126], $Re_\tau = 950$ [42], $Re_\tau = 2,000$ [77] and the last two $\frac{1}{0.41}\ln(y^+) + 5.2$; solid lines with symbols: VD; dashed lines with symbols: CS.

can supply well-predicted wall-shear stress in the range of all Reynolds numbers. This means that TBLE can model different flow regions better than the other two models. In case wm_1, since the coupling point is in the buffer region and the logarithmic mean velocity starts from that point (this will be verified in the following subsection 4.1.1.4), the outer part of the mean velocity is somewhat underpredicted.

The local κ of cases $wm_{4\sim6}$ are shown in Fig. 4.7, since the mean-velocity profiles of these models behave similarly, only the results of TBLE are shown. It is obvious that, at several near-wall grid points, κ is heavily underpredicted, that is the gradient of mean velocity is too large. In the outer part, κ is overpredicted. From the underpredicted values to overpredicted ones, κ increases gradually away from the wall without obvious logarithmic region even in case wm_6 at very high Reynolds number.

Since tendency of κ is similar using three wall models which feed back different wall-shear stresses, it can be deduced that this phenomenon is caused by SGS-modeling error, especially at high Reynolds numbers. In order to assess
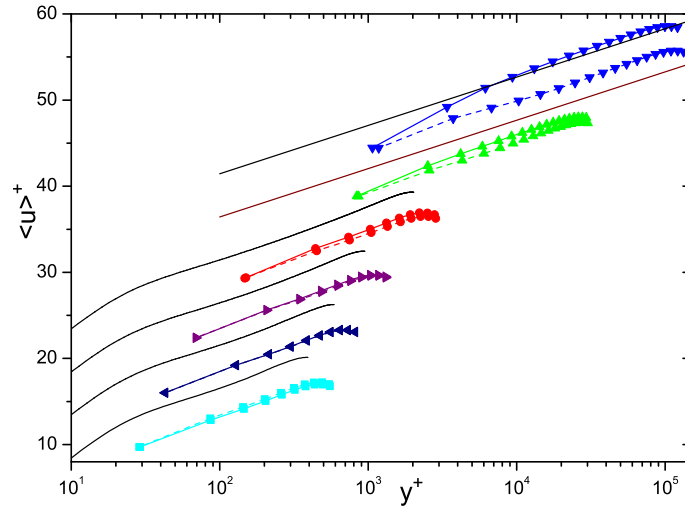
Figure 4.5: Mean velocity comparisons of cases $wm_i(i = 1 \sim 6)$ using WW from bottom to top, lines labeled as in Fig. 4.4.
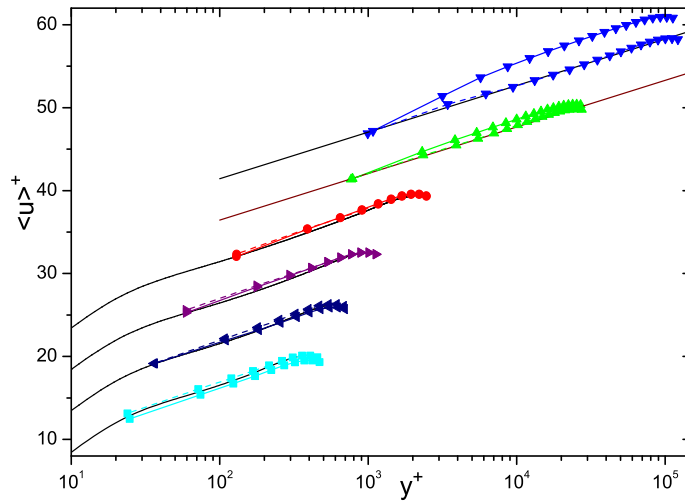

Figure 4.6: Mean velocity comparisons of cases $wm_i(i = 1 \sim 6)$ using TBLE from bottom to top, lines labeled as in Fig. 4.4.
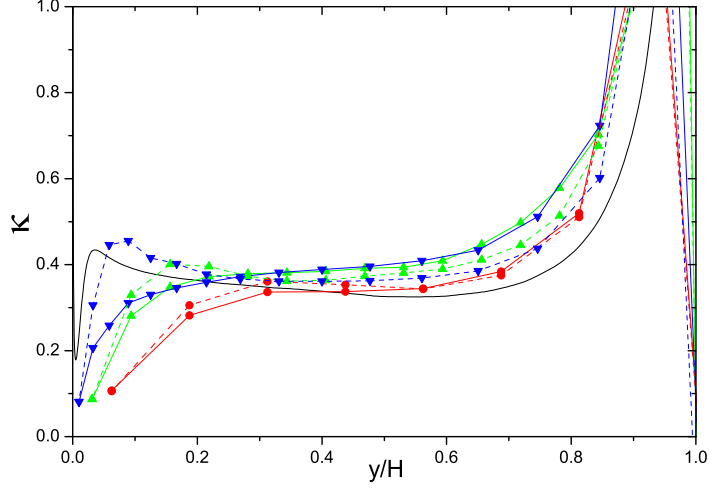
Figure 4.7: Local κ of cases $wm_i (i = 4 \sim 6)$ using TBLE, symbols denote different cases as in Fig. 4.4. Solid line: DNS at $Re_\tau = 2,000$ [77]; solid lines with symbols: VD; dashed lines with symbols: CS.

the different behavior at low and high Reynolds numbers and the difference between the homogenous and stretched grids, the balance of viscous, resolved and subgrid stresses is analyzed, as shown in Fig. 4.8, using TBLE wall model. At relatively low Reynolds numbers upto $Re_\tau = 2000$ in Fig. 4.8(a), the viscous stress is large at the first off-wall grid points, and decreases when the Reynolds number increases. Meanwhile, as the nondimensional wall distance y_{c1}^+ of the coupling position increases, the effect of damping function diminishes according to Eq. 2.31, hence, the subgrid stress increases (the implicit subgrid dissipation is approximately proportional to $\boldsymbol{\sigma}_{i,j,k}$ for homogeneous isotropic turbulence [69]). The resolved stress does not change much if the grid resolution is the same. This means that the subgrid stress becomes important in the near-wall momentum balance as the Reynolds number increases. At higher Reynolds numbers, the effect of viscous stress becomes trivial in the momentum balance, while the effect of modeled subgrid stress becomes large, especially at several near-wall cells, as shown in Fig. 4.8(b). As the large energy-containing structures depend weakly on Reynolds number outside of the wall layer, the resolved stresses increase as the grid resolution increases, comparing case wm_4 with cases $wm_{5\sim6}$ in Fig. 4.8(b). In case wm_6, although the wall-normal grid is stretched near the wall, the y_{c1}^+ is
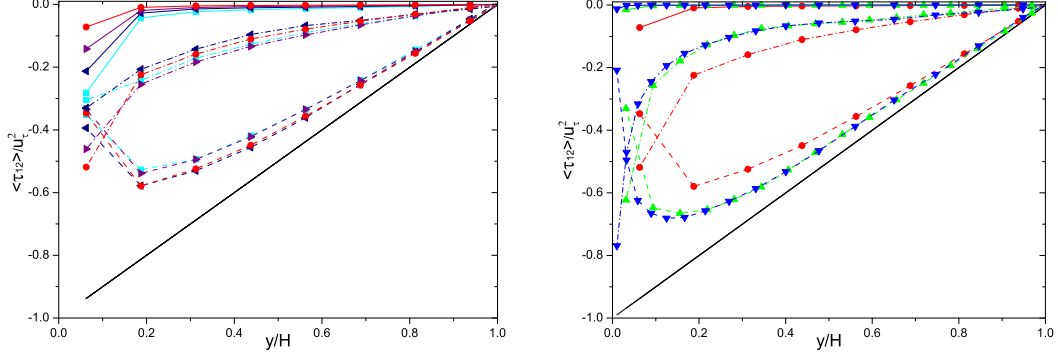
(a) Streamwise shear stress balance of case $wm_i(i = 1 \sim 4)$ for TBLE

(b) Streamwise shear stress balance of cases $wm_i(i = 4 \sim 6)$ for TBLE

Figure 4.8: Streamwise shear stress balance of case $wm_i(i = 1 \sim 6)$ for TBLE, symbols denote different cases as in Fig. 4.4. Solid line: total shear stress; solid line with symbols: viscous stress; dashed line with symbols: subgrid stress; dashdotted line with symbols: resolved shear stress.

still so large that the damping function cannot take the effect of the existence of the wall layer into account. On the other hand, the smaller grid size near the wall leads to an increase of the modeled implicit subgrid stress according to Eq. 2.30. The subgrid stress exhibits large values in several near-wall cells, which extracts energy from the mean flow and causes artifacts of the mean velocity profile in this region. From this analysis, one can concluded that an optimal method to alleviate the excessive subgrid dissipation near the wall is to use a physics based model for obtaining subgrid dissipation through a compensation of the implicit modeling parameter σ.

Although the prediction of the mean velocity has some deficiency at high Reynolds numbers, the Reynolds stresses are predicted reasonably well using the TBLE model at low and high Reynolds numbers, as shown in Fig. 4.9. The results of GWFP are almost the same as those of TBLE, except in the case wm_1, due to its overpredicted wall-shear stress. Since wall-shear stresses are overpredicted in all cases of WW, a large discrepancy of the resolved Reynolds stresses is observed. Therefore, the results of these two models are not shown.
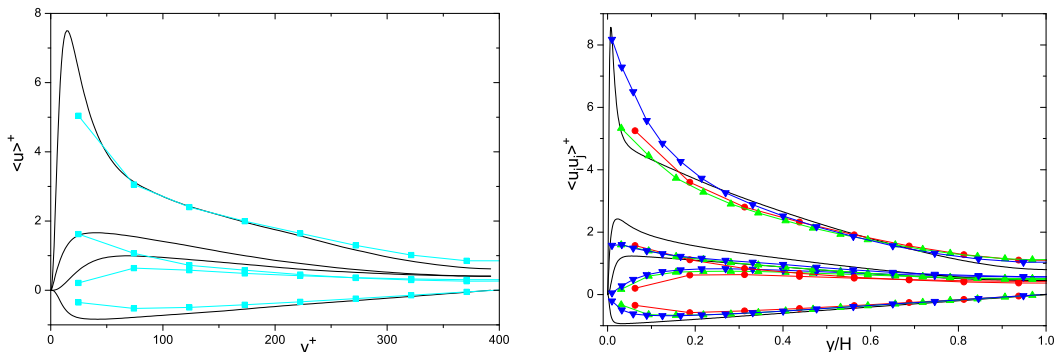
(a) Resolved Reynolds stresses comparison of case wm_1

(b) Resolved Reynolds stresses comparison of cases $wm_i (i = 4 \sim 6)$

Figure 4.9: Resolved Reynolds stresses comparisons of case $wm_i (i = 1, 4 \sim 6)$ for TBLE with those of DNS at $Re_\tau = 395$ [126] in Fig. 4.9(a) and DNS at $Re_\tau = 2000$ [77] in Fig. 4.9(b). Symbols denote different cases as in Fig. 4.4. Solid line: DNS; solid line with symbols: VD.

4.1.1.3 Coherent-structures based formulation

Motivated by the above analysis of the shear stress balance in the last subsection, an adaptive coefficient formulation of $\boldsymbol{\sigma}_{i,j,k}$ based on coherent structures [102, 103] is used to compensate the modeled subgrid stress without using a wall-damping function. Although the wall layer is not resolved and the detail of coherent structures is unavailable, it is the hope that large structures in the outer layer, such as the logarithmic layer, can be captured on a relatively coarse mesh, and that physically driven subgrid dissipation can be obtained. The detail of the formulation is presented in App. B. It is validated for TCF at $Re_\tau = 395$ and $Re_\tau = 590$ on a relatively coarse mesh with y_1^+ around 1. The mean velocity and resolved Reynolds stresses are predicted well, see APP. B.

This formulation of $\boldsymbol{\sigma}_{i,j,k}$ is adapted for wall-modeling LES. The results of cases wm_1 and wm_4 are shown in Fig. 4.10. It can be seen in Fig. 4.10(a) that the mean velocities no longer exhibit an artificial logarithmic region from the first off-wall grid point, their slopes are lower than those of DNS, and the wall-shear stresses are overpredicted using TBLE. The reason causing these results can be observed in Fig. 4.10(b) clearly. The coherent-structures based model
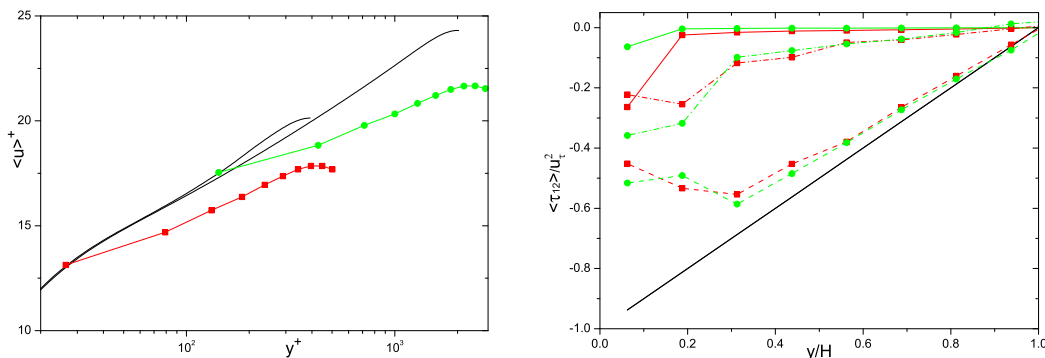
(a) Mean velocity comparison of cases wm_1 and wm_4 with DNS at $Re_\tau = 395$ [126] and $Re_\tau = 2000$ [77]. Solid lines: DNS; Solid line with square: wm_1; Solid line with circle: wm_4.

(b) Streamwise shear stress balance of cases wm_1 and wm_4. Line styles denote different stresses as in Fig. 4.8. Symbols denote different cases: square: wm_1; circle: wm_4.

Figure 4.10: Mean velocity and streamwise shear stress balance of cases wm_1 and wm_4 for CS without modification using TBLE.

returns smaller modeled subgrid stresses at the first off-wall grid point due to unphysical coherent structures there. For the balance of the streamwise shear stress, the wall-shear stress from the wall model is overpredicted according to Eq. 4.6. Therefore, an alternative to compensate this near-wall problem is using $\boldsymbol{\sigma}_{i,j,k}$ values at the second off-wall points to avoid the unphysical structures at the first off-wall grid points. This is based on the physical consideration that the resolved structures in logarithmic layer extend directly towards the wall without being altered by details of the wall layer. This coherent-structures based model is denoted as CS hereafter.

The mean-velocity profiles of cases $wm_i(i = 1 \sim 6)$ using CS combined with three wall models are also shown in Fig. 4.4, 4.5 and 4.6, respectively. All these results show that the mean velocities are predicted just as well as using VD at relatively low Reynolds numbers because of the domination of viscous stress, whereas they are much improved at higher Reynolds numbers, expecially for the case wm_6, with stretched wall-normal grids, since the effect of modeled subgrid stress becomes large in the near-wall momentum balance. Another observation is that the effect of wall models cannot be improved by the improved subgrid modeling, *i.e.* GWFP overpredicts wall shear stress at low Reynolds numbers and
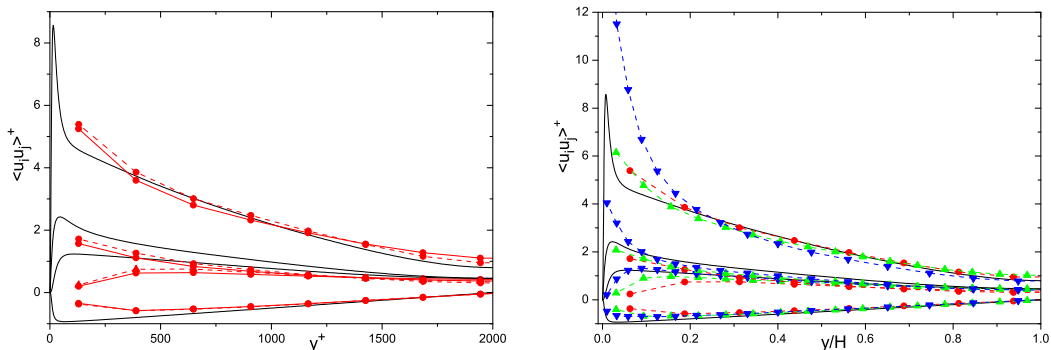
(a) Resolved Reynolds stresses comparison of case wm_4 using VD and CS with those of DNS[77].

(b) Resolved Reynolds stresses comparison of cases $wm_i(i = 4 \sim 6)$ using CS with those of DNS[77].

Figure 4.11: Resolved Reynolds stresses comparisons of case $wm_i(i = 4 \sim 6)$ using TBLE. Symbols denote different cases as in Fig. 4.4. Solid lines: DNS; solid lines with symbols: VD; dashed lines: CS.

WW overpredicts wall shear stress at all Reynolds numbers. On the other hand, it also confirms that even for advanced wall models satisfactory results cannot be obtained if the subgrid model is insufficiently accurate, especially near the wall. The subgrid modeling error should be taken into consideration when constructing a wall model for coarse LES. An improved wall model cannot eliminate the descrepancy caused by the SGS-modeling error.

The local κ of cases $wm_i(i = 4 \sim 6)$ using TBLE are compared with that of DNS at $Re_\tau = 2000$ and results of VD in Fig. 4.7. The values of κ at the first off-wall points are almost the same, while they extend more quickly to high values away from the wall using CS than using VD, and exhibit longer logarithmic region. In the outer layer the κ become smaller using CS and approach that of DNS.

Reynolds stresses of case wm_4 using CS and VD are compared with that of DNS in Fig. 4.11(a) using inner scaling for clarity. It can be observed that the Reynolds normal stresses are larger near the wall and smaller around channel center than those of VD. The Reynolds shear stress is almost the same. Therefore, the Reynolds stresses of CS is somewhat better than those of VD. For cases $wm_i(i = 4 \sim 6)$ using CS, the Reynolds stresses are compared with those of DNS

(a) Streamwise shear stress balance of case wm_5.

(b) Streamwise shear stress balance of case wm_6.

Figure 4.12: Streamwise shear stress balance comparisons of cases $wm_i(i = 5, 6)$ using VD and CS with TBLE. Line styles denote different stresses as in Fig. 4.8. Symbols denote different cases: circle : VD; uptriangle: CS.
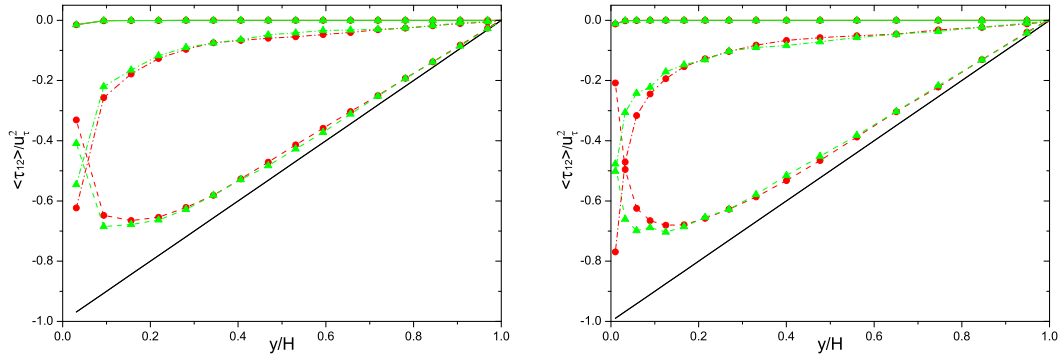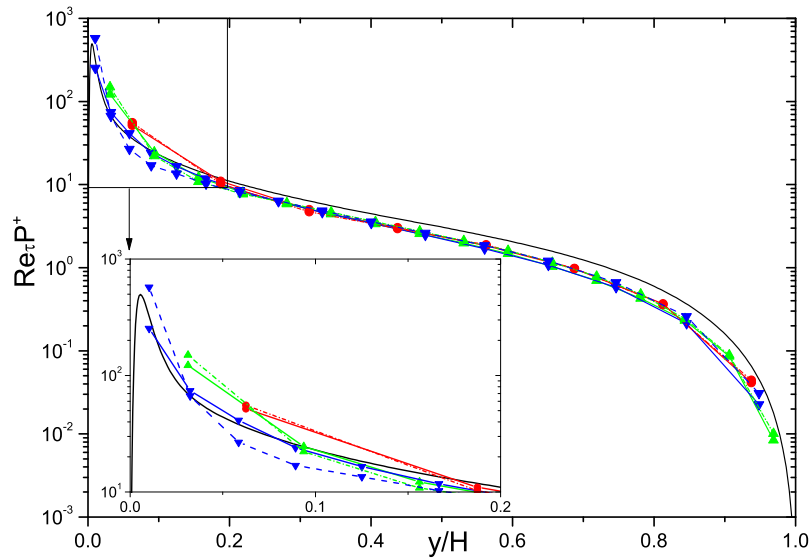

Figure 4.13: Local turbulence production of cases $wm_i(i = 4 \sim 6)$ using TBLE, symbols denote different cases as in Fig. 4.4. Solid line: DNS at $Re_\tau = 2,000$ [77]; solid lines with symbols: VD; dashed lines with symbols: CS.
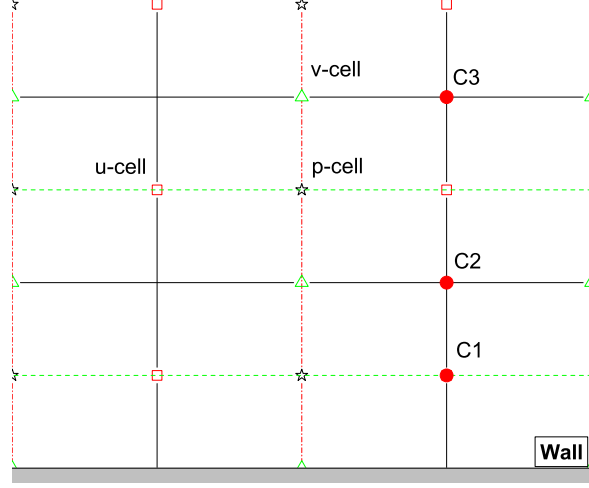
Figure 4.14:   Three different coupling positions.

Table 4.3: Cases with different coupling positions

case	$N_x \times N_y \times N_z$	y_{ci}^+	$-dP/dxH$	$\langle \tau_{w1} \rangle$	$-dP/dxH - \langle \tau_{w1} \rangle$
$R1C1$	$16 \times 16 \times 16$	24.7	3.219e-3	3.228e-3	-0.009e-3
$R1C2$	$16 \times 16 \times 16$	49.4	3.089e-3	3.123e-3	-0.034e-3
$R1C3$	$16 \times 16 \times 16$	98.8	3.360e-3	3.426e-3	-0.066e-3
$R2C1$	$32 \times 32 \times 32$	12.3	3.620e-3	3.629e-3	-0.009e-3

at $Re_\tau = 2000$ in outer scaling. At $y/H \geqslant 0.3$, the stresses scale well with the friction velocity. With increasing Reynolds number, the magnitude of Reynolds normal stresses at the first off-wall points increases, and is much larger than those of VD, as shown in Fig. 4.9(b). This can be attributed to the larger resolved shear stress using CS than using VD near the wall, as shown in Fig. 4.12 for cases $wm_i(i = 5 \sim 6)$, and is confirmed by the nondimensional turbulence production shown in Fig. 4.13.

From the comparison of the streamwise shear-stress balance in Fig. 4.12, one can see that the resolved shear stress is larger near the wall and that the modeled subgrid stress becomes smaller, while the viscous stress remains almost the same when CS is used. This trend confirms the fact that mean-velocity artifacts are caused by the overpredicted subgrid stress at several near-wall grid points.
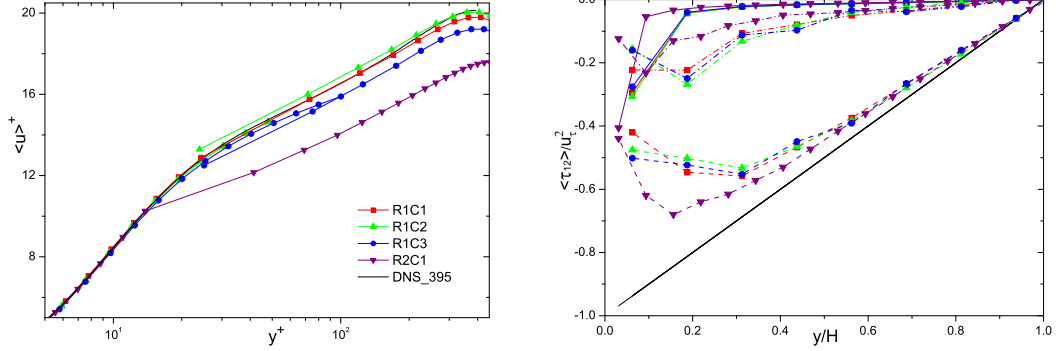
(a) Mean velocity profiles of inner TBLE and exterior LES.

(b) Streamwise shear stress balance. Line styles denote different stresses as in Fig. 4.8. Symbols denote different cases as in (a).

Figure 4.15: Influence of coupling position on mean velocity and streamwise shear stress balance.

4.1.1.4 Coupling position and parameters of the TBLE model

The effect of coupling position and modeling parameters of TBLE are investigated in detail in this subsection. Four cases using three coupling positions, as sketched in Fig. 4.14, are simulated on two grids with different resolutions at $Re_\tau = 395$, which are detailed in Tab. 4.3. 'R' refers to resolution, and 'C' to coupling position. The coupling positions reach from the buffer layer to the outer layer, according to the nondimensional wall distance. The results of the driving-pressure force, wall-shear stress and residual subgrid stress defined in Eq. 4.6 are also given in Tab. 4.3. When the TBLE model is used the residual subgrid stress in all cases are small and do not exceed 2% of the total driving-pressure force, which indicates that the effect of wall modeling compensates the SGS-modeling error, especially near the wall, through the momentum balance. A negative residual subgrid stress indicates turbulence production.

The results of mean-velocity profiles and streamwise shear-stress balance are shown in Fig. 4.15. It can be observed that the mean velocity exhibits a logarithmic region and starts from the first off-wall point, even when the coupling is far from the wall as in case $R1C3$ or is near the wall in the buffer region as in case $R2C1$. The mean velocity of exterior LES is constrained by the velocity of the inner TBLE at the coupling position. In case $R1C3$ the coupling position is

(a) Mean velocity profiles
(b) Local von Kármán constant κ
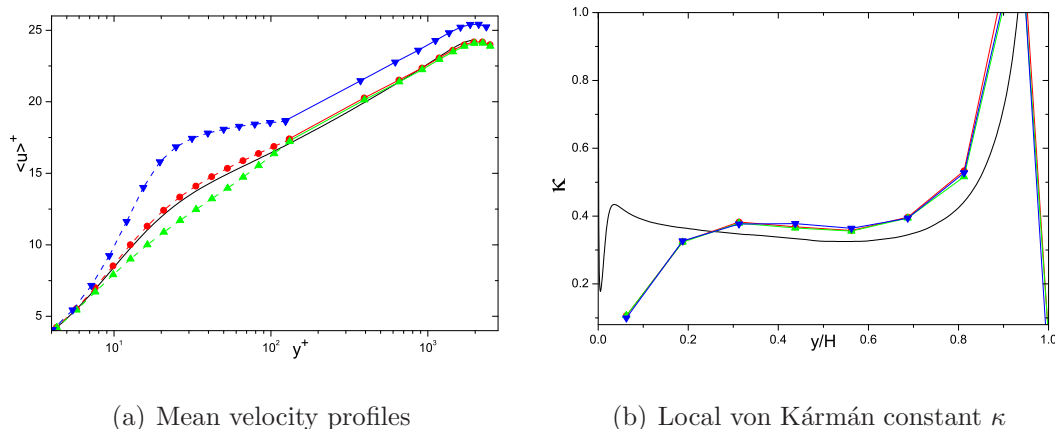
Figure 4.16: Effect of eddy-viscosity model on mean velocity and κ of coarse LES with TBLE model at $Re_\tau = 2000$. Solid lines: DNS; Solid lines with symbols: exterior LES; Dashed lines with symbols: inner TBLE. Circle: *eddy*1; uptriangle: *eddy*2; downtriangle: *eddy*3.

so far from the wall that the TBLE without convective terms cannot predict the outer part of the TBLE-region well. However, when the coupling position is too near the wall the wall-shear stress is overpredicted, as in $R2C1$, which leads to an underprediction of the mean velocity in wall units. From the comparison of the streamwise shear stress balance it can be observed that when the coupling position coincides with the first off-wall point the resolved shear stresses exhibit the same tendency as approaching the wall, compare $R1C1$ and $R2C1$. When the coupling point does not lie within the cell where the wall-shear stress is fed back the subgrid stress becomes small in the wall-adjacent cell, even though the viscous stresses are almost the same in these cases, compare $R1C1$, $R1C2$ and $R1C3$.

Therefore, it can be concluded that the coupling position should lie at the bottom of the logarithmic layer, neither far into the logarithmic layer, nor near in the buffer or viscous sublayer. It is better to locate the coupling point within the first off-wall cell, where the wall-shear stress is fed back to the exterior LES by a wall model.

To assess the effect of modeled dynamics of the wall layer better three different eddy-viscosity models for TBLE are investigated, using the same computational

(a) Reynolds shear stress

(b) Turbulence production
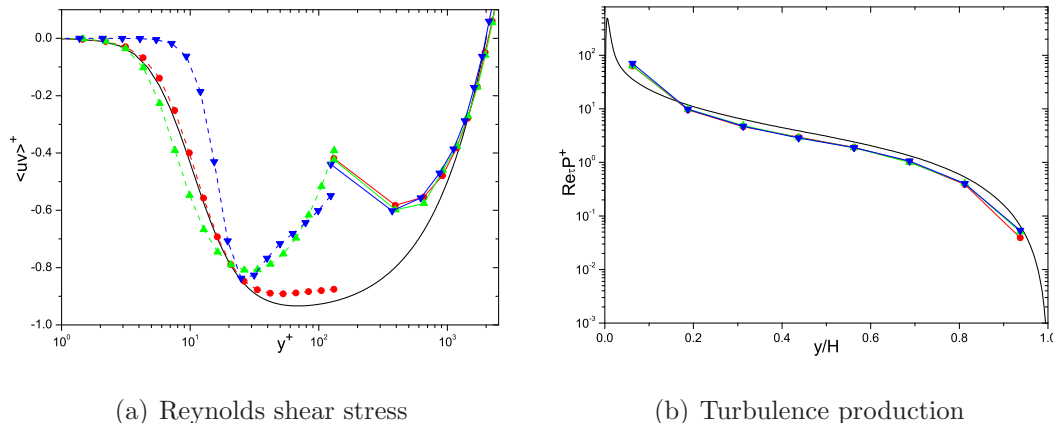
Figure 4.17: Effect of eddy-viscosity model on Reynolds shear stress and turbulence production for coarse LES with TBLE model at $Re_\tau = 2000$. Lines labeled as in Fig. 4.16.

condition as for case wm_4 in Tab. 4.2. The first eddy viscosity model is Eq. 3.19, denoted as $eddy1$. The second one is the Baldwin-Lomax model [11] which uses a two-layer formulation. The inner layer is based on the friction velocity scale, the outer layer is based on the velocity scale deduced from the vorticity. This model is denoted as $eddy2$. The last one is the formulation of E. Balaras *et al.* in Ref. [10] denoted as $eddy3$

$$\nu_t = (\kappa y)^2 |\overline{\mathbf{S}}|D, \quad D = [1 - exp(-(y^+/A)^3)], \tag{4.7}$$

where $|\overline{\mathbf{S}}|$ is the magnitude of the resolved strain at the coupling position, providing the velocity scale, and $A = 25$.

The comparisons of the mean-velocity profiles of inner TBLE and exterior LES are shown in Fig. 4.16(a). It can be observed that mean velocity of the inner TBLE using $eddy1$ is best. $Eddy3$ produces a too small wall-shear stress and fails to model the inner TBLE well. $Eddy2$ produces almost the same wall-shear stress as $eddy1$, although the outer part of TBLE is not predicted well. The exterior mean velocity exhibits a well-reproduced logarithmic region. From the comparison of local κ in Fig. 4.16(b), it can be seen that the exterior LES have almost uniform behavior. This is confirmed in Fig. 4.17 by the resolved shear stress and nondimensionalized turbulence production. It also can be observed in

(a) Mean velocity profiles
(b) Local von Kármán constant κ
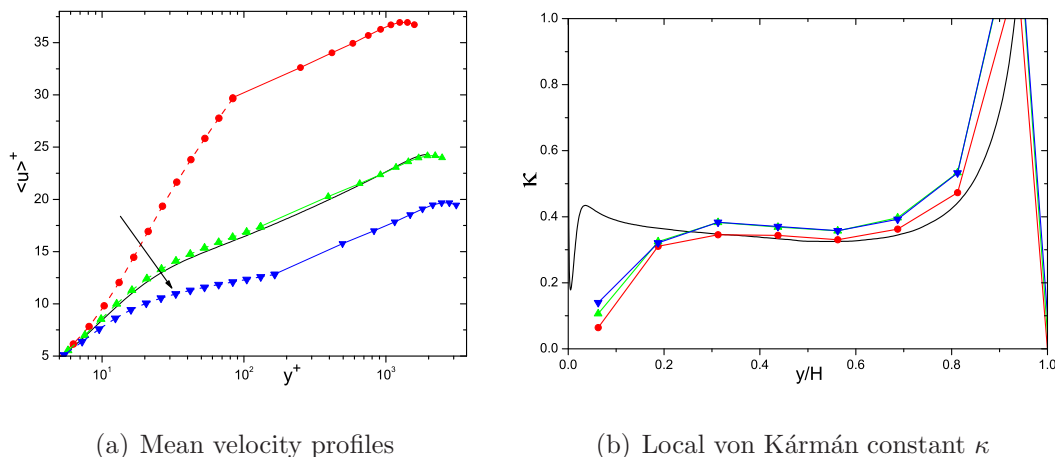
Figure 4.18: Effect of von Kármán constant κ in TBLE on mean velocity and local κ for coarse LES with TBLE model at $Re_\tau = 2000$. Solid lines: DNS; Solid lines with symbols: exterior LES; Dashed lines with symbols: inner TBLE. Circle: $K01$; uptriangle: $K04$; downtriangle: $K08$.

Fig. 4.17(a) that eddy-viscosity models $eddy2$ and $eddy3$ produce shear stress that approaches the resolved one at the coupling positions due to the different velocity scales based on the exterior LES in eddy-viscosity formulation.

The above analysis indicates that a key issue for a wall model is to provide the correct wall-shear stress, and that the exterior LES is not very sensitive to the details of near-wall turbulence modeling.

The effect of von Kármán constant is investigated for the eddy-viscosity model $eddy1$. Simulations are carried out as for the case wm_4 in Tab. 4.2. Three values $\kappa = 0.1$, 0.4, and 0.8 are used, which are denoted as $K01$, $K04$ and $K08$, respectively. From a comparison of mean-velocity profiles of inner TBLE and exterior LES in Fig. 4.18(a) it can be seen that a larger κ corresponds to a larger wall-shear stress, while the exterior LES also exhibits well-predicted logarithmic region for different eddy-viscosity models, indicted by local κ in Fig. 4.18(b). In case $K01$ the local κ is smaller than for the other two cases using a larger von Kármán constant. The difference of the wall shear stress is large, which causes the flow dynamics at the first off-wall points of exterior LES to be much different. It also results in a large turbulence production and a viscous shear stress as shown in Fig. 4.19 at first off-wall point. Through the balance of the streamwise shear

78
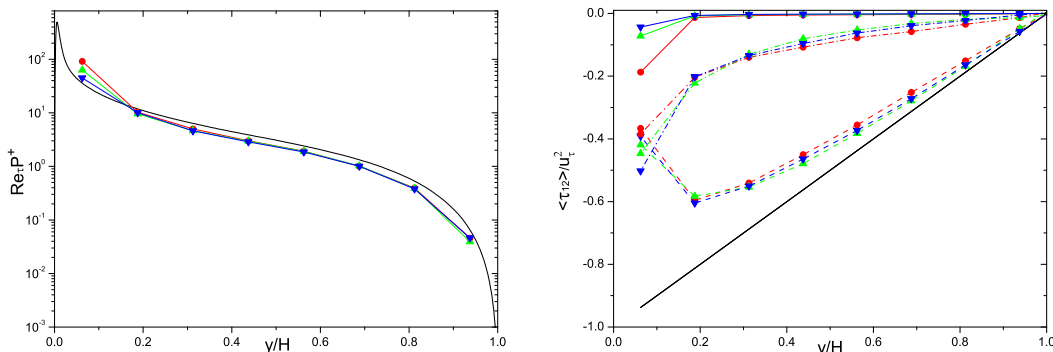
(a) Turbulence production. Solid lines: DNS; Solid lines with symbols: exterior LES.

(b) Streamwise shear stress balance. Line styles denote different stresses as in Fig. 4.8.

Figure 4.19: Effect of von Kármán constant κ in TBLE on turbulence production and streamwise shear stress balance for coarse LES with TBLE model at $Re_\tau = 2000$. Circle: $K01$; uptriangle: $K04$; downtriangle: $K08$.

stress the subgrid stress is also different.

Therefore, it can be concluded that κ in TBLE mainly affects the wall-shear stress. Through the much different wall-shear stresses the flow dynamics of the exterior LES is also affected, mainly at the first-off wall point.

4.1.1.5 Effect of grid resolution

The grid resolution of the exterior LES is investigated in this subsection. Although a grid convergence study can not be carried out as with traditional RANS, we need to check whether the resolved part of the flow is improved when the resolution increases in the context of wall modeling. Three cases with different resolutions are considered at $Re_\tau = 2000$ using TBLE, as shown in Tab. 4.4. The results of driving pressure force, wall shear stress and residual subgrid stress are also shown in the table. For all these three cases, the residual subgrid stress is very small, which indicates that the flows are well established with different grid resolutions.

The results of mean velocity and local κ are compared in Fig. 4.20. As the resolution increases, the first off-wall point approaches the wall, but it is still outside of the buffer layer. The well established logarithmic regions extend

Table 4.4: Cases with different resolutions at $Re_\tau = 2000$

case	$N_x \times N_y \times N_z$	y_{c1}^+	$-dP/dxH$	$\langle \tau_{w1} \rangle$	$-dP/dxH - \langle \tau_{w1} \rangle$
$R1$	$16 \times 16 \times 16$	125	2.061e-3	2.055e-3	0.006e-3
$R2$	$32 \times 32 \times 32$	62.5	2.039e-3	2.033e-3	0.006e-3
$R3$	$48 \times 48 \times 48$	41.7	2.043e-3	2.044e-3	-0.001e-3
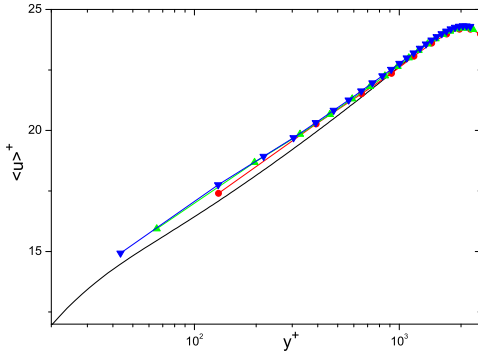
(a) Mean velocity profiles
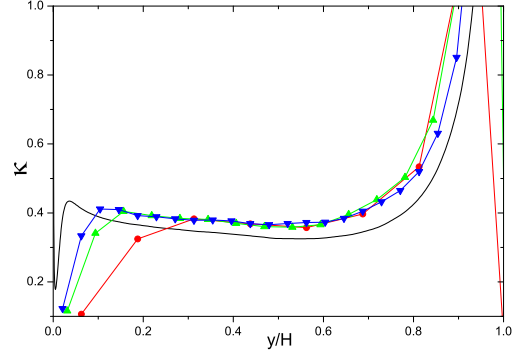
(b) Local von Kármán constant κ

Figure 4.20: Effect of resolution of exterior LES on mean velocity and local κ with TBLE model at $Re_\tau = 2000$. Solid lines: DNS; Solid lines with symbols: exterior LES; Circle: R1; uptriangle: R2; downtriangle: R3.
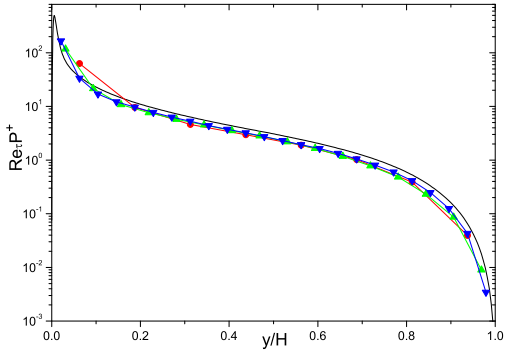
(a) Turbulence production. Solid lines: DNS; Solid lines with symbols: exterior LES.
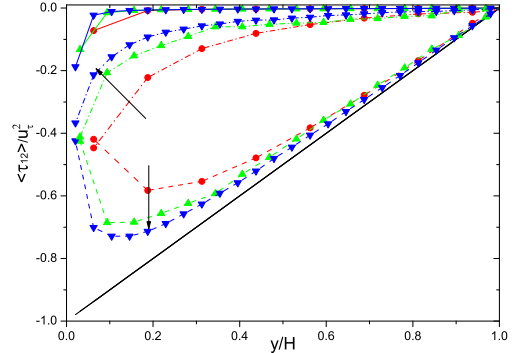
(b) Streamwise shear stress balance. Line styles denote different stresses as in Fig. 4.8.

Figure 4.21: Effect of resolution of exterior LES on turbulence production and shear stress balance for coarse LES with TBLE model at $Re_\tau = 2000$. Circle: R1; uptriangle: R2; downtriangle: R3. Arrows point to the direction increasing resolution.

towards the wall and leave the outer part unchanged, which is indicated clearly by the local κ in Fig. 4.20(b). It can also be observed that κ is not exactly constant with increasing resolution, but approaches the DNS.

The resolved-turbulence production also approaches that of DNS near the wall when the resolution is increased. The outer part is improved a little although it is still underpredicted, as shown in Fig. 4.21(a). This can be attributed to the increased resolved shear stress, as shown in Fig. 4.21(b). By the streamwise shear-stress balance the modeled subgrid stress decreases, when the resolution increases. And the viscous stress becomes large when the first off-wall point approaches the wall.

From the above results we can see that the resolved part of the turbulence increases as the resolution increases in the context of wall modeling. As long as the requirement of wall modeling is satisfied consistent results can be obtained.

4.1.2   Investigation of backward-facing step flow

The considered computational domain extends in streamwise direction to $40H$, where H is the step height, including a section of $10H$ upstream of the step. The height is $6H$ at the outlet, the spanwise width is $3H$, and an expansion ratio is 1.2, as shown in Fig. 4.22. The computational domain is divided into three blocks at the step, which are discretized by $192 \times 32 \times 24$ cells, with 48 cells upstream of the step and 8 cells in the step. In the streamwise direction the grids are refined near the location of the step. The recycling inflow technique and the outflow boundary condition as described in section 2.4.1 are applied in the streamwise direction. The recycling length is more than 5 times of the boundary layer thickness at the inlet. A symmetry boundary condition is used at the upper boundary. A periodic condition is used in the spanwise direction. At the wall, alternatively a no-slip condition (LES resolution not resolving the near-wall flow) and three different wall models are used. The resolution of the locally embedded TBLE is 20 for all cases, and the grids are stretched near the wall. The coupling position at first off-wall point is about $y_{c1}^+ = 50$, based on the local friction velocity at inlet. These cases are denoted as LES_CS, WM_GWFP, WM_WW and WM_TBLE, respectively. In all cases, the pressure Poisson equation is solved
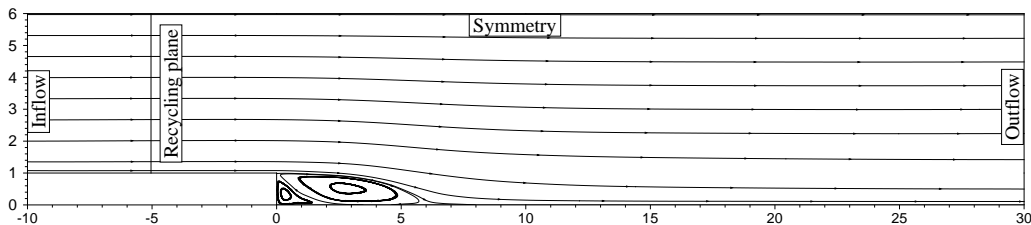
Figure 4.22:   Sketch of the backward-facing step.

Table 4.5: Reattachment position and the size of secondary separation bubble

case	x_r/H ($C_f = 0$)	x_r/H ($\chi = 0.5$)	$x_{s2}/H \times y_{s2}/H$
LES_CS	5.40	5.40	0.75×0.70
WM_GWFP	5.65	5.65	0.30×0.35
WM_WW	5.81	5.81	0.60×0.50
WM_TBLE	7.40	5.80	N/A

using a fast Fourier transform in the spanwise direction, and a two-dimensional BiCGStab iterative solver for the other directions. The simulation is carried out for 10 flow-through times until the statistical steady state is reached. Statistics are collected during the last 6 flow-through times.

4.1.2.1   Global flow quantities

As the Reynolds number $Re_H = 5100$ based on the step height is relatively low, the results of the original VD and of CS are indistinguishable. Therefore, only the results obtained using CS are presented. The reattachment length x_r/h of these four cases indicated by the location of zero mean friction coefficient and the backward-flow-time ratio $\chi = 50\%$ at the first off-wall points are shown in Tab. 4.5. In the cases LES_CS, WM_GWFP and WM_WW both criteria are equivalent because the mean-wall stress is calculated directly from the velocity at the first off-wall point. In case WM_TBLE, the wall-shear stress is calculated from the velocity at the first off-wall point of the embedded TBLE, and the back-flow-time ratio is calculated from the velocity at the first off-wall point of the exterior LES. This difference is partially responsible for the rather large discrepancy. These reattachment lengths are all quite different from the experiment $x_r/h = 6.0 \pm 0.15$ [91]. The predicted reattachment length strongly depends on
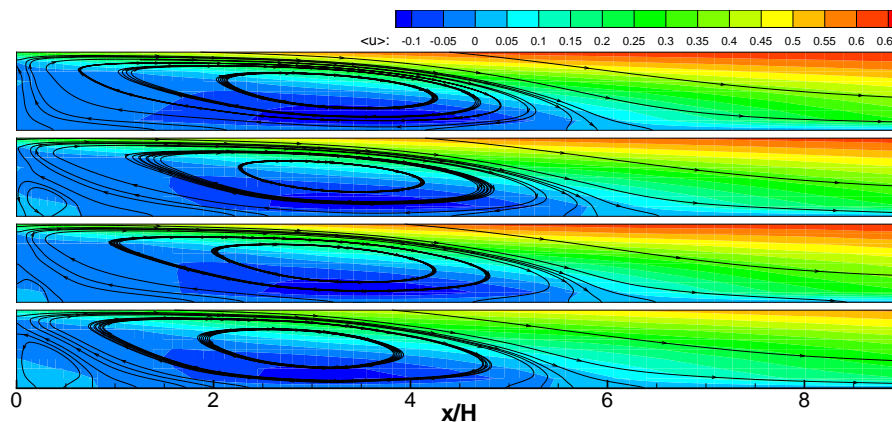
Figure 4.23: Global flow fields comparison of coarse LES and wall models downstream of the step. From bottom to top: WM_LES, WM_GWFP, WM_WW and WM_TBLE.

the boundary layer upstream of the step and on the effective dissipation in the recirculation region. In the case LES_CS the boundary layer upstream of the step is not predicted correctly due to the coarse resolution. In wall-modeling cases, although the outer part of incoming boundary layer is more accurate (see below), the wall model is still insufficient for an accurate prediction of the recirculation region.

The DNS of Le *et al.* [108] shows that a second recirculation occurs at the lower corner of the step and its size is $1.76H \times 0.8H$ in streamwise and vertical directions. For coarse LES without wall modeling and for wall-modeling cases the sizes of the secondary-separation bubble $x_{s2}/H \times y_{s2}/H$ are also shown in Tab. 4.5. The largest one is observed in case LES_CS, while in the wall-modeling cases it becomes smaller, and there is no secondary-separation bubble in case WM_TBLE, as compared in Fig. 4.23. Its size is much different in cases WM_GWFP and WM_WW. In WM_TBLE the main recirculation is strong and extends all the way to the step, a similar behavior has been reported in Ref. [25] for all kinds of wall models used there and for coarse LES without wall model. These observations support the conclusions that the occurrence of the secondary-recirculation bubble rather depends on the SGS-modeling quality than on the grid resolution and is very sensitive to the wall model. It also shows that the wall models are unable to correctly recover such effects.

(a) Friction-coefficient comparison

(b) Pressure-coefficient comparison
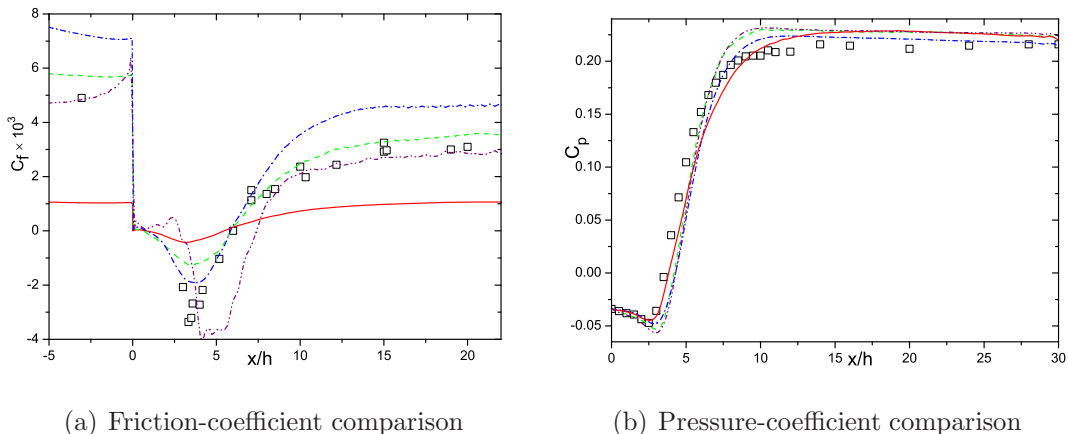
Figure 4.24: Friction- and pressure-coefficient comparisons of experiment, coarse LES and wall models. Square symbol: EXP [91]; Solid line: LES_CS; dashed line: WM_GWFP; dashdotted line: WM_WW; dashdotdotted line: WM_TBLE.

The friction- and pressure-coefficient distributions

$$C_f = \frac{\tau_w}{\frac{1}{2}\rho U_0^2}, \quad C_p = \frac{p - p_0}{\frac{1}{2}\rho U_0^2}, \tag{4.8}$$

are compared in Fig. 4.24(a) and Fig. 4.24(b), respectively, where p_0 is the reference pressure taken at $x/H = -5.1$ upstream of the step. U_0 is the upstream reference velocity at $x/H = -3.05$, defined following the experiment [91], which is also used to scale the mean velocity and Reynolds stresses. From the C_f distribution, it can be seen that C_f is strongly underpredicted in the case LES_CS, as expected. At $x/H = -3.05$ upstream of the step the boundary layer develops under the influence of a weak favorable pressure gradient. The C_f upstream of the step is predicted well by the TBLE model, while GWFP and WW overpredict the wall-shear stress as for the simulations of TCF. In the recirculation region all wall models fail to recover the correct C_f. In cases WM_GWFP and WM_WW, the wall shear stress is underpredicted and has positive values near the step, which is consistent with the observed small secondary-separation bubble. In case WM_TBLE in the front part of the recirculation a weak favorable pressure gradient causes the wall friction become positive. In the rear part, the overpredicted adverse pressure gradient results in a negative C_f farther downstream than in the

experiment. Therefore, it can be deduced that in the embedded TBLE there is a secondary-separation bubble, however, the positive wall-shear stress can not drive the mean flow in the exterior LES to reproduce a secondary-separation bubble. It can be concluded that the wall friction is dominated by the pressure gradient when using the simplified TBLE, and that the prediction deficiency may be related to the neglected convection terms. In the recovery region C_f is predicted well by TBLE, and is slightly overpredicted by GWFP, but is heavily overpredicted by WW, which is also similar to the results of the TCF computations at low Reynolds numbers.

As shown in the C_p distribution, the pressure recovers more quickly in the wall-modeling cases than in LES_CS. The pressure of the rear part of the recirculation is lower in the wall-modeling cases than in LES_CS, which indicates stronger recirculations in the former cases. However, downstream of the position $x/h = 14$ the pressure coefficients are almost the same for all cases, except for WM_WW. Although the wall-shear stress is heavily overpredicted in this case, the recovery of the pressure is reasonably accurate compared with the experiment.

It can be learned from the comparison of the global flow quantities that the secondary flow is much more sensitive to a wall model than the main flow features, and different wall models result in much different wall-shear stress due to different modeled near-wall flow dynamics.

4.1.2.2 Mean-velocity profile and Reynolds stresses

The mean velocities and Reynolds stresses are compared in Fig. 4.25 and 4.26 at six streamwise stations. At station $x/H = -3.1$ upstream of the step the flow resembles a developed turbulent boundary layer under a weak favorable pressure gradient. In the wall-modeling cases the mean streamwise velocities and Reynolds stresses are well predicted outside of the wall layer at this station. The mean vertical velocity is not well predicted in all cases at all positions. In LES_CS the mean steamwise velocity is underpredicted near the wall but overpredicted away from the wall. The position of the maximum streamwise Reynolds normal stress is shifted farther away from the wall, which resembles flow at lower Reynolds number such as the results for coarse LES of TCF without wall modeling. The
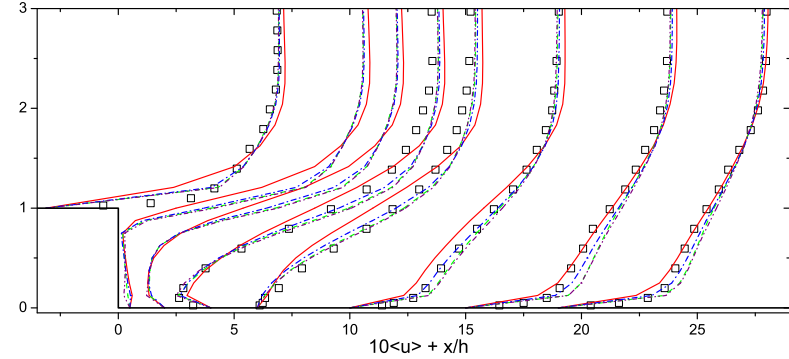
(a) Steamwise mean velocity
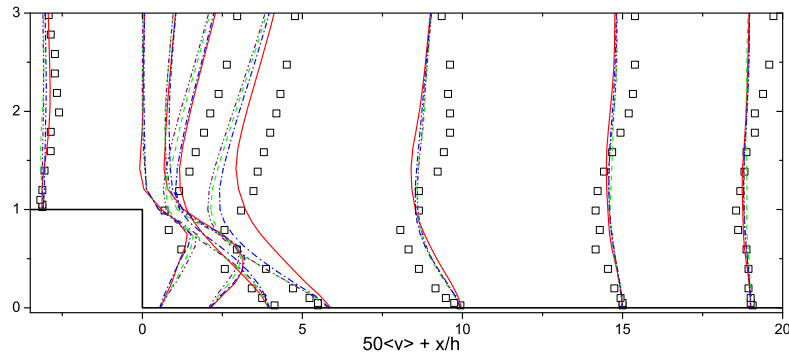
(b) Vertical mean velocity

Figure 4.25: Mean velocity comparisons of experiment, coarse LES and wall models. Lines labeled as in Fig. 4.24.

other two Reynolds stresses are predicted well.

At the location $x_1/h = 4.0$, in the recirculation bubble the maximum mean backflow velocity is underpredicted in LES_CS, which is consistent with its too short reattachment length and slow pressure recovery. For the wall-modeling cases the coupling positions are approximately at the locations of the maximum backflow velocity. Beneath those locations the turbulence production in the real flow is very small [2]. The mixing-length eddy-viscosity model using Eq. 3.19, however, introduces a rather strong turbulence production in the TBLE and fails to represent this kind of flow. The other two wall models provide too small wall-shear stress as shown in Fig. 4.24(a). Although the three wall models behave much differently the differences of the mean velocity profile and Reynolds stresses are small.

At reattachment and further downstream the prediction of mean streamwise velocities and Reynolds stresses is generally improved by wall models, except at the far-downstream stations. It can be seen that in the wall-modeling cases the flow recovers too quickly after the reattachment, as shown in Fig. 4.25(a) and 4.26(a). In the rear part of the recovery region, although the pressure gradient is almost zero, the boundary layer is far from well-developed [91, 108]. An inner boundary layer develops near the wall, and the outer flow is still affected by the evolution of the free shear layer that has experienced a strong adverse pressure gradient. The mixing length and eddy viscosity are much larger than the one obtained using Eq. 3.19 with $\kappa = 0.4$ [90]. This fact results in an underprediction of the wall-shear stress using TBLE, as in Fig. 4.24(a). Thus, the flow recovers too fast with an overpredicted mean velocity. And this can also explain that the overpredicted wall-shear stress in case WM_WW results in an improved pressure and mean-streamwise-velocity predictions in the recovery region.

Even the very simple WW model can improve the prediction of the mean flow quantities. The mean velocity and Reynolds stresses are not very sensitive to the wall-shear stress provided by different wall models. The secondary flow features are much more sensitive to near-wall modeling. Compared with GWFP and WW TBLE can reproduce more flow dynamics, including the effects of pressure gradient on the near-wall momentum balance and the near-wall turbulence, however, it prevents the development of the secondary-separation bubble. In different flow regions, the requirement of the wall modeling is different, and all three wall models fail to reproduce the separation process accurately.

4.1.3 Conclusions regarding wall modeling on body-fitted meshes

From the above investigation of the canonical TCF and flow along the backward-facing step the following can be learned for coarse-mesh LES and wall modeling. For coarse LES without wall modeling large residual subgrid modeling errors result in the near-wall relatively large cells since the dynamics of the wall layer cannot be resolved. The wall-shear stress is under predicted in both types of flows, as expected. When wall models are applied the flows are much improved
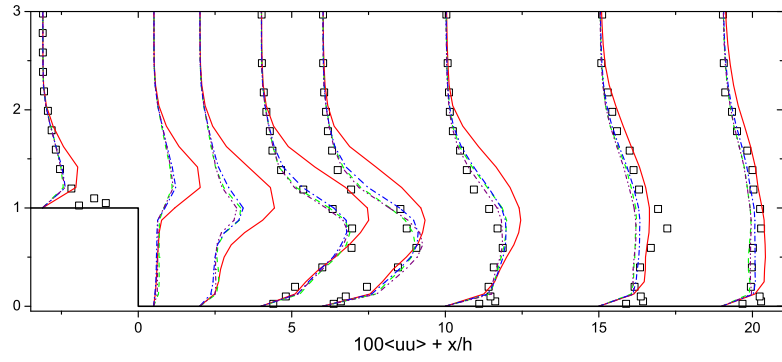
(a) Streamwise Reynolds normal stress
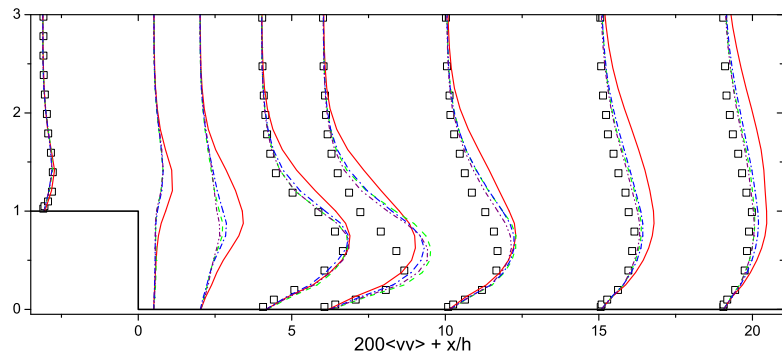
(b) Vertical Reynolds normal stress
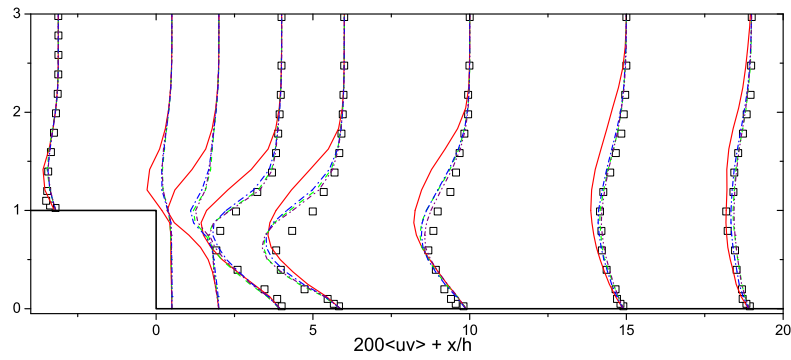
(c) Reynolds shear stress

Figure 4.26: Reynolds stress comparisons of experiment, coarse LES and wall models. Lines labeled as in Fig. 4.24

concerning the mean flow features and near-wall momentum balance up to moderately large Reynolds numbers. As the Reynolds number increases the modeled subgrid stress becomes much more important. The near-wall subgrid modeling error leads to a large discrepancy of the mean flow quantities near the wall. This modeling error is almost independent of wall models and cannot be improved by them. Even for improved subgrid modeling the characteristics of wall models are not effected. Therefore, the near-wall modeling errors of subgrid modeling and wall modeling should be distinguished and diminished separately. As feedback of a wall model the wall-shear stress is much more crucial for obtaining reasonable physical flows. However, modeling parameters in wall models have less effect on the exterior LES, except at the first off-wall grid points. In TCF, the TBLE performs best within the Reynolds-number range, and GWFP behaves well at large Reynolds numbers, while WW always overpredicts the wall-shear stress.

In the much more complex backward-facing step case, three wall models act in the attached-flow region as in TCF, while significant differences are observed in the recirculation region. Although WW overpredicts wall friction before the step and after the reattachment, it results in a better secondary-flow features and mean-velocity profiles in the recovery region compared with GWFP and TBLE. Therefore, it is not obvious which wall model is superior to the others. All three wall models do not lead to satisfactory results for the massive separation.

4.2   Wall modeling for canonical flows with CIIM

As the main intention is to use wall models in conjunction with implicit LES and the conservative immersed interface method for complex geometries, it is sensible to test this combination first on these two simple configurations, TCF and backward-facing step.

4.2.1   Turbulent channel flow using CIIM

First, a channel flow at $Re_\tau = 395$ using TBLE is considered. The physical domain is $2\pi H \times 2H \times \pi H$ and is immersed in a computational domina of size $2\pi H \times 2.375H \times \pi H$, with the near-wall cells cut, as sketched in Fig. 4.27.

Figure 4.27: Computational domain and immersed interfaces of TCF. Thick solid lines: immersed interfaces.

(a) Mean velocity profile

(b) Reynolds stresses
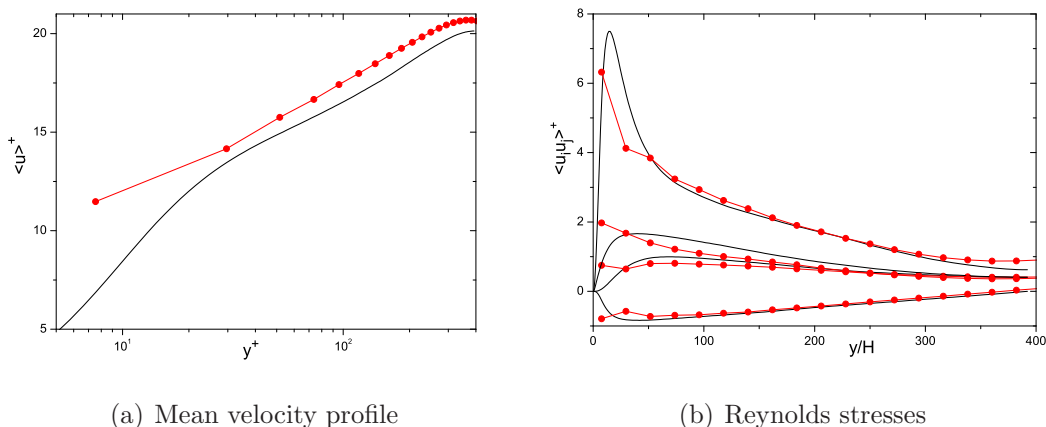
Figure 4.28: Comparisons of mean velocity and Reynolds stresses of coarse LES using TBLE with CIIM at $Re_\tau = 395$. Solid lines: DNS; solid lines with symbols: exterior LES.

The resolution is $32 \times 40 \times 32$ in three directions respectively. Periodic boundary conditions are applied in the streamwise and the spanwise directions, and the wall model is used at both immersed interfaces. The nondimensional wall distance of the coupling position is $y_c^+ = 47$. And the CS formulation is used.

The mean velocity compared with that of DNS [126] is shown in Fig. 4.28(a). Since the wall-shear stress is underpredicted the scaled mean velocity is over-predicted. Besides, it can be observed that the mean velocity at the cut cell is large than the expected logarithmic values as in body-fitted case. From the Reynolds stress comparison in Fig. 4.28(b), the Reynolds stress components are

(a) Turbulence production. Solid lines: DNS; solid lines with symbols: exterior LES.

(b) Streamwise shear stress balance. Line styles denote different stresses as in Fig. 4.8.

Figure 4.29: Turbulence production and streamwise shear stress balance of coarse LES using TBLE with CIIM at $Re_\tau = 395$.

all overpredicted in the cut cell. This is confirmed by the turbulence production, as shown in Fig. 4.29(a). By analysis of streamwise shear-stress balance in Fig. 4.29(b), it is evident that the mean resolved-shear stress is abnormal in the cut cell, and the modeled subgrid stress becomes positive there. This means that the modeled shear stress does not extract energy from the mean flow, but injects energy into the mean flow. The reason is the artificial momentum mixing at the wall that is employed to small cut cells. This phenomenon occurs at all relatively low Reynolds numbers upto $Re_\tau = 950$. At higher Reynolds numbers the wall stress and mean flow quantities are predicted better as will be presented in the following.

To limit the contamination of the momentum mixing near the cut cells a finer grid resolution $48 \times 48 \times 48$ in three directions is used for three high Reynolds numbers, $Re_\tau = 2000$, 25000 and 100000. The grids are equally distributed. The boundary conditions are the same as the case at $Re_\tau = 395$. The coupling position is a vertical-cell size away from the wall.

Three wall models are all evaluated. The mean velocity profiles and Reynolds stresses are compared in Fig. 4.30. The GWFP performs as well as on a body-fitted mesh at these large Reynolds numbers, as shown in Fig. 4.30(a) and Fig. 4.30(b). At $Re_\tau = 25000$ and 100000 the wall-shear stresses are slightly underpre-

(a) Mean velocity profile using GWFP

(b) Reynolds stresses using GWFP

(c) Mean velocity profile using WW

(d) Reynolds stresses using WW

(e) Mean velocity profile using TBLE

(f) Reynolds stresses using TBLE
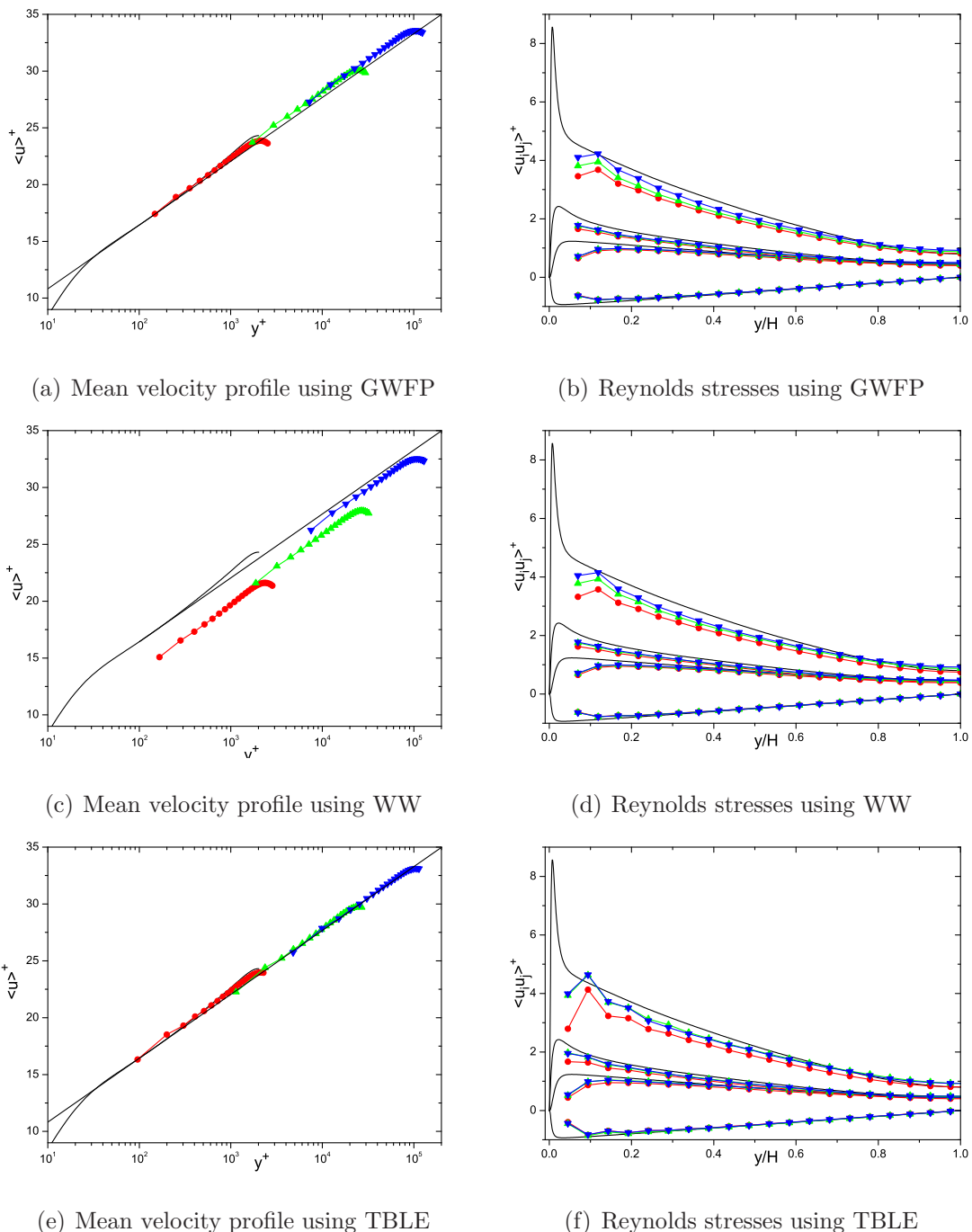
Figure 4.30:   Comparisons of mean velocity and Reynolds stresses of coarse LES using wall models with CIIM. Solid lines: DNS at $Re_\tau = 2000$; solid lines with symbols: exterior LES; circle: $Re_\tau = 2000$; uptriangle: $Re_\tau = 25000$; downtriangle: $Re_\tau = 100000$.
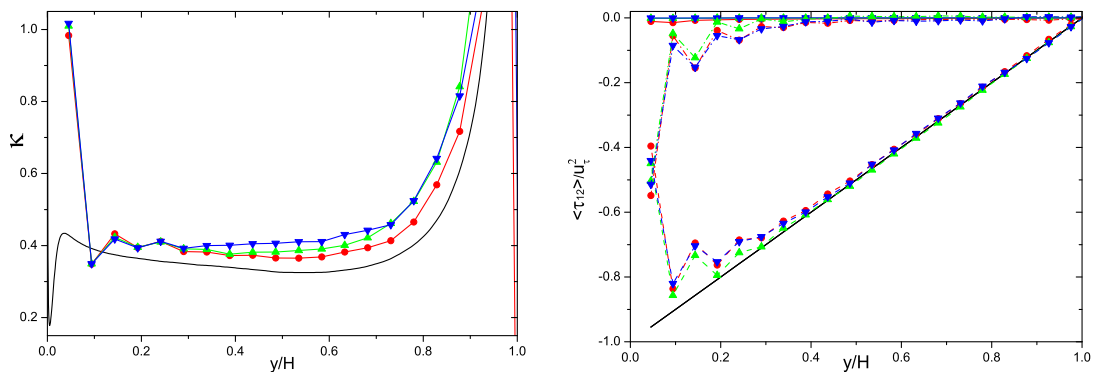
(a) Local von Kármán constant κ. Solid lines: DNS at $Re_\tau = 2000$; solid lines with symbols: exterior LES.

(b) Streamwise shear stress balance. Line styles denote different stresses as in Fig. 4.8.

Figure 4.31: Comparisons of Reynolds stress and streamwise shear stress balance of coarse LES using TBLE with CIIM. Symbols denote different cases as in Fig. 4.30.

dicted, which results in overprediction of mean velocities in wall units. Reynolds stresses are predicted well, but do not show Reynolds dependence near the wall as in Fig. 4.11(b) using body-fitted grids. The WW still overpredicts wall-shear stress at all Reynolds numbers in Fig. 4.30(c) as body-fitted cases in Fig. 4.5. However, the overprediction becomes smaller with inreasing Reynolds number. This is similar to the behavior of GWFP in the framework of CIIM. Although the scaled Reynolds stress is predicted well using the outer length scale, as shown in Fig. 4.30(d), the flows exhibit a much larger friction Reynolds numbers due to the overpredicted wall-shear stress.

The TBLE performs much better than GWFP and WW concerning the mean velocity profiles, as shown in Fig. 4.30(e). It can be seen in Fig. 4.31(a) that the local κ is overpredicted at first off-wall grid point, and that this tendency is almost the same at these three high Reynolds numbers. This can be attributed to the uniform artificial momentum mixing. The Reynolds-stress comparison in Fig. 4.30(f) shows that the profiles at two higher Reynolds numbers are almost the same, while the values at $Re_\tau = 2000$ is small. The streamwise shear-stress balances in Fig. 4.31(b) show oscillations of the resolved shear stress and the modeled subgrid stress. This can explain the Reynolds stress oscillation in several
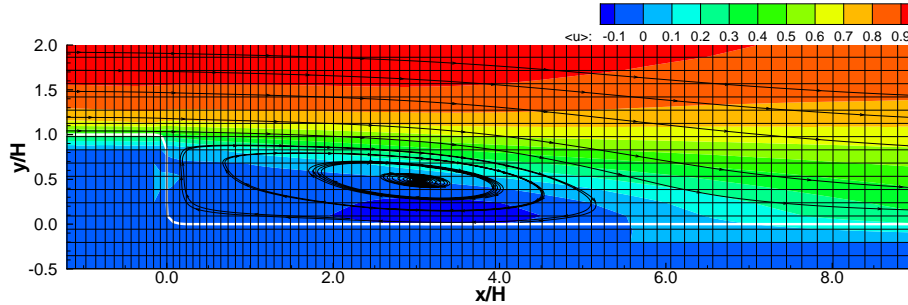
Figure 4.32: Partial computational domain of the backward-facing step using CIIM. Thick lines: immersed interface.

near-wall cells.

From the above analysis, it can be found that the performance of GWFP and WW depends on Reynolds number. Although TBLE performs much better, the flow dynamics in several near-wall cells are also affected by the momentum-mixing procedure, which causes a Reynolds stress oscillation in each case, independent of the particular wall model.

4.2.2 Backward-facing step using CIIM

To test the full approach for a moderately complex geometry the backward-facing step is considered. Compared to the turbulent channel flow additional complications are introduced with respect to wall-modeling formulation and flow dynamics. With respect to the former the wall-normal direction is not continuous and changes abruptly in the corners, which poses a difficulty for the underlying level-set representation of the wall and for defining unambiguous wall-tangential directions. With respect to the latter the challenge lies in the problem of separation process.

In the computation using CIIM the computational domain size is $40h \times 6.5h \times 3h$ in the streamwise, vertical and spanwise directions, respectively. The step is immersed into the computational domain and does not collapse with computational-grid lines, as partially sketched in Fig. 4.32. The resolution is $192 \times 44 \times 24$ which is comparable with the boundary-conforming case using the same grid refinement near the step. The same boundary conditions as in

Table 4.6: Reattachment position and the size of the secondary-separation bubble using CIIM.

case	x_r/H $(c_f = 0)$	x_r/H $(\chi = 0.5)$	$x_{s2}/H \times y_{s2}/H$
IB_GWFP	5.03	5.80	N/A
IB_WW	4.88	5.75	N/A
IB_TBLE	7.0	5.55	N/A

(a) Friction coefficient

(b) Pressure coefficient
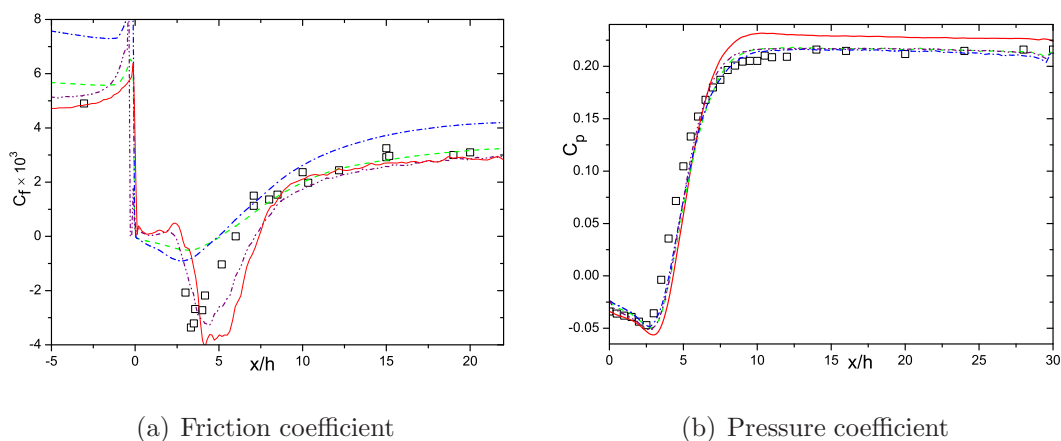
Figure 4.33: Friction- and pressure-coefficient comparisons of experiment and wall models using body-fitted girds and CIIM. Square symbol: EXP [91]; solid line: WM_TBLE; dashed line: IB_GWFP; dashdotted line: IB_WW; dash-dotdotted line: IB_TBLE.

the boundary-conforming case are used, except at the wall, where the wall-shear stresses from the wall-model are imposed by wall-shear force using CIIM. The coupling position is a vertical-cell size away from the wall, corresponding to $y_c^+ = 37$ based on the friction velocity at the inlet. The cases using GWFP, WW and TBLE are denoted as IB_GWFP, IB_WW and IB_TBLE, respectively.

The global flow features of the reattachment length and the secondary-separation bubble of wall-modeling cases indicated by two different criteria are shown in Tab. 4.6. An obvious observation is that the two criteria are no longer equivalent in the cases IB_GWFP and IB_WW unlike for the body-fitted cases. This is caused by two facts. On the one hand, as the coupling position does no longer coincide with the first off-wall grid point, the velocities used in the wall models are interpolated using pseudo-Laplacian weighted interpolation method as detailed in App. A. On the other hand, for the momentum-mixing procedure the criterion

(a) Streamwise mean velocity comparison

(b) Vertical mean velocity comparison
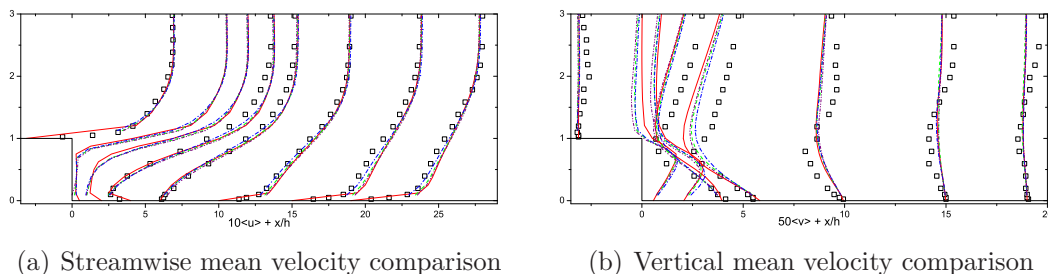
Figure 4.34: Mean velocity comparisons of experiment and wall models using body-fitted girds and CIIM. Lines and symbols labeled as in Fig. 4.33.

based on the percentage of forward-flow time is no longer true at the first off-wall grid points. All the separation lengths indicated by the zero wall friction become smaller than in the body-fitted cases. Another obvious result is that there is no secondary separation bubble for all three cases. It can deduced that the momentum mixing contaminates the near-wall flow dynamics at this relatively low Reynolds number.

The friction and pressure coefficients are defined as in Eq. 4.8, and the same reference values as in experiment are used. The results are compared in Fig. 4.33. Upstream of the step GWFP and WW overpredict the wall friction as in body-fitted cases. And the TBLE also overpredicts the wall friction, unlike wall-friction underprediction for TCF at relatively low Reynolds numbers. The wall pressure is underpredicted at the upper corner of the step using CIIM, which makes the favorable pressure gradient upstream of the step large. Therefore, the TBLE returns the large wall-shear stress. In the separation region GWFP and WW also underpredict the wall-shear stress, while the positive values in the front of the separation is absent due to the CIIM formulation. The C_f of TBLE using CIIM is compared with the result of body-fitted case in Fig. 4.33(a). The former C_f is smaller than the latter in the separated and recovery regions due to the lower adverse pressure gradient shown in Fig. 4.33(b). In the recovery region, the overprediction of wall friction uisng WW and GWFP becomes smaller compared with that in the body-fitted cases, as indicated in Fig. 4.24. This is similar as TCF at low Reynolds numbers using CIIM and caused by the artificial momentum mixing. The pressure-coefficient comparisons in Fig. 4.33(b) show that all cases using CIIM have a better predicted pressure at recovery region than

(a) Streamwise Reynolds normal stress

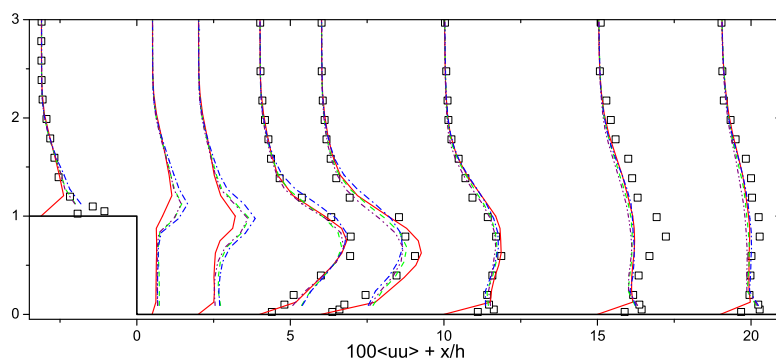(b) Vertical Reynolds normal stress
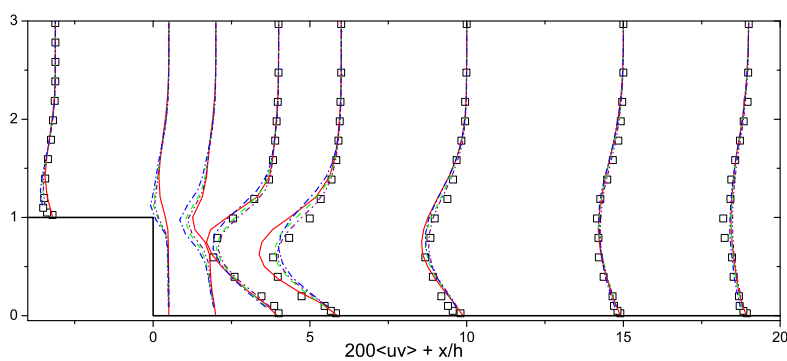
(c) Reynolds shear stress

Figure 4.35: Reynolds stress comparison of experiment and wall models using body-fitted girds and CIIM. Lines and symbols labeled as in Fig. 4.33.
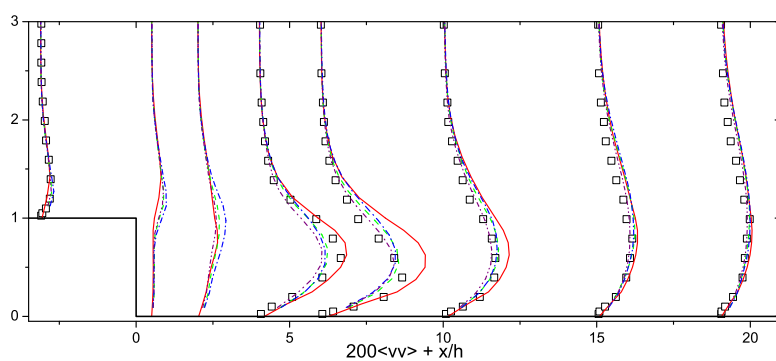
WM_TBLE using body-fitted grids. This is attributed to the favorable effect of artificial momentum mixing near the wall, which makes the near-wall velocity larger, therefore resulting in smaller pressure.

From a comparison of the mean velocity in Fig. 4.34 it can be seen that wall models in the framework of CIIM perform as well as using the body-conforming formulation. The transverse Reynolds normal stress and Reynolds shear stress are in better agreement with the experiment than those of WM_TBLE, as shown in Fig. 4.35. This can be attributed to the favorable effect of artificial momentum mixing near the wall, which is consistent with the more accurately predicted pressure coefficient. The chosen position of immersed interface leads to the situation that momentum mixing is applied all along the lower wall downstream of the step. This artificial mixing is corresponding to high turbulence mixing, which results in large turbulent length scale there. Therefore, the better results are obtained.

4.2.3 Conclusions of wall models using CIIM

From the above investigation, it can be found that the momentum mixing procedure in CIIM has some disadvantages and advantages. In the TCF simulation, it results in a Reynolds-number dependence of the model performance, except for the TBLE model. The near-wall flow dynamics are contaminated that the fluctuation of resolved Reynolds stress is detected in several near-wall cells for TCF, and the secondary-separation bubble disappears in backward-facing step case. This artificial mixing enhances the turbulence mixing in the recovery region, which exhibits its favorable effect on better predicted recovery pressure and Reynolds stresses. Improved mean velocity and Reynolds stress are obtained using wall models in the framework of CIIM.

The conclusions of wall modeling on body-fitted grids still apply, namely that the TBLE is superior to GWFP and WW in TCF simulation. However, in the more complex flow along backward-facing step, the three wall models show almost the same results with respect to mean-flow quantities.

Chapter 5

Applications

In this chapter, wall models are applied to three cases with separation from smooth continuous surfaces at high Reynolds numbers, in order to obtain a more profound understanding of the characteristics of the wall modeling.

The cases include flow over two different hills in channels, as shown in Fig. 5.1, both with separation from smooth surfaces. They serve to assess whether the wall models for ILES in the framework of CIIM are able to predict such kind of separation. These flows produce complex flow behavior associated with acceleration, separation, reattachment and recovery, which are very difficult for most of the statistical turbulence models to predict correctly, even with respect to global flow features. These two cases have different boundary conditions and much different pressure gradients on the hills. Therefore, the flows behave much differently. The separation is very shallow in the bump case, whereas it is large in the periodic hill case. The flow is quasi-steady in the former, but highly unsteady in the latter. There is a long recovery region in the former, while there is only a short recovery region in the latter.

The third case is the flow over a smooth circular cylinder at very high Reynolds number $Re_D = 1.0 \times 10^6$, based on the diameter of the circular cylinder. The AMR technique is used in combination with wall modeling. The aim is to show the potential of wall modeling to treat complex flows, and show its potential as practical method to treat complex geometries in practical engineering. In the following sections, these cases are presented in detail.
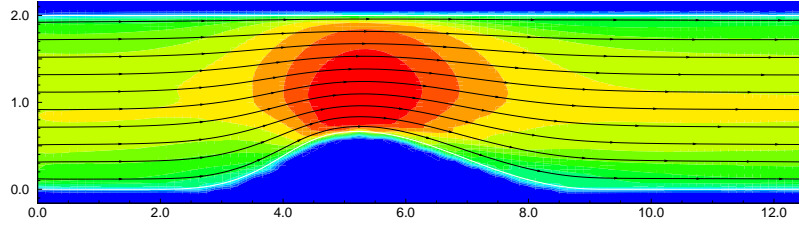
(a) Configuration of bump
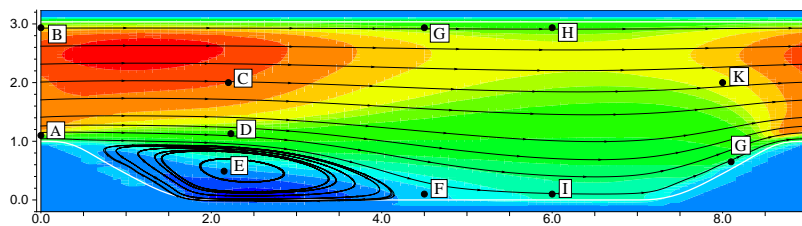
(b) Configuration of periodic hill

Figure 5.1: Configurations of bump and periodic hill. White line: immersed interfaces.

5.1 Flow over a bump

5.1.1 Case description

This case originally has been designed to investigate the boundary layer under the effect of a variable pressure gradient by an experiment, which mimics the adverse pressure gradient on the suction side of an airfoil at the verge of separation at very high Reynolds number [14, 167]. To investigate the flow structures in much more detail DNS of this configuration has been carried out first at $Re_\tau = 395$ [117], and then at $Re_\tau = 600$ [107], where $Re_\tau = u_\tau h/\nu$ is the friction Reynolds number based on the friction velocity u_τ at the inlet, half channel height h, and the kinematic viscosity ν. A shallow separation region was observed in both investigations. Reynolds stresses and flow structures were studied in detail. Several SGS models were assessed on different resolutions in comparison with DNS. The case at $Re_\tau = 600$ is chosen as a reference because of its higher Reynolds number $Re_h = u_{bulk}h/\nu = 12,600$, where u_{bulk} is the bulk velocity at the inlet. At this Reynolds number, the flow exhibits a slight deceleration, strong
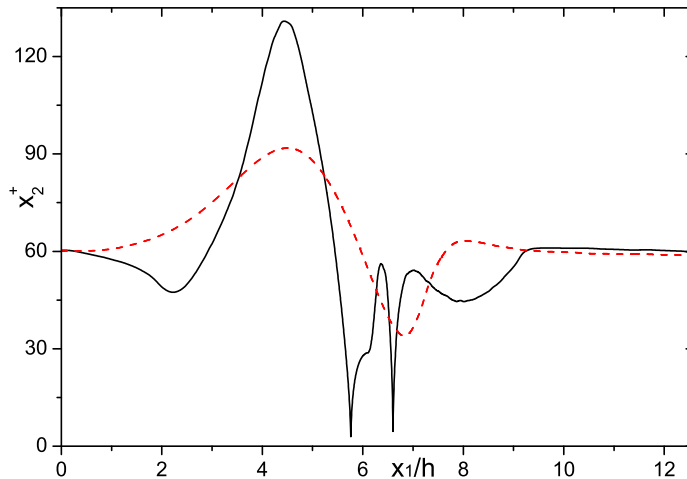
Figure 5.2: Nondimensional wall distance of interpolation points on coarse resolutions of bump on both walls. Solid line: lower wall; dashed line: upper wall.

acceleration, very shallow separation (no separation in the experiment at very high Reynolds number), reattachment on the leeward side of the hill and a long recovery region, due to the complex pressure gradient.

The computational domain is $4\pi h \times 2.5h \times \pi h$ in streamwise, vertical and spanwise directions, with the bump symmetrically immersed, in the lateral direction. Two different grids are used to assess the issues of resolution. The coarse one is $96 \times 48 \times 24$, and the fine one is $192 \times 64 \times 48$. The grids are equally distributed in all three directions. The recycling inflow technique and the outflow boundary condition as described in section 2.4.1 are applied in the streamwise direction. Periodic conditions are applied in the spanwise direction. Wall models are adopted at the immersed interfaces. For the coarse resolution the cases using GWFP, WW and TBLE are denoted as $BGWFP\_C$, BWW_C and $BTBLE\_C$, respectively. For the finer resolution, the last character C is replaced by F, which means the fine resolution.

The CFL number is 0.5 for the coarse resolution and is halved on the fine one. The statistics are accumulated for around 15 flow-through times on the coarse resolution and for around 10 flow-through times on the fine one, because the flow is quasi-steady. The nondimensional wall distance (based on the friction velocity from DNS) of the coupling position of both immersed interfaces are shown in Fig.

(a) Friction coefficient on the bump

(b) Friction coefficient on the upper wall
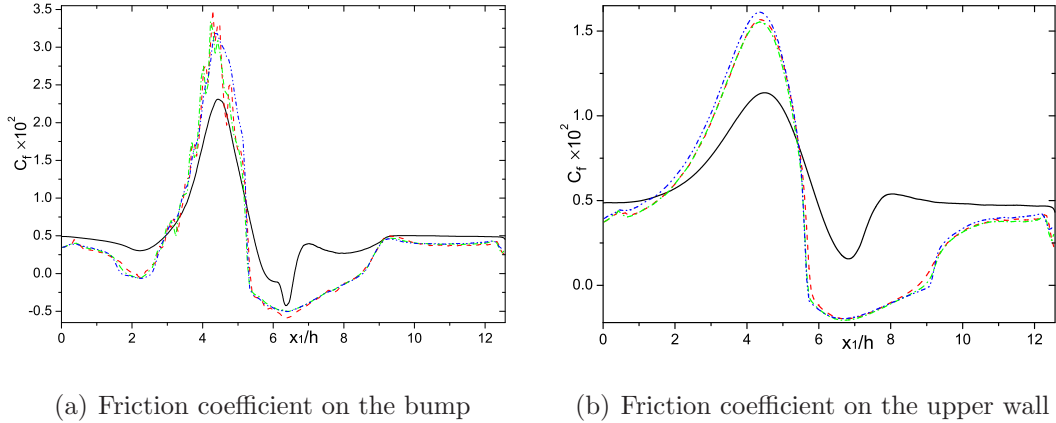
Figure 5.3: Friction-coefficient comparisons of three interpolation methods using TBLE and DNS [107]. Solid line: DNS; dashed line: linear least square; dashdotted: trilinear; dashdotdotted line: pseudo-Laplacian weighted method.

5.2 for the coarse resolution. In most of the attached flow region, the interpolation points are outside of the wall layer.

5.1.2 Results of bump case

In this section, first, three interpolation methods, as shown in App. A, are compared for a complex geometry and variable pressure gradient. Subsequently the results of coarse and fine resolutions are presented. Last, the wall-shear stress of DNS are used to formulate the approximate boundary condition for exterior LES and its results are compared with those of TBLE. The gross-flow parameters are compared with those of DNS [107]. Mean velocities and Reynolds stresses are also compared at several sections. For the sake of simplicity and brevity, only the turbulent kinetic energy and Reynolds shear stress are shown and analyzed in detail.

5.1.2.1 Comparison of interpolation methods

Since there is no exact instantaneous flow data, the interpolation methods are compared indirectly using the mean-friction coefficient returned by a wall model. The friction coefficient is nondimensionalized by the mean bulk velocity. The

(a) Friction coefficient on the bump

(b) Friction coefficient on the upper wall
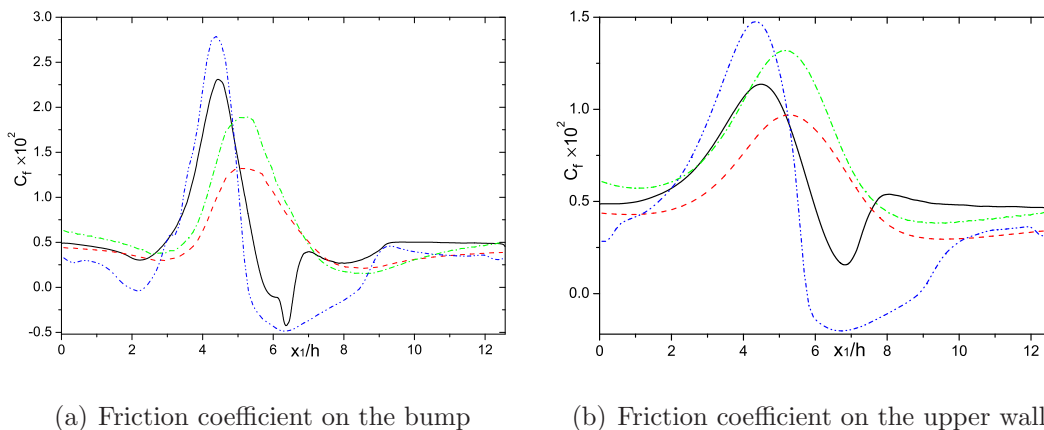
Figure 5.4: Friction-coefficient comparisons of three wall models using coarse resolution with DNS [107]. Solid line: DNS; dashed line: $BGWFP\_C$; dashdotted: BWW_C; dashdotdotted line: $BTBLE\_C$.

interpolated results of velocity are always smooth, and the effect of pressure gradient is small in GWFP, while it is absent in WW. Therefore, the TBLE is used on the fine grid resolution and its results are compared in Fig. 5.3.

The friction coefficients of the linear least square and the trilinear interpolation methods are not smooth on the bump, as shown in Fig. 5.3(a). Whereas on the straight part of the lower immersed interface, three interpolation methods perform almost the same, and the results are smooth as on the upper immersed interface in Fig. 5.3(b). This difference is caused by the pressure gradient interpolation of three methods in the presence of the curved immersed interface. Globally, the interpolation method based on the pseudo-Laplacian weight is superior to the other two. Hence, it is used in the following.

5.1.2.2 Results for bump on coarse-resolution grid

The friction coefficients are compared in Fig. 5.4. Upstream of the bump GWFP predicts wall-shear stress well while WW overpredicts the data as shown in Fig. 5.4(a), which resembles that in TCF cases and in the backward-facing step case. TBLE produces underpredicted values due to the adverse pressure gradient shown in Fig. 5.5(a). GWFP and WW heavily underpredict the wall friction on the windward side and the rear part of the leeward side of the bump, but they over-

(a) Pressure coefficient on the bump   (b) Pressure coefficient on the upper wall
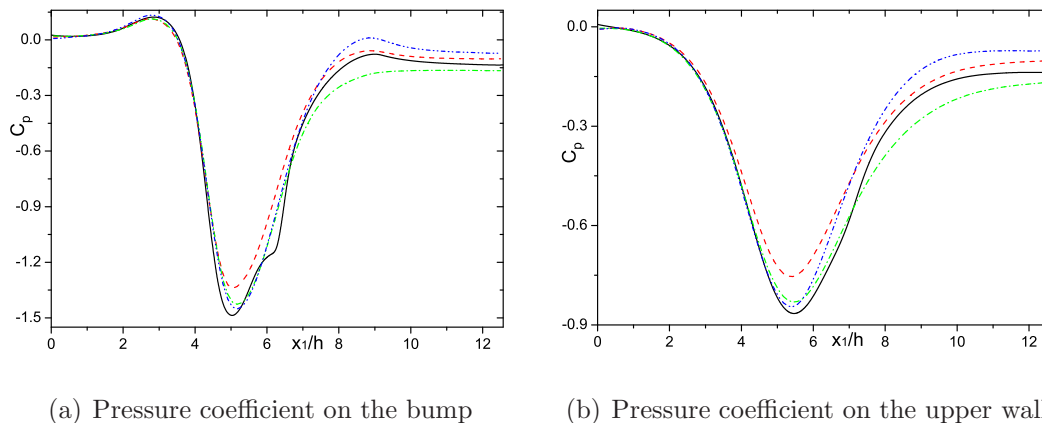
Figure 5.5:   Pressure-coefficient comparisons of three wall models using coarse resolution with DNS [107]. Lines labeled as in Fig. 5.4.

predict data on the forward part of the leeward side. The position of maximum wall friction is wrongly predicted by GWFP and WW. It is found on the top of the bump, but not before the top as in DNS. The TBLE shows overpredicted data under a strong favorable pressure gradient, and underpredicted data under a strong adverse pressure gradient. However, it predicts the position of the maximum wall-shear stress well. In the straight recovery region all models underpredict the wall-shear stress. On the upper straight wall, the performance of the three wall models are clearly shown in Fig. 5.4(b). Their characteristics resemble those on the lower immersed interface.

Above results show that GWFP and WW mainly depend on the velocity and miss the correct position of maximum wall-shear stress on both immersed interfaces. The TBLE model can predict the global tendency of wall-shear stress well, $e.g.$ the position of maximum values. However, the simplified TBLE without convective terms are strongly affected by the pressure-gradient term, which causes the wall-shear stress to be underpredicted under an adverse pressure gradient, but overpredicted under a favorable one, except in the far recovery region after $x_1/h = 9.0$, in agreement with the findings for the backward-facing step of the last chapter.

Although the TBLE predicts negative wall-shear stress in the regions $2.02 \leq x_1/h \leq 2.29$ and $5.30 \leq x_1/h \leq 8.44$ on the lower wall, and $5.83 \leq x_1/h \leq 8.84$

on the upper wall, which is $5.76 \leq x_1/h \leq 6.60$ on the lower wall in DNS, these negative wall-shear stresses could not drive the flow back in the exterior LES for the case $BTBLE\_C$ on coarse resolution. That is because the resolution is so coarse that the grid width is larger than the height of separation.

The pressure coefficients are compared in Fig. 5.5. Upstream of the top of the bump all cases produce almost the same and well predicted pressure coefficients, except near the top of the bump. The minimum of the pressure is not predicted well by GWFP, while WW and TBLE behave well until the reattachment point $x_1/h = 6.6$ indicated by the results of DNS. On the leeward side GWFP over-predicts the pressure. In the recovery region on the bump, GWFP and TBLE can reproduce the correct tendency. However, WW cannot reflect the influence of the concave region at the foot of the bump. In the straight recovery region GWFP returns better pressure data, while it is lower in BWW_C and is higher in $BTBLE\_C$. On the upper immersed interface, the general behavior of wall models resembles that on the lower bump.

The mean velocity and Reynolds stresses are interpolated from the Cartesian grids to the wall-normal direction by a second-order Lagrange interpolation method. The mean velocity and Reynolds stress in the local coordinates are obtained by vector projection and tensor transformation respectively, for comparison with DNS results. The mean velocity profiles are compared in Fig. 5.6(a).

Before the reattachment point the three wall models behave almost the same, and the mean-velocity profiles are predicted reasonably well compared with DNS, before the top of the bump. On the leeward side of bump, neither wall model can reproduce the mean-velocity profiles well. In the recovery region, the mean velocities are well predicted by GWFP, which is consistent with its better recovery pressure. While in BWW_C using WW, the mean velocities are underpredicted near the wall but are overpredicted near the channel center. They are under-predicted in the upper part of the channel in $BTBLE\_C$, but are overpredicted near the lower immersed interface. It has to be mentioned that the mean-velocity profiles are not smooth in the lower part of the channel before the beginning of the bump, which is caused by the too short distance from the inlet to the recycling plane. The distance is not long enough for the flow to develop. The original recycling plane does not totally decorrelate with the inlet plane, therefore, some
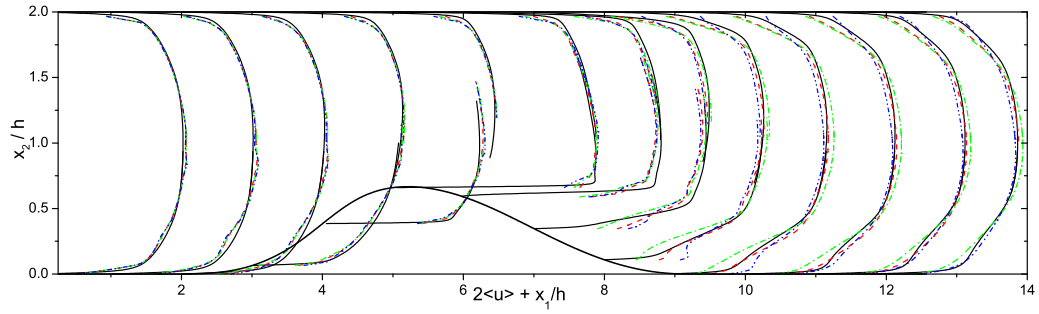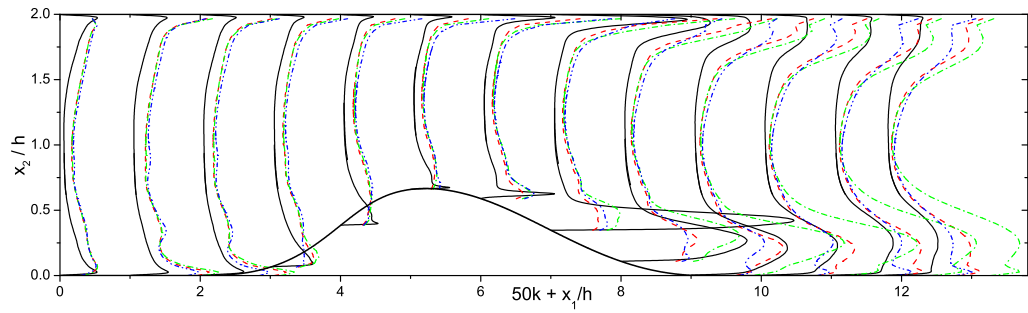
(a) Mean velocity

(b) Turbulent kinetic energy
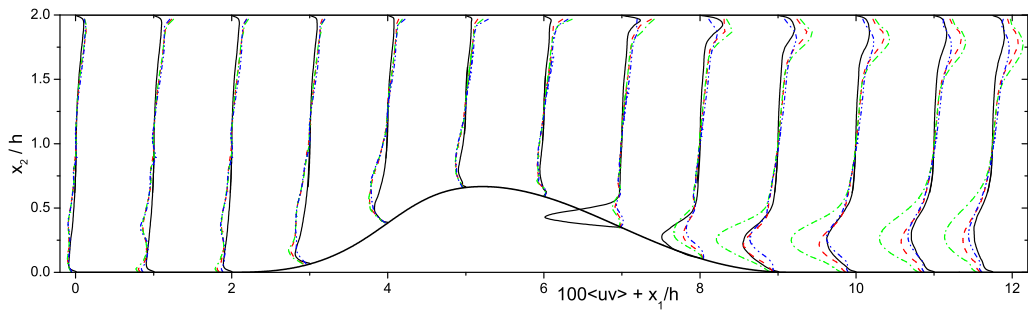
(c) Reynolds shear stress

Figure 5.6:   Mean velocity, turbulent kinetic energy and Reynolds shear stress comparisons of three wall models using coarse resolution with DNS of bump at $Re_h = 12,600$.   Solid line: DNS; dashed line: $BGWFP\_C$; dashdotted: BWW_C; dashdotdotted line: $BTBLE\_C$.

artificial structures develop.

The turbulent kinetic energy and Reynolds shear stress are compared in Fig. 5.6(b) and Fig. 5.6(c), respectively. All the wall models give almost the same overpredicted turbulent kinetic energy and Reynolds shear stress before the top of the bump. On the leeward side of the bump, before $x_1/h = 8.0$, the turbulent kinetic energy and Reynolds shear stress is underpredicted near the lower wall, especially in the separation region, whereas it is overpredicted away from the lower wall. In the plane-channel recovery region, turbulent kinetic energy is overpredicted on the upper wall for all cases, but is reasonable on the lower wall for cases $BGWFP\_C$ and $BTBLE\_C$. It is overpredicted across the channel in BWW_C. The behavior of the Reynolds shear stress is like that of the turbulent kinetic energy, and is consistent with the mean-velocity profiles.

From the above analyses it can be concluded that the flows are more sensitive to wall modeling in the recovery region than in the attached or separated region. TBLE can produce better results than the WW concerning the gross-flow parameters, mean velocity and Reynolds stresses. GWFP is better than TBLE concerning the mean velocity profile, but it is worse than TBLE with respect to the Reynolds stresses in the straight recovery region. The influence of the recycling-inflow length needs further investigation. Since the turbulent kinetic energy and Reynolds shear stress are much overpredicted, the resolution is not high enough to represent the exterior flow using LES. In the next section the results of a fine resolution is presented.

5.1.2.3 Results for bump on fine-resolution grid

The grid points are doubled in streamwise and spanwise directions. In vertical direction, the number of grid point is increased to obtain a coupling position $x_2^+ = 45$ at the inlet, based on the friction velocity of DNS.

The friction coefficients are compared in Fig. 5.7. The tendency of wall friction for each wall model is almost the same as using coarse resolution, while the wall friction increases at both immersed interfaces. The pressure coefficients are compared in Fig. 5.8. Before the top of the bump the pressure is predicted well compared with that of DNS, and there is almost no change compared to that
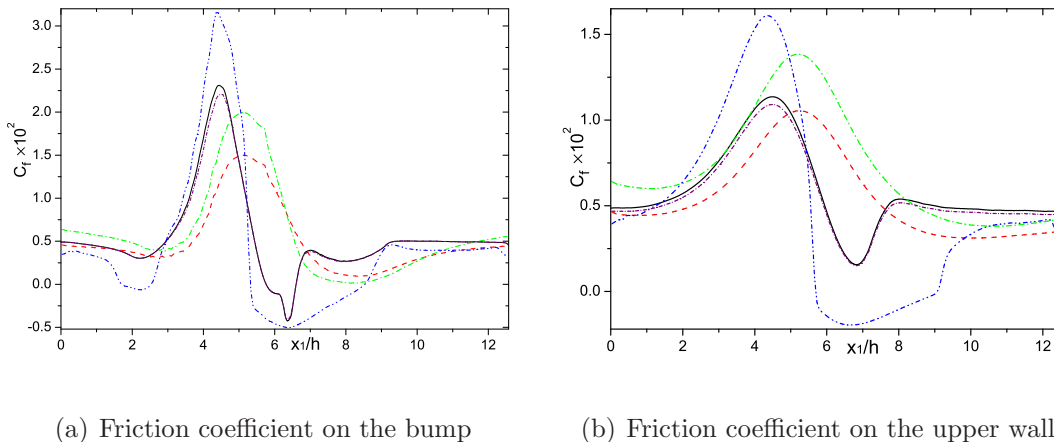
(a) Friction coefficient on the bump (b) Friction coefficient on the upper wall

Figure 5.7: Friction-coefficient comparisons of four wall models using fine resolution with DNS [107]. Solid line: DNS; dashed line: $BGWFP\_F$; dashdotted: BWW_F; dashdotdotted line: $BTBLE\_F$; shortdashdotted: $BDNS\_F$.

of using coarse resolution. The minimum pressure is improved using TBLE and WW and is slightly overpredicted using TBLE. There is no improvement using GWFP. A large difference is observed in the recovery region when using GWFP and WW. GWFP tends to produce a separation, and WW produces a separation, although the wall friction using both wall models are all positive. Therefore, the pressure is underpredicted at the concave leeward side. The pressure on the upper wall behaves like that on the lower wall.

The mean velocities, turbulent kinetic energy and Reynolds shear stress are shown in the Fig. 5.9. The mean velocity before the top of the bump almost does not change, and the artificial influence of the short recycling length cannot be eliminated by fine resolution. On the leeward-side and the straight recovery regions the results of TBLE are improved. However, the mean velocities of GWFP and WW become worse compared to those for the coarse resolution, because they cannot represent the influence of the concavity at the foot of leeward side. Although there is a separation bubble using WW on the fine resolution, WW gives a positive wall friction along the entire bump, as the coupling point is outside of the backflow region.

The turbulent kinetic energy and Reynolds shear stress become smaller than that of the coarse resolution, especially near the channel center. In the recovery

(a) Pressure coefficient on the bump   (b) Pressure coefficient on the upper wall
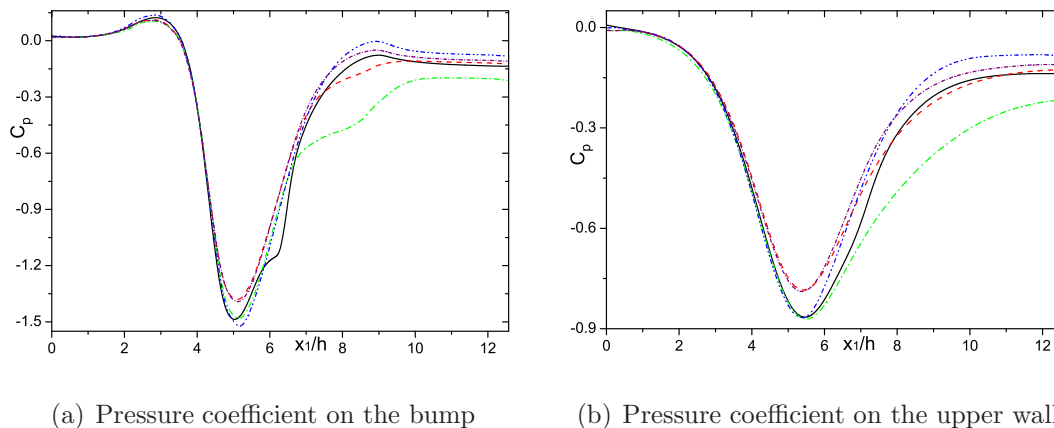
Figure 5.8: Pressure-coefficient comparisons of four wall models using coarse resolution with DNS [107]. Lines labeled as in Fig. 5.7.

region, the results of TBLE are improved, while even higher values are returned by GWFP and WW, because they tend to produce a separation region at the concavity of the foot of leeward side.

From above analysis it can be seen that if wall models cannot reflect the wall curvature and the pressure gradient well, even when the grid resolution is increased, the flow prediction cannot be improved. In this context, TBLE is better than GWFP and WW concerning the global flow variables, mean velocity and Reynolds stresses. This reflects the importance of the modeling of near-wall flow dynamics.

5.1.2.4 Wall modeling using wall-shear stress from DNS

To gain understanding about the influence of modeled wall-shear stress, the mean streamwise wall-tangential shear stress from DNS [107] is used to formulate a wall model. In order to take the fluctuations of the wall stress into account, the formulation of Schumann, *e.g.* Eqs. 1.5, is used as described in chapter 1. The wall-tangential velocities $u_i(i = 1, 3)$ are interpolated from exterior LES at the coupling positions. A time average is used to obtain the mean velocity at the coupling positions. The grid resolution corresponds to the fine one, and other computational conditions are the same as those for the fine resolution in the last
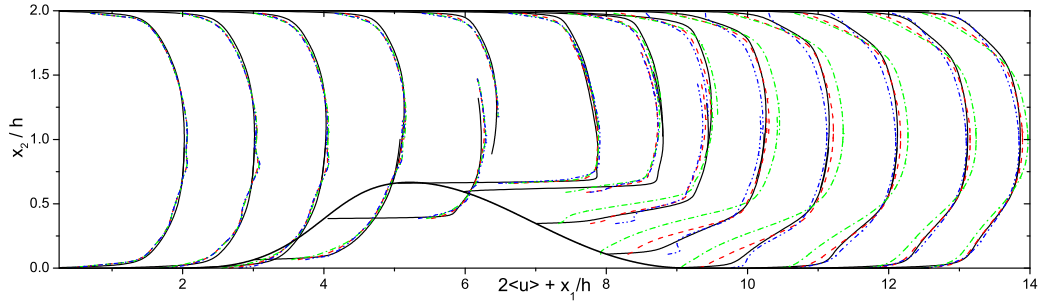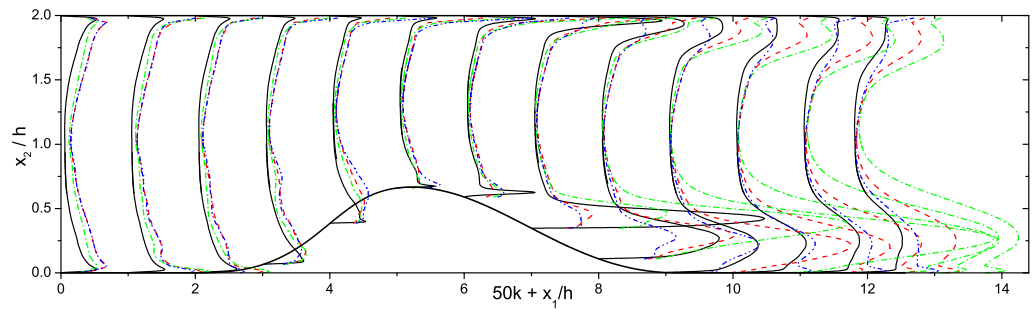
(a) Mean velocity

(b) Turbulent kinetic energy

(c) Reynolds shear stress

Figure 5.9: Mean velocity, turbulent kinetic energy and Reynolds shear stress comparisons of three wall model and DNS of bump at $Re_h = 12,600$. Solid line: DNS; dashed line: $BGWFP\_F$; dashdotted line: BWW_F; dashdotdotted line: $BTBLE\_F$.

subsection. This case is denoted as $BDNS\_F$.

The wall friction at both immersed interfaces is also shown in Fig. 5.7. Compared with the results of DNS, the wall friction on the lower wall has smaller values near and before the position of maximum wall friction, and it is slightly underpredicted on the upper immersed interface. The pressure coefficient is also compared with other results in Fig. 5.8. It can be seen that at concave region of the windward side the pressure is not well recovered. Near the top of the bump, it is underpredicted as GWFP using the same resolution. In the recovery region, the benefit is obvious, the tendency resembles that of DNS, and is better than the results of TBLE.

The mean velocity profiles, turbulent kinetic energy and Reynolds shear stress are compared with those of case $BTBLE\_F$ in Fig. 5.10. The mean velocity profiles are as good as in case $BTBLE\_F$, except for the last four positions on the upper immersed interface. The resolved turbulent kinetic energy is larger than that in $BTBLE\_F$, especially in the recovery region, but the results are better than that of $BGWFP\_F$ and BWW_F using the same resolution. The Reynolds shear stresses are larger than that of TBLE in the straight recovery region, which is consistent with its higher turbulent kinetic energy. These results are not as good as expected using the better modeled wall-shear stress. Even the results of TBLE is better than using the wall-shear stress directly from DNS.

What we learn from the above analysis is that the recovery pressure can be reproduced better when a correct wall-shear stress is used. The mean velocity is not very sensitive to the modeled wall-shear stress. Even though a much more accurate wall shear-stress is provided as an approximate boundary condition for the exterior LES, the results of Reynolds stresses are not better than that of TBLE. Considering the difference between $BTBLE\_F$ and $BDNS\_F$, the TBLE can take the fluctuations of the velocity and the pressure into account, while the formulation of Schumann [154] can only take the fluctuations of the velocity into account. In this flow, the Reynolds shear stress in the streamwise wall-tangential direction is responsible for most of the turbulence production. The pressure fluctuation is very important for the turbulence redistribution from the streamwise Reynolds normal stress to other two normal components. Therefore, it can be suspected that the time fluctuation of the wall-shear stress introduced
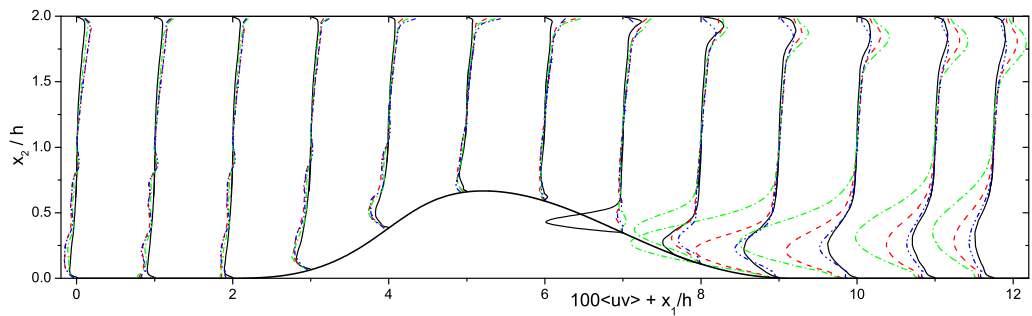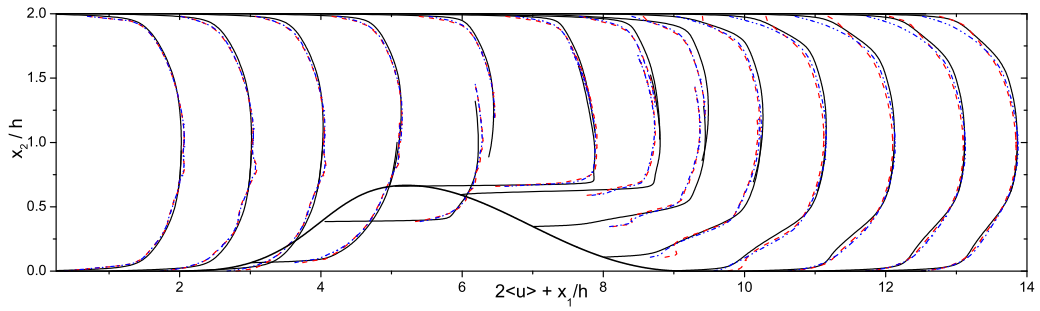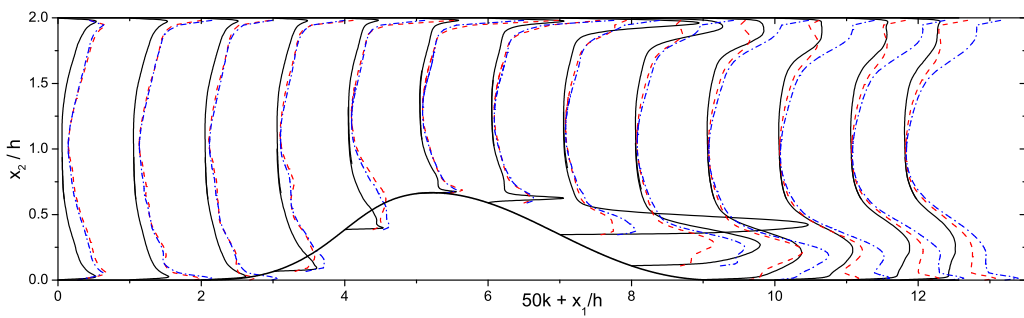
(a) Mean velocity

(b) Turbulent kinetic energy
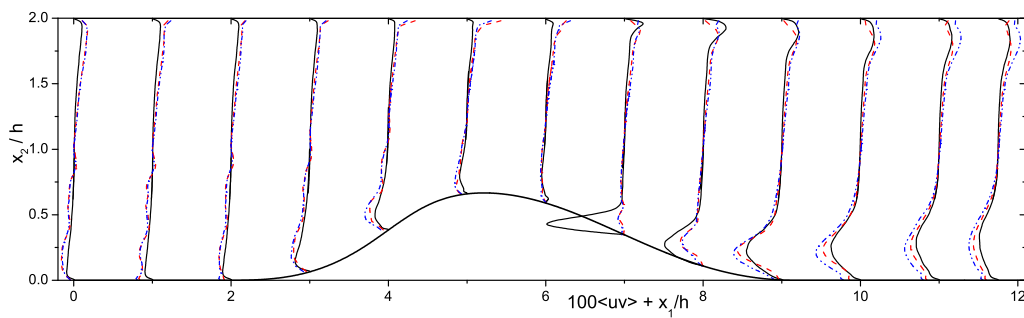
(c) Reynolds shear stress

Figure 5.10: Mean velocity, turbulent kinetic energy and Reynolds shear stress comparisons of $BTBLE\_F$, $BDNS\_F$ and DNS of bump at $Re_h = 12,600$. Solid line: DNS; dashed line: $BTBLE\_F$; dashdotted line: $BDNS\_F$.

112

by the pressure fluctuation is very important to the exterior LES.

5.1.3 Conclusions for the bump case

From the above investigations the following can be concluded. First, the flow is much more sensitive to the wall modeling in the recovery region than in the attached flow or separation regions, which differs from the results of the backward-facing step having fixed separation introduced by the sharp corner of the wall at relatively low Reynolds number, see section 4.2.2 of the last chapter. Second, in order to obtain well resolved exterior LES, the resolution should be sufficient. Third, if a wall model cannot model the near-wall flow dynamics well, the resolved part of the flow will become even worse with increasing resolution. Fourth, not only the correct values of wall-shear stress is important, but the fluctuation of the modeled wall-shear stress is also very important, concerning its influence on the resolved Reynolds stresses of the exterior LES, especially in the recovery region. Finally, the influence of the recycling length needs further investigation.

5.2 Flow over a periodic hill

5.2.1 Case description and computational setup

In order to avoid the influence of the inflow/outflow boundary conditions as in bump case, a flow over periodic hills is chosen as an application, which has periodic boundary condition in the streamwise direction.

The flow over periodic hills in a channel as proposed by Mellen *et al.* for numerical simulation [120] is modified from an experiment of Ahmeida *et al.* [4], with doubled distance between two hills in the streamwise direction allowing for natural reattachment, halved channel height to reduce the computational effort, instead of sidewalls with periodicity in the spanwise direction and reduced Reynolds number based on the hill height. This well defined test case has been used as a benchmark test in several workshops, *e.g.* the EROFTAC/IAHR workshops on refined turbulence modeling [83, 115] and large eddy simulation of complex flows focusing on the SGS-model developments and wall modeling. In

this case, the turbulence evolution associated with separation from the smooth curved surface, recirculation, reattachment on the flat plate, acceleration and wall proximity on the windward of the hill. Most of the statistical turbulence models fail to predict these flow features, or even gross flow features such as separation length. A simulation with highly resolved LES on the hill side and wall modeling on the straight side was carried out by Fröhlich *et al.* [52], investigating the physical issues comprehensively at $Re_H = 10,595$ based on the hill height H, bulk velocity and kinematic viscosity. It is interesting that a phenomenon, associated with the 'splatting' of large scale eddies originating from the shear layer and convected downstream to the windward slope, explains why RANS simulations, even when applying second-moment closures, cannot capture the flow field accurately. The Reynolds-number effects on the flow features were investigated in detail by experiments, DNS and highly resolved LES on both walls, in a wide range of Reynolds numbers covering $100 \le Re_H \le 10,595$ [21].

Wall modeling issues were extensively investigated combining different SGS models with different wall models on coarse body-fitted grids [120, 170, 171], which highlighted the importance of an adequate streamwise resolution of the flow in the vicinity of the separation line. The near-wall treatment was found to be more influential than the SGS modeling on the quality of the results obtained on coarse grids. It has to be mentioned that a new wall modeling strategy for separated flows has been developed using statistical evaluations of wall-resolved LES data, which takes the effect of streamwise pressure gradient into account [20].

Hybrid LES/RANS approaches, including detached-eddy simulation, were evaluated for this test case [17, 18, 53, 178]. A massive deterioration of the results was detected when the LES/RANS interface lies outside of the boundary layer on the crest of the hill [178].

In the computation the simulation domain is $9.0H \times 3.335H \times 4.5H$ with the configuration symmetrically immersed, in the lateral direction, as shown in Fig. 5.1(b). Periodic conditions are used in the streamwise and spanwise directions, and the wall models are adopted on the immersed interfaces as in the bump case. To assess the wall models a relatively coarse resolution is used at Reynolds number $Re_H = 10,595$. Beside the coarse resolution a finer resolution is used at higher

114

Table 5.1: Simulation parameters of the periodic hill

$Case$	Re_H	$N_{x_1} \times N_{x_2} \times N_{x_3}$	CFL	T_{avg}	x_{sep}/H	x_{reatt}/H
$HGWFP\_C$	10,595	$96 \times 64 \times 32$	0.25	40	0.45	4.31
HWW_C	10,595	$96 \times 64 \times 32$	0.25	40	0.38	4.44
$HTBLE\_C$	10,595	$96 \times 64 \times 32$	0.25	40	0.65	4.00
$HHTBLE\_C$	37,000	$96 \times 64 \times 32$	0.5	90	0.75	3.41
$HHTBLE\_F$	37,000	$192 \times 72 \times 48$	0.5	40	0.75	3.80

Reynolds numbers $Re_H = 37,000$ based on the experiences on the bump. All the simulation cases are listed in the Tab. 5.1, which includes the grid resolution, CFL number, and the flow-through times used to accumulate the statistics.

The separation and reattachment points indicated by the streamline normal to the wall are also shown in Tab. 5.1. On the non-body-fitted coarse Cartesian meshes, it is not reasonable to deduce the separation and reattachment positions. The estimating given here are just for giving an overview and for completeness.

5.2.2 Results for the periodic hill at $Re_H = 10,595$

5.2.2.1 Mean flow quantities

First, three wall models are assessed on the coarse resolution at Reynolds number $Re_H = 10,595$, which are denoted as $HGWFP\_C$, HWW_C and $HTBLE\_C$, respectively. The nondimensional wall distance (based on the friction velocity from resolved LES of Fröhlich [52]) of the coupling position is about 30 on average, with a maximum of 135.8 at $x_1/H = 8.66$, as shown in Fig. 5.11.

The friction coefficient on the lower wall and pressure coefficient on both walls are compared with those of Fröhlich [52] in Fig. 5.12. As in the bump case, the TBLE produces a reasonable tendency of the friction coefficient, but predicts lower values under an adverse pressure gradient, which is another indication for the lack of convective effects in the simplified TBLE model. GWFP and WW produce a wrong tendency and data, except for the short recovery region. It has to be mentioned that the behavior of GWFP and WW are not as in the backward-facing step and bump cases. GWFP predicts a higher wall friction than WW in this case. This may be caused by the strong unsteady flow. However, neither of them can reflect the effect of the pressure gradient.
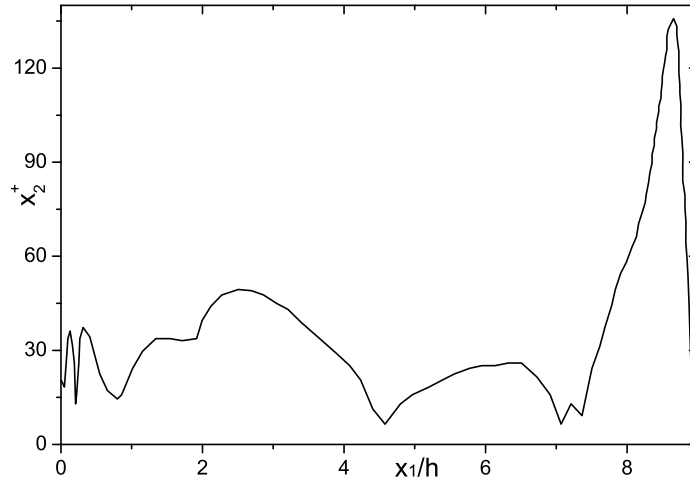
Figure 5.11: Nondimensional wall distances of interpolation points on coarse resolution of the hill at $Re_H = 10,595$.

From the comparison of pressure coefficients in Fig. 5.12(b), the pressure is underpredicted using GWFP and WW on both walls, while the result using TBLE is globally better. On the lower wall, the pressure gradient indicates that the flow recovers more quickly in the wall-modeling LES than in the resolved LES, and the maximum pressure is slightly overpredicted using TBLE. Note that the low pressure region on the top of the hill is accompanied by a short closed separation region, which can be observed in imbedded TBLE, but cannot be observed in the exterior LES due to the coarse grid resolution. This low pressure region on the top of the hill does not appear in the cases $HGWFP\_C$ and HWW_C, for GWFP and WW models cannot represent the influence of the pressure gradient.

The mean velocity, turbulent kinetic energy and Reynolds stresses are compared with the results of highly resolved LES of Rapp [145] using LESOCC at ten sections in Fig. 5.13. The mean velocities are overpredicted in the upper part of the channel, while they are underpredicted near the lower wall in $HGWFP\_C$ and HWW_C, which resembles that in bump case using WW model. In $HTBLE\_C$, the mean velocities are predicted well, but are underpredicted after location $x_1/H = 4.0$ near the upper wall. GWFP predicts better results at these sections. The difference of vertical mean velocities is smaller than streamwise mean

116

(a) Friction coefficient on the hill.

(b) Pressure coefficient on both walls. The shallow ones are on upper wall.
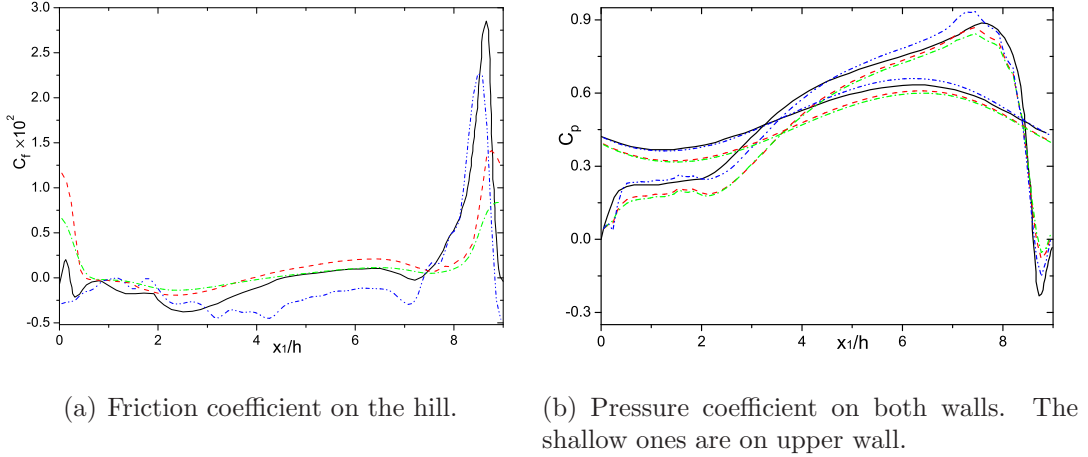
Figure 5.12: Comparisons of friction and pressure coefficients for periodic hill at $Re_H = 10,595$ on coarse resolution. Solid line: Fröhlich [52]; dashed line: $HGWFP\_C$; dashdotted line: HWW_C; dashdotdotted line: $HTBLE\_C$.

(a) Mean streamwise velocity

(b) Mean vertical velocity

(c) Streamwise Reynolds normal stress

(d) Vertical Reynolds normal stress

(e) Turbulent kinetic energy

(f) Reynolds shear stress
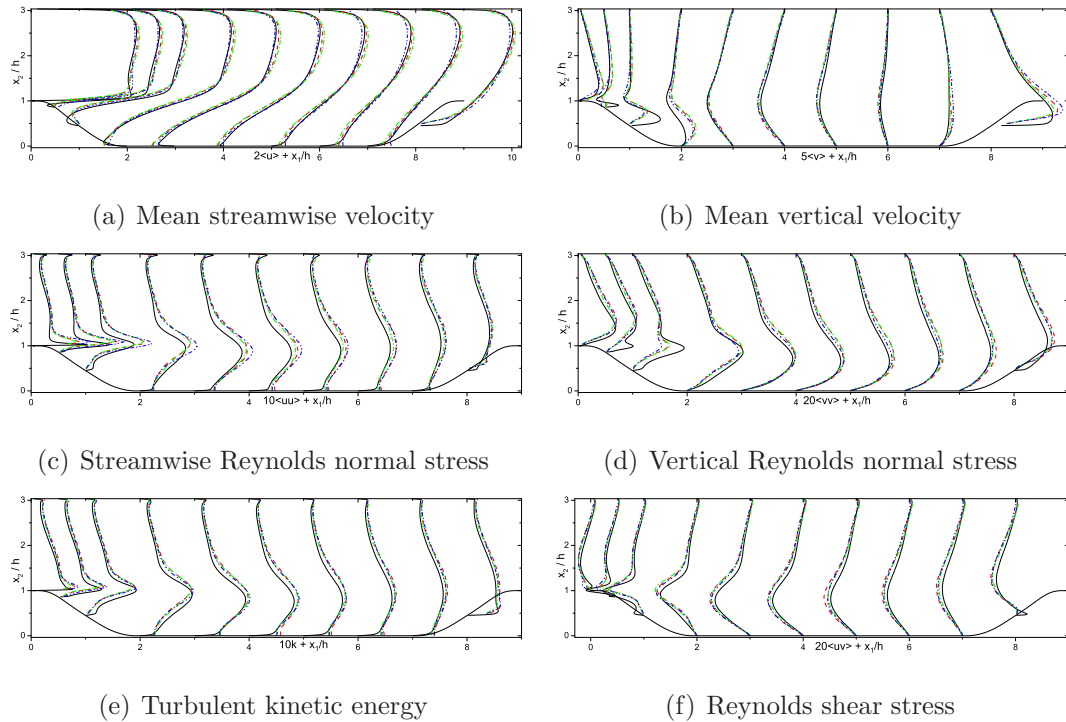
Figure 5.13: Comparisons of mean velocities and Reynolds stresses for periodic hill at $Re_H = 10,595$ on coarse resolution. Solid line: Rapp [145]; other lines labeled as in Fig. 5.12.
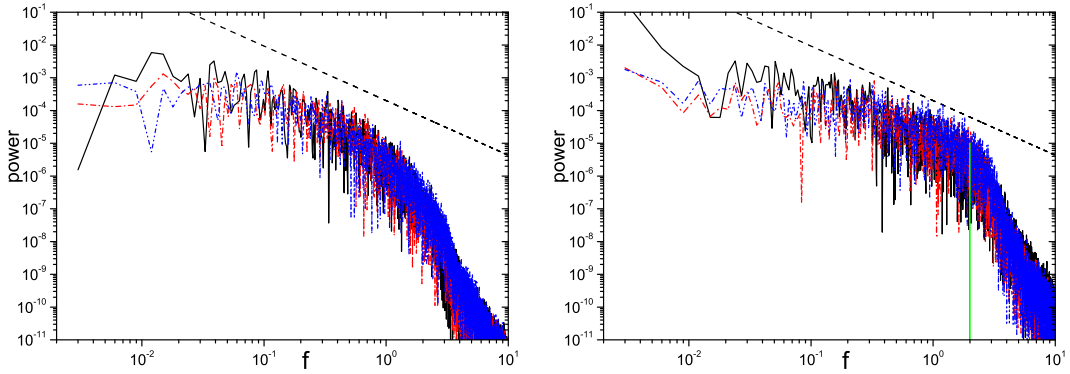
(a) Point E, in the center of recirculation re-
gion $x_1/H = 2.15$, $x_2/H = 0.49$.

(b) Point D, in the center of free shear layer
$x_1/H = 2.23$, $x_2/H = 1.13$.

Figure 5.14: Power-spectrum density of three velocity component in $HTBLE\_C$
of two points at $Re_H = 10,595$. Solid line: E_{uu}; dashdotted line: E_{vv}; dashdot-
dotted line: E_{ww}; dashed line: $0.0002f^{-5/3}$; vertical solid line: critical frequency
of second-order central scheme.

velocities, except at $x_1/H = 8.0$. Although the pressure gradient is favorable and
the nondimensional wall distance of the LES/TBLE coupling point is 58.5 at that
location, large discrepancy from resolved LES can be observed. The reason for
this discrepancy is that the boundary layer at this position is strongly unsteady
and exhibits a 'splatting' phenomenon of large scale eddies [52].

The turbulent kinetic energy and Reynolds stresses are predicted reasonably
well and the discrepancies of them using different wall models are small, which
resembles in the backward-facing step having massive separation. The Reynolds
shear stress is overpredicted in the separated free-shear layer, as shown in Fig.
5.13(f), which is responsible for the overpredicted turbulent kinetic energy, and
is caused by the relatively coarse resolution.

5.2.2.2 Spectra of velocity

To assess the grid resolution the spectra of the time series of velocity are obtained
using windowed fast Fourier transform with a Hanning window. The velocity
signals are recorded for the case $HTBLE\_C$ during the data accumulation at
several points on the center plane without spanwise averaging as shown in Fig.
5.1(b). Using Taylor's hypothesis, the spectra in time can be related to the spectra
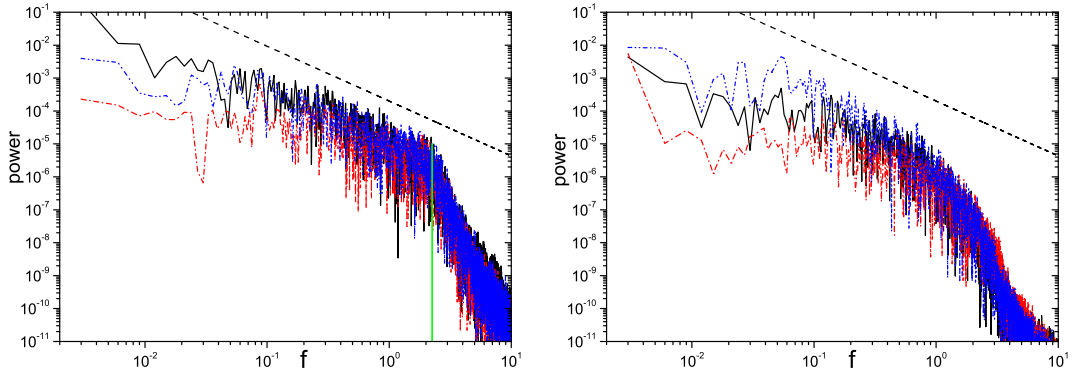
(a) Point A, on the top of the hill $x_1/H = 0.0$, (b) Point G, in the accelerating region $x_1/H =$
$x_2/H = 1.1$.   8.1, $x_2/H = 0.65$.

Figure 5.15: Power-spectrum density of three velocity component in $HTBLE\_C$
of two near-wall points at $Re_H = 10,595$. Lines labled as in Fig. 5.14.

in space, which requires the average velocity to be substantially larger than the
fluctuations. In the center of the recirculation region, point E $x_1/H = 2.15$,
$x_2/H = 0.49$, this requirement cannot be satisfied, while it can be satisfied in the
center of the free shear layer, point D $x_1/H = 2.23$, $x_2/H = 1.13$.

The power-spectrum densities of three velocity components at these two points
are shown in Fig. 5.14. It is obviously that each spectra has low-frequency
energy-containing range, middle regular-decay range and high-frequency fast-
decay range. However, there is no long regular-decay range having slope of $-5/3$
observed as in resolved LES of Fröhlich [52]. This means the inertial subrange is
not resolved with this coarse grid resolution, which is consistent with the analysis
of the Reynolds stresses. The smooth transition from the regular decay to fast
decay in the recirculation region and the abrupt change between these two regions
are observed on the coarse resolution as in the resolved LES [52]. Since it is very
difficult to determine the modified wavenumber of ALDM, the critical frequency
$f = \langle u \rangle / (4\Delta x_1)$ defined by the modified wavenumber of second-order central
scheme is given as a reference. The abrupt change takes place at a slightly larger
frequency than this reference, which indicates that effective resolution property
of ALDM is better than the classical LES with second-order central schemes.

The power-spectrum densities at two near-wall points A and G, $x_1/H = 0.0$,
$x_2/H = 1.1$ and $x_1/H = 8.1$, $x_2/H = 0.65$, are shown in Fig. 5.15. The

former is on the top of the hill, and the latter is in the accelerating flow region before the hill. These spectra do not resemble those in the near-wall region, compared with the results of resolved LES of Fröhlich [52], but resemble that in the outer layer, which is consistent with the concept of wall modeling. At the point A, the spectra exhibit a long inertial subrange with slope $-5/3$. As the mean velocity is almost four times larger than the streamwise fluctuating velocity, the requirement of Taylor's hypothesis can be satisfied, therefore the grid resolution there is sufficient. At point G it can be observed that the power-spectra density of the spanwise velocity w is higher than that of u and v, which corresponds to the 'splatting' phenomenon mentioned above.

5.2.2.3   Realizable states of the flow turbulence

Although the Reynolds stresses are predicted reasonably well using wall models, it is necessary to check whether the predicted turbulence states satisfy the realizability constraints. A convenient way is to check the invariants of the anisotropy tensor of the Reynolds stress. The anisotropy tensor b_{ij} is defined using the Reynolds stress $\langle u_i u_j \rangle$ as

$$b_{ij} = \frac{\langle u_i u_j \rangle}{\langle u_k u_k \rangle} - \frac{1}{3}\delta_{ij}, \tag{5.1}$$

where δ_{ij} is the Kronecker delta. As the anisotropy tensor has zero trace it has only two independent invariants II and III, calculated as

$$II = -\frac{b_{ij}b_{ji}}{2}, \quad III = \frac{b_{ij}b_{jk}b_{ki}}{3}. \tag{5.2}$$

Conveniently one defines ξ and η from the invariants III and II as

$$\xi = \left(\frac{III}{2}\right)^{1/3}, \quad \eta = \left(-\frac{II}{3}\right)^{1/2}. \tag{5.3}$$

In the (ξ, η)-diagram, the well-known Lumley triangle exhibits two straight sides [143], and the departure from isotropy indicated by η becomes evident.

All physically realizable turbulence has to lie within the triangle, as shown in Fig. 5.16, which is corresponds to the real eigenvalues of the anisotropy tensor. The left side with $\eta = -\xi$ is called axisymmetric contraction, where the anisotropy

(a) $x_1/H = 0.5$

(b) $x_1/H = 2.0$

(c) $x_1/H = 6.0$

(d) $x_1/H = 8.0$
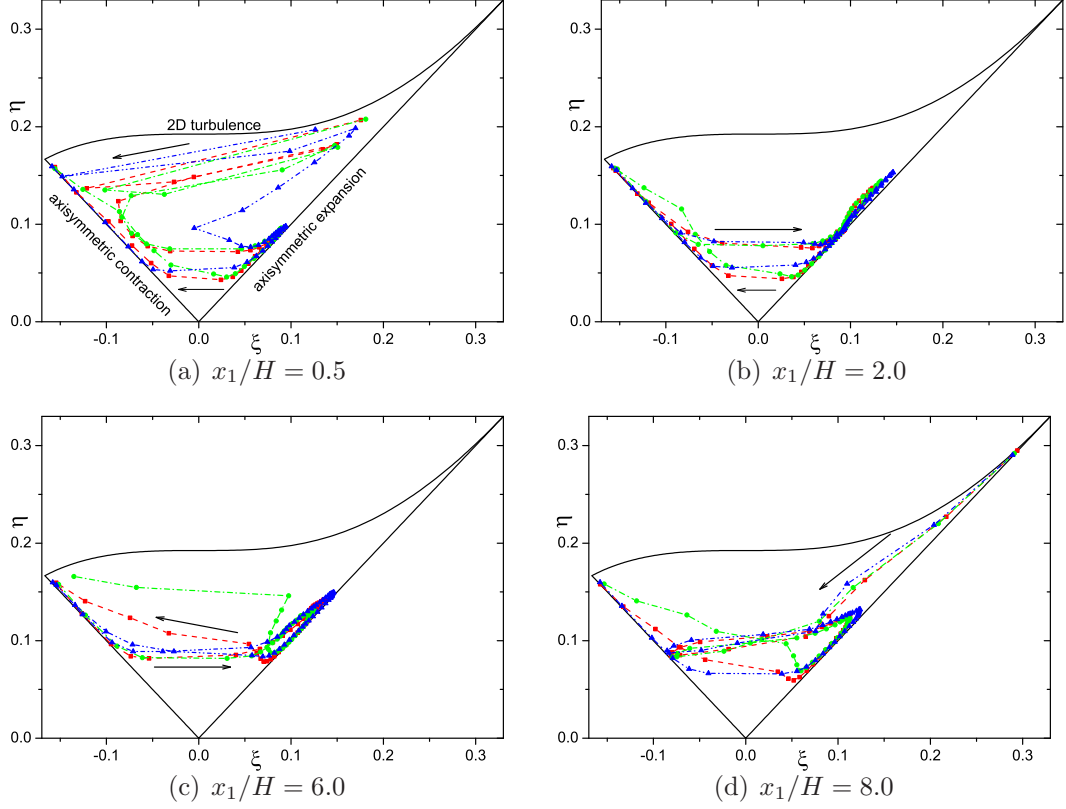
Figure 5.16: Invariant maps along vertical lines at four streamwise locations.

tensor only has one small eigenvalue, which means that one component of the velocity fluctuations is smaller than the other two. The right side with $\eta = \xi$ is called axisymmetric expansion, where the anisotropy tensor only has one large eigenvalue, which means that one fluctuating component dominates the other two. The upper side with $\eta = (\frac{1}{27} + 2\xi^3)^{1/2}$ is called two-dimensinal turbulence, where the sum of the two eigenvalues of anisotropy tensor is $1/3$, which means that the fluctuation has only two components. On the bottom, the point with $\xi = 0$ and $\eta = 0$ is called the isotropic point, where all the eigenvalues are zero, which is corresponding to the isotropic turbulence. At left upper corner point $\xi = -\frac{1}{6}$ and $\eta = \frac{1}{6}$, the two eigenvalues equal to $\frac{1}{6}$, where the turbulence has two equal components. At the right upper corner point $\xi = \eta = \frac{1}{3}$, one large eigenvalue equals to $\frac{2}{3}$ and the other two equal to $-\frac{1}{3}$, the turbulence has only one component.

121

The results of coarse LES using three wall models are shown in the Fig. 5.16 at four streamwise sections across the channel, where the arrows point from the lower wall to the upper wall. It can be seen that all simulated turbulence states lie within the triangle, which means the requirement of realizability constraints is satisfied, although they are far from those of highly resolved LES of Breuer *et al.* [21]. Another global observation is that all the states do not start from the two-dimensional turbulence on the upper side of the triangle and do not end there either, due to the unresolved near-wall region on the coarse grid resolution. The results of WW are much different from that of GWFP and TBLE near the upper wall.

At section $x_1/H = 0.5$, the turbulence state of the point near the lower wall resembles two-dimensional turbulence. At the lower part of the channel, the states exhibit complex variations, and the results of three wall models are much different. Near the upper wall, the states tend to axisymmetric contraction. At $x_1/H = 2.0$ and $x_1/H = 6.0$, the turbulence states exhibit a clear free shear layer region near the axisymmetric-expansion side. Therefore, the turbulence states near two walls resemble the edge of the mixing layer with negative ξ at section $x_1/H = 2.0$ in both cases using GWFP and TBLE. The state of the first off-wall point at $x_1/H = 8.0$ shows that the turbulence has only one components, which is consistent with the large spanwise fluctuation there.

5.2.3 Results for the periodic hill at $Re_H = 37,000$

To assess the resolution dependence of the wall-modeling LES on Reynolds number, two grid resolutions are used in the simulations at $Re_H = 37,000$. As the streamwise mean velocity of the case using the TBLE model is better than those of GWFP and WW at $Re_H = 10,595$, only TBLE is applied here. As there are no results on friction and pressure coefficients of resolved LES, only the mean velocities and Reynolds stresses are compared with that of resolved LES using MGLET [145] at ten sections in Fig. 5.17.

The mean velocities are stronger overpredicted than that at $Re_H = 10,595$ on the coarse resolution, because of less resolved LES at this higher Reynolds number. However, when the resolution increases, the streamwise mean velocities

(a) Mean streamwise velocity   (b) Mean vertical velocity

(c) Streamwise Reynolds normal stress   (d) Vertical Reynolds normal stress

(e) Turbulent kinetic energy   (f) Reynolds shear stress
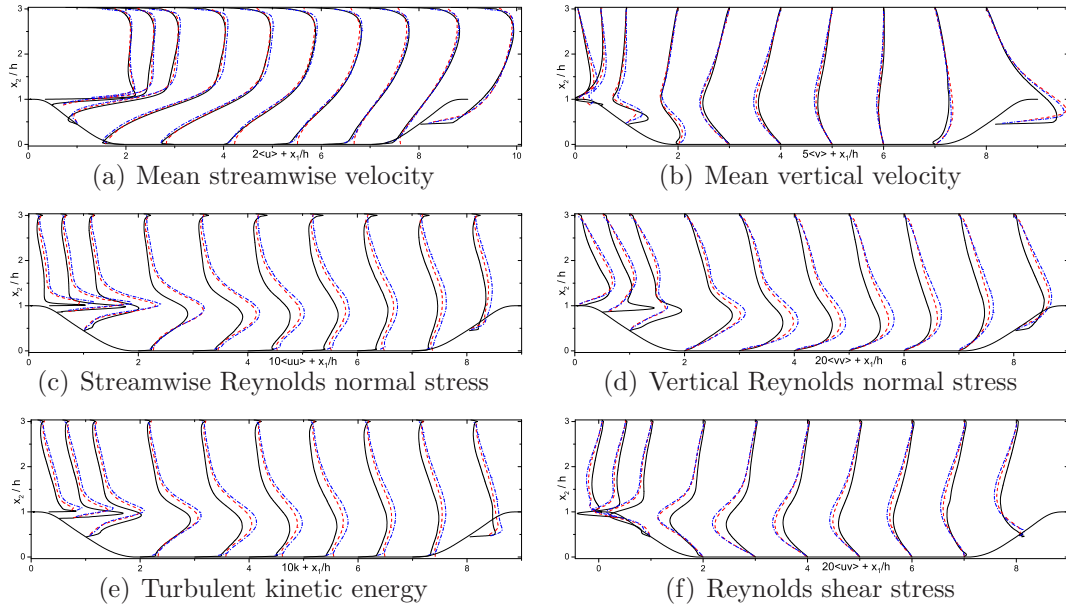
Figure 5.17: Comparisons of mean velocities and Reynolds stresses for periodic hill at $Re_H = 37,000$, on two resolutions. Solid line: Rapp [145]; dashed line: $HHTBLE\_C$; dashdotted line: $HHTBLE\_F$.

become worse at the stations in the separation region. Because a large and strong recirculation is produced on the fine resolution, the mean streamwise velocities near the lower wall are underpredicted. Therefore, they are overpredicted near the upper wall under the constraint of constant mass flux, which leads to the higher shear rate. After $x_1/H = 3.0$, the mean velocities are improved near both walls. The tendency of vertical mean velocity is worse than that on the coarse resolution before the station $x_1/H = 6.0$. The comparisons of turbulent kinetic energy and Reynolds stresses show that higher turbulent kinetic energy is reproduced due to the higher turbulence production on the fine resolution.

This investigation shows that even though the grid resolution is increased, the flow quantities cannot be improved globally, but rather deteriorate at some sections. This is mainly because that the wall model cannot approximate correctly the flow dynamics in the recirculation region, even when the resolution of the exterior LES increases.

5.2.4   Conclusions on the periodic-hill flow

Concerning the mean flow quantities, *e.g.* friction and pressure coefficients and mean velocities, the TBLE model performs better than GWFP and WW. However, the discrepancies of Reynolds stresses are small, even though the modeled wall friction has large difference. This resembles in the case of backward-facing step having a massively separated flow region, but it is different for the bump case having a very shallow separation. The velocity spectra at near-wall points have no near-wall characteristics as in resolved LES, but resemble that of the outer flow regions. Two kinds of transition of the energy decay can be recovered as in the resolved LES. Based on the analysis of invariants of anisotropy tensor, the predicted turbulence is physically realizable using the wall models and coarse resolution. The indication of typical flow features, such as a free shear layer, can be observed, although the detail of the invariant maps is far from that of resolved LES. The TBLE model cannot improve the predicting results, when the resolution increases. This failure resembles that of GWFP and WW on the finer grid resolution in the bump case. Another shortcoming is that the predicted wall-shear stress strongly depends on the pressure gradient, which confirms the former finding.

5.3   Application for the circular cylinder using AMR

In all the above applications, there is only one block used for the computational domain with equally distributed grid resolution, and the Reynolds numbers are just moderately high. In the present case, the Reynolds number $Re_D = 1.0 \times 10^6$ based on the freestream velocity and the diameter of the circular cylinder is very large. Therefore, the grid resolution near the immersed interface is required to be fine enough to let the coupling position of the wall model and the exterior LES be not far from the boundary of the wall layer. The AMR technique described in section 2.3 is used to locally refine the grid near the immersed interface.

The computational domain is $40D \times 20D \times \pi D$ in the streamwise, vertical and spanwise directions, respectively. The upstream length is $10D$ from the inlet to

(a) Multi-blocks of the computational domain   (b) Local girds and flow fields

Figure 5.18: Results of AMR and local flow fields.

the center of the cylinder. The refinement starts from one block with 24 grid cells stretched in streamwise and vertical directions and 32 equally distributed grid cells in the spanwise direction, and ends at 59 blocks with non-equally distributed grid resolution and around 2.6 million cells, without the spanwise refinement, as shown in Fig. 5.18.

A uniform inflow condition is used at the inlet, and the turbulence intensity is set to zero. A second-order Neumann boundary condition is applied at the outlet. Slip walls are used at the two boundaries in the vertical direction. Periodic conditions are adopted in the spanwise direction. The communication of the flow variables between two blocks is accomplished using the algorithm given in section 2.3. On the immersed interface the TBLE model is applied. In the framework of wall modeling, an additional difficulty due to the multiple blocks is that the coupling position and its interpolating points should lie in a local block where the immersed interface presents. Otherwise, it needs to use a complicated and expensive method to find these points in its neighbor blocks. Thanks to the buffer region of each block, this difficulty can be avoided. Because of the complexity of the boundary layer on the cylinder, it is difficult to take the laminar-turbulent transition into account. No special treatment is used, but rather a fully turbulent condition is employed. Although the grid resolution is refined near the interface, the coupling position is still far from the edge of the wall layer, and the maximum couping wall distance is $x_2^+ = 1607$ in wall units based on the friction velocity from TBLE model at the windward side $\theta = 57.7°$ and $\theta = 302.3°$.

The computation is carried out on 10 cores using MPI to communicate the

Table 5.2: Mean flow variables of flow around a circular cylinder at $Re_D = 1 \times 10^6$

$Case$	C_D	$-C_{p,base}$	St	L_r/D
$TBLE\_LES$	0.26	0.34	0.26	0.95
WM_LES[30]	0.31	0.32	0.35	1.04
$Exp.$[157]	0.24	0.33	0.22	-
$Exp.$(Others [187])	0.17-0.40	-	0.18-0.50	-

interface information. The CFL is 0.75 and the total simulation time is 2.5 flow-through times. the statistics are accumulated during the last one flow-through time.

The drag coefficient C_D, base pressure coefficient $C_{p,base}$, Strouhal number St and mean-recirculation length L_r/D are shown in Tab. 5.2 compared with the results of wall-modeling LES of Catalano *et al.* [30] and the experiments. All these flow variables are predicted reasonably well. The shape of the recirculation is shown in Fig. 5.18(b). It is obvious that the height of the wake is smaller than the diameter of the cylinder.

The friction coefficient returned from TBLE model and the pressure coefficient are compared with the experimental results in Fig. 5.19. The wall friction is overpredicted under the favorable pressure gradient and underpredicted under adverse pressure gradient as in the bump and periodic hill cases, while the different Reynolds numbers between wall-modeling LES and the experiment only account for a small fraction of this discrepancy as analyzed by Catalano *et al.* [30]. The separation angle is $\theta_s = 95.6°$ indicated by the zero friction coefficient, but it is 150.8° deduced from the streamline perpendicular to the wall. This discrepancy is caused by the defect of TBLE model and coarse resolution as analyzed in periodic hill simulation.

In the front part of the cylinder, the pressure distribution is predicted reasonably well, for the normalized pressure is nearly independent of the Reynolds number there. However, it is under predicted in the region $70° < \theta < 120°$, which may be caused by the under predicted wall-shear stress as shown in Fig. 5.19(a). This much lower wall friction cannot drive the flow back in the exterior LES, but makes it much slower, therefore, the pressure is much higher. In the base region, it is reasonable that the pressure lies between the experiments at higher and lower
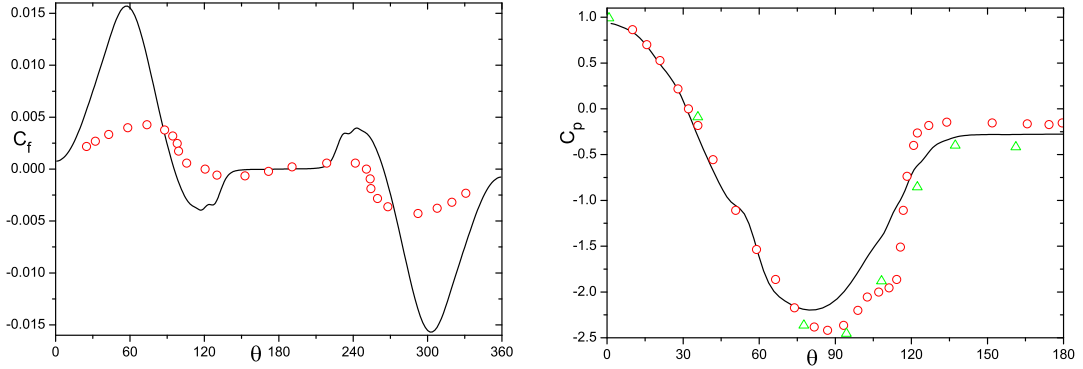
(a) Friction coefficient comparison. Solid line: $TBLE\_LES$; circle: experiments of Achenbach [1] at $Re_D = 3.62 \times 10^6$.

(b) Pressure-coefficient comparison. Solid line: $TBLE\_LES$; circle: experiment of Falchsbart (in Ref. [187]) at $Re_D = 6.7 \times 10^5$; uptriangle: experiment of Warschauer (in Ref. [30]) at $Re_D = 1.2 \times 10^6$.

Figure 5.19: Friction- and pressure-coefficient distributions on the cylinder.

Reynolds numbers than in the wall-modeling LES. A kink around $\theta = 110°$ can be found from the experimental results of Flachsbart at $Re_D = 6.7 \times 10^5$. This is the characteristic of the supercritical regime of flow over circular cylinder, where the boundary layer separates laminarly, followed by a turbulent reattachment, thus a separation bubble appears, and the transition happens on the top of the recirculation bubble. This process is difficult to be reproduced numerically or experimentally, because it is very sensitive to the disturbance, such as imposed by the freestream turbulence level or surface roughness. The TBLE model can not account for this flow dynamics either.

Due to the lack of the experimental data, the mean velocity and Reynolds stresses of the wall-modeling LES are compared at four streamwise locations in Fig. 5.20. The mean streamwise velocity profile exhibits 'U' shape at $x_1/D = 0.6$, and changes to 'V' shape at downstream locations, which is usually observed in experiments and resolved LES at low Reynolds numbers. The mean vertical velocity is larger before the cylinder than behind, and it exhibits a complex shape in the recirculation region. At the location $x_1/D = -0.75$, the Reynolds normal stresses are very small, but non zero, and exhibit very complex shape (not shown). They become large in the separated shear layer, which corresponds to the

(a) Mean streamwise velocity

(b) Mean vertical velocity

(c) Streamwise Reynolds normal stress

(d) Streamwise Reynolds normal stress

(e) Vertical Reynolds normal stress

(f) Vertical Reynolds normal stress
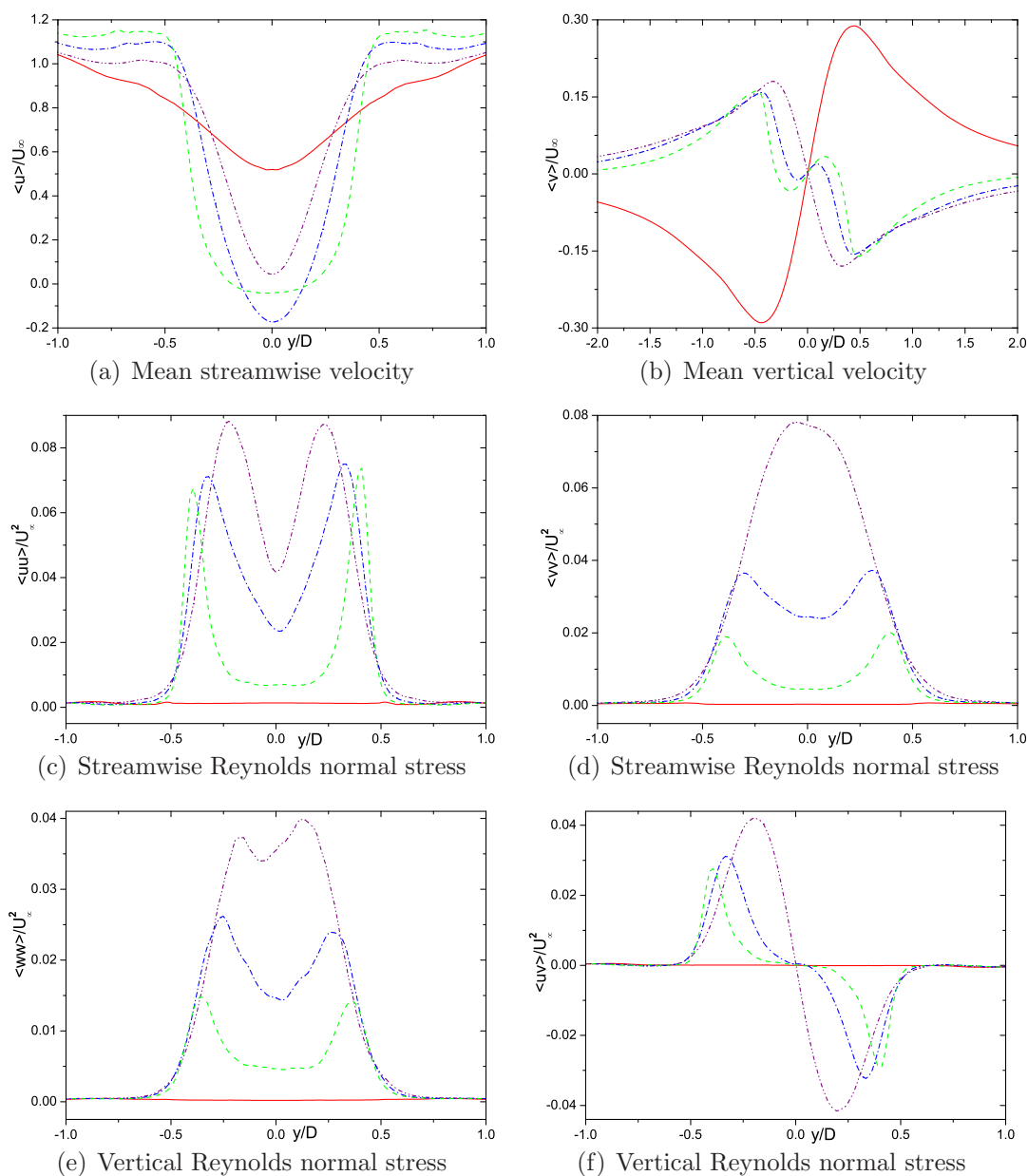
Figure 5.20: Comparisons of mean velocities and Reynolds stresses at four streamwise locations. Solid line:$x_1/D = -0.75$; dashed line: $x_1/D = 0.6$; dashdotted line: $x_1/D = 1.0$; dashdotdotted line: $x_1/D = 1.5$.

(a) Invariant maps.

(b) Power-spectrum density. Lines labeled as in Fig. 5.14.
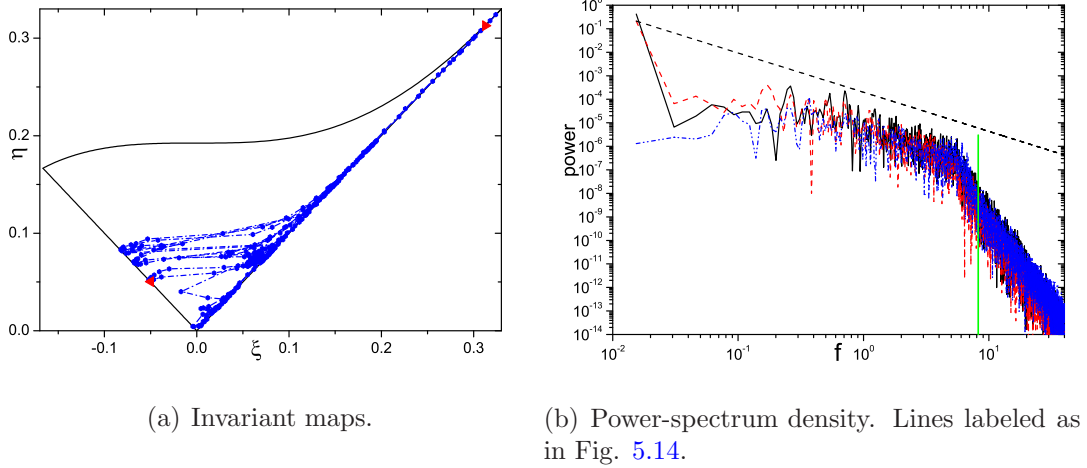
Figure 5.21: Invariant maps at station $x_1/D = 1.0$ and power-spectrum density of three velocity components at point $x_1/D = -0.4$, $x_2/D = -0.5$.

increased Reynolds shear stress. From the profiles of Reynolds normal stresses, it can be observed that these profiles are asymmetric. This is caused by the staggered-grid arrangement in the framework of CIIM, although the configuration is symmetric.

To assess turbulence anisotropy, for clarity, only the upper half of the invariant maps in the vertical direction at $x_1/D = 1.0$ near the center of recirculation region is shown in Fig. 5.21(a). The right triangle indicates the point on the edge of the computational domain, where the the turbulence approaches one component. The left triangle indicates the point on the horizontal center line, where the turbulence has two large dominant components. In a global view, the turbulence there resembles that of a free shear layer. However, it looks like that several free shear layers are composed together, and each has its own edge reaching the axisymmetric contraction side of the Lumley triangle.

The power-spectrum density of three velocity components at $x_1/D = -0.4$, $x_2/D = -0.5$ is shown in Fig. 5.21(b). It is obvious that the spectrum has the characteristics of fully developed turbulence, and exhibits a longer inertial range having a slope of $-5/3$, even before the circular cylinder. And the Reynolds stresses are very small. Another interesting observation is that a spectral peak of three velocity components locates at $f \approx 0.26$, which corresponds to the Strouhal

number.

From the above investigation, it is evident that reasonable results are obtained using wall-modeling LES in the framework of AMR, even on coarse resolution at such high Reynolds number. It indicates that the wall modeling for implicit LES combining CIIM and AMR is a potential framework to apply the LES in practical engineering. It also shows the defect of TBLE based modeling.

Chapter 6

Conclusions

To avoid the statistical model dependence of RANS and the high cost of DNS, LES has been established as an alternative. However, in wall-bounded flows turbulent flow structures are highly anisotropic in the thin wall layer. Therefore, the grid resolution requirement approaches that of DNS, which makes the computational cost so high that LES is hardly affordable at high Reynolds numbers. Wall models have been developed to bypass the expensive wall layer for explicit LES using body-fitted grids, and the SGS-modeling and wall-modeling errors are found to play a crucial role.

A wall modeling method for implicit LES using ALDM has been constructed and investigated in detail. First, the method has been developed for the body-fitted mesh, which is realized using the wall-shear stress as approximate boundary condition for exterior LES directly, where the effects of SGS-modeling error and wall modeling error are distinguished, and are eliminated or alleviated separately. To treat complex flows along complex geometries, the wall modeling method for implicit LES is also constructed using CIIM in the framework of finite volume methods, which is accomplished by using the wall-shear force as source terms in the momentum equations. These source terms function as approximate boundary condition for the exterior LES, meanwhile they provide the no-slip wall boundary conditions for CIIM indirectly. Three kinds of wall-stress model based on a generalized wall function with pressure correction, a two-layer power law, and a simplified TBLE wall-layer modeling are investigated for the canonical TCF and separated flow along a backward-facing step in detail. They are also applied to

two different separated flows along two different hills at moderately high Reynolds numbers. At last, the wall modeling with CIIM is extended to multi-block computational domains using AMR, and a preliminary investigation is carried out on a flow over a circular cylinder at very high Reynolds number.

Compared with coarse LES without wall modeling, the effect of wall models is to reduce SGS-modeling error caused by the relatively large grid cells near the wall, through the wall-tangential momentum balance. However, SGS-modeling error, which is not caused by the coarse resolution but by the SGS model itself, such as the wall-asymptotic behavior at high Reynolds numbers, cannot be reduced by wall modeling.

SGS-modeling error caused by wall damping results in a mean velocity mismatch with the logarithmic law in the simulation of TCF at very high Reynolds numbers. This mismatch cannot be improved by using more accurate wall models, but has to be solved using a physically motivated near-wall SGS modeling, such as the one based on coherent structures adopted in the investigation. The improvement is accomplished through the momentum balance in several near-wall cells.

The wall-modeling error appearing as incorrect wall-shear stress provided to the exterior LES mainly leads to a upward or downward shift of the scaled mean velocity profile. When the wall-shear stress is underpredicted the scaled mean-velocity profile moves upwards, and the resulting flow resembles that at lower Reynolds numbers. Otherwise, the scaled mean velocity profile moves downwards, and the resulting flow resembles that at higher Reynolds numbers. However, the shape of the mean-velocity profiles has no large change according to different wall-shear stress.

The effect of modeling parameters of simplified TBLE model is mainly controlled by the resulting wall-shear stress supplied to the exterior LES. The flow dynamics, *i.e.*, the momentum balance, turbulent production are just affected in the several near-wall cells of the exterior LES. It is also found that the coupling position is a crucial wall-modeling parameter, because the logarithmic mean-velocity profile starts from that position, and the exterior LES can only resolve the large energy-carrying structures on the coarse resolution. Therefore, the expected coupling position lies at the beginning or bottom of the logarithmic layer.

If the coupling position is proper, and the wall model can account for the near-wall flow dynamics well, the predicted results converge to that of resolved LES or DNS, when the grid resolution increases.

In the investigation of the flow along the backward-facing step with massive separation induced by an abrupt geometric change, it is found that the effect of the wall-modeling error is trivial concerning the results of mean velocity and Reynolds stresses. However, different effects of wall models are observed on the secondary flow at the bottom corner of the step using body-fitted grids. Upstream of the separation, different wall models return much different wall-shear stresses, while the mean velocity and Reynolds stresses are not sensitive to these difference. When these wall models are realized in the framework of CIIM, the difference on the secondary flow disappears, and no secondary-separation bubble can be observed at all. This is because numerical errors, especially as numerical dissipation, are introduced by the mixing procedure of CIIM, which conceals the difference of the wall models. In the massive recirculation region, the exterior LES is insensitive to the wall-modeling error, but it becomes sensitive in the recovery region. The artificial mixing introduced by the mixing procedure of CIIM has a favorable influence on the predicted results concerning the recovery pressure and Reynolds stresses in the recovery region. The difference of wall models becomes much smaller in the framework of CIIM than when using body-fitted mesh in this massively separated flow.

The methods are applied to two separated flows along the two different hills at moderately high Reynolds numbers. One is a quasi-steady flow along a shallow bump, which resembles the flow over the upper surface of an airfoil, using inflow/outflow boundary conditions. Another is a highly unsteady flow over a periodic hill having a massive separation. The results of wall-modeling LES compare reasonably well with that of DNS and resolved LES, respectively. The results also indicate that the exterior LES is sensitive to wall-modeling error in the bump case concerning the predicted mean velocity and Reynolds stresses, especially in the recovery region. The separation is so shallow that all wall models fail to reproduce it on very coarse grids. We also find that the results can only be improved using a proper wall model which can account for near-wall flow dynamics well, when the resolution increases. Otherwise, they deteriorate. If the recycling

length is not long enough using recycling/rescaling inflow boundary condition, artificial flow structures are observed.

In the periodic hill case, the sensitivity of exterior LES to the wall modeling error becomes trivial concerning the results of mean velocity and Reynolds stresses. When the grid resolution increases, globally improved results cannot be obtained because of the defect of TBLE model in the massive recirculation region. But the improved results are realized in the recovery and reacceleration regions, where TBLE works reasonably well. Through the analysis of invariants of turbulence anisotropy, all the turbulence states in wall-modeling LES are realizable using all wall models. The local spectral analysis of three velocity components can be used to evaluate the grid resolution *a posteriori* and to assess the turbulence states.

The wall modeling in the framework of ALDM and CIIM combing AMR is applied to complex flow along a circular cylinder at very high Reynolds number. The global flow quantities are predicted reasonably well, which shows that this wall modeling methodology has the potential to be a practical simulation tool in engineering.

Among the investigated wall models, the best one is the TBLE model, which can account for much more near-wall flow dynamics. It can return correct wall-shear stress at all Reynolds numbers in the simulations of TCF, and produces better results in the simulations of separated flows, concerning wall friction, mean velocity and Reynolds stresses. However, it also exhibits strong dependence on the pressure gradient term in simplified TBLE, where the nonlinear convective terms are omitted. It cannot account for the flow dynamics in the recirculation and recovery regions well, which is beyond the validity of the thin boundary layer assumption. The second one is the generalized wall function with pressure correction. It can return correct wall-shear stress at high Reynolds numbers in TCF cases, and predicts better results than Werner and Wengle two-layer power law based formulation. The integral formulation of Werner and Wengle law always overpredicts the wall-shear stress in the attached flow regions. However, it can reproduce the secondary separation bubble better than the other two models in the backward-facing step case using body-fitted grids. Therefore, these wall models also exhibit flow-case dependence.

It can be concluded that a proper wall model can improve the prediction

of coarse LES with proper SGS modeling. However, it also confirms the prior finding using explicit SGS models on body-conforming grids that only using the wall-shear stress as an approximate boundary condition is not enough in wall-modeling LES, but some information of the turbulence structures are required, such as the instantaneous wall-shear stress fluctuation introduced by the pressure gradients in the flow over the bump having very complex pressure gradient. In order to improve the wall modeling of LES, further research on the near-wall SGS modeling and the wall-layer coherent structures modeling are required.

Appendix A

Interpolation Methods

Three interpolation methods are adopted to obtain the flow variables for wall models from the exterior LES. In the following, these methods are described in detail.

A.1 Linear least square interpolation

This interpolation method uses more than three interpolation points to interpolate a flow variable at the coupling points between the wall models and the exterior LES. It is expected that this method is better than the linear interpolation in three dimensions, as it solves an overdetermined linear equation set according to the minimum energy principle. The formulation of this method is given in the following.

Using N points to interpolate a flow variable ϕ at point $\mathbf{x}_p = (x_p, y_p, z_p)$. The overdetermined system of linear equations can be expressed as :

$$A\nabla\phi = \Delta\phi, \tag{A.1}$$

where

$$A = \begin{bmatrix} \Delta x_1 & \Delta y_1 & \Delta z_1 \\ \vdots & \vdots & \vdots \\ \Delta x_N & \Delta y_N & \Delta z_N \end{bmatrix}, \quad \nabla \phi = \begin{bmatrix} \nabla_x \phi \\ \nabla_y \phi \\ \nabla_z \phi \end{bmatrix}, \quad \Delta \phi = \begin{bmatrix} \Delta \phi \\ \Delta \phi \\ \Delta \phi \end{bmatrix}. \tag{A.2}$$

The least-squares method is used to obtain the pseudo inverse of matrix A, then the gradient of ϕ can be expressed as

$$\nabla \phi = A^{-1} \Delta \phi, \tag{A.3}$$

and the pseudo inverse metrix A^{-1} is

$$A^{-1} = (A^T A)^{-1} A^T. \tag{A.4}$$

The components of the gradient of ϕ can be expressed explicitly as

$$\nabla_x \phi = \frac{1}{C} \sum_{n=1}^{N} \left[(c_2 + c_3)(x_n - x_0) - c_4(y_n - y_0) - c_5(z_n - z_0) \right] (\phi_n - \phi_0)$$

$$\nabla_y \phi = \frac{1}{C} \sum_{n=1}^{N} \left[-c_4(x_n - x_0) + (c_1 + c_3)(y_n - y_0) - c_6(z_n - z_0) \right] (\phi_n - \phi_0)$$

$$\nabla_z \phi = \frac{1}{C} \sum_{n=1}^{N} \left[-c_5(x_n - x_0) - c_6(y_n - y_0) + (c_1 + c_2)(z_n - z_0) \right] (\phi_n - \phi_0)$$

$$C = c_1 c_2 + c_1 c_3 + c_2 c_3 - c_4^2 - c_5^2 - c_6^2,$$

(A.5)

where the subscript "0" denote the base point of interpolation. This point could be one of the N interpolation points or other point surrounded by these N points. The closest point of $N = 8$ points surrounding $\mathbf{x}_p$ is used here. And the coefficients $c_i (i = 1 \sim 6)$ only depend on the coordinates of the interpolation and base points.

They are defined as

$$
\begin{aligned}
c_1 &= \sum_{n=1}^{N}(x_n - x_0)^2, \\
c_2 &= \sum_{n=1}^{N}(y_n - y_0)^2, \\
c_3 &= \sum_{n=1}^{N}(z_n - z_0)^2, \\
c_4 &= \sum_{n=1}^{N}(x_n - x_0)(y_n - y_0), \\
c_5 &= \sum_{n=1}^{N}(x_n - x_0)(z_n - z_0), \\
c_6 &= \sum_{n=1}^{N}(y_n - y_0)(z_n - z_0).
\end{aligned}
\tag{A.6}
$$

At last using the gradient of ϕ at the base point, the interpolated value of ϕ_p can be computed as

$$
\phi_p = \phi_0 + (x_p - x_0)\nabla_x\phi + (y_p - y_0)\nabla_y\phi + (z_p - z_0)\nabla_z\phi.
\tag{A.7}
$$

A.2 Trilinear interpolation

For the backgroud Cartesian mesh, trilinear interpolation in a box provides a convenient method to obtain the value ϕ_p at a interpolation point $\mathbf{x}_p = (x_p, y_p, z_p)$. This is accomplished as following. Denote flow variables at eight grid nodes $\phi_{l,m,n}(l = 0 \sim 1, m = 0 \sim 1, n = 0 \sim 1)$. These grids form a regular Cartesian cell as shown in Fig. A.1. Scale this cell to a cubic and define interpolation coefficient α, β and γ as

$$
\alpha = \frac{x_p - x_i}{x_{i+1} - x_i}, \quad \beta = \frac{y_p - y_j}{y_{j+1} - y_i}, \quad \gamma = \frac{z_p - z_k}{z_{k+1} - z_k}.
\tag{A.8}
$$
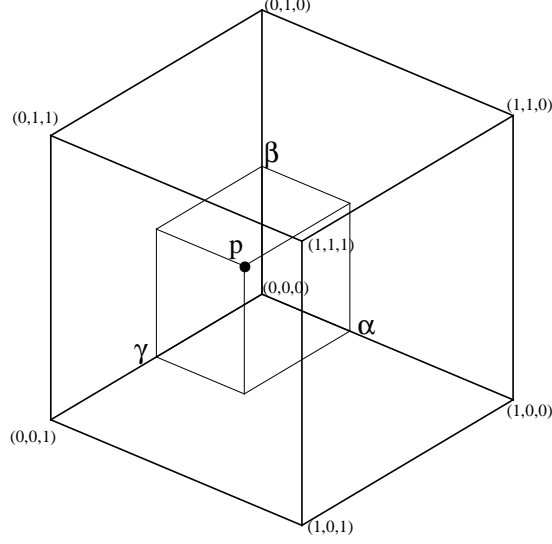
Figure A.1: Sketch of trilinear interpolation.

Then the interpolated value ϕ_p can be obtained using

$$
\begin{aligned}
\phi_p &= \phi_{0,0,0}(1-\alpha)(1-\beta)(1-\gamma) + \phi_{1,0,0}\alpha(1-\beta)(1-\gamma) \\
&+ \phi_{0,1,0}(1-\alpha)\beta(1-\gamma) + \phi_{0,0,1}(1-\alpha)(1-\beta)\gamma \\
&+ \phi_{1,0,1}\alpha(1-\beta)\gamma + \phi_{0,1,1}(1-\alpha)\beta\gamma \\
&+ \phi_{1,1,0}\alpha\beta(1-\gamma) + \phi_{1,1,1}\alpha\beta\gamma
\end{aligned}
\tag{A.9}
$$

A.3 Pseudo-Laplacian weighted method

The flow variable ϕ_p at a interpolation point can be obtained by a weighted average of the values $\phi_n(n = 1 \sim N)$ of its N surrounding points as

$$
\phi_p = \left(\sum_{n=1}^{N} w_n \phi_n \right) / \sum_{n=1}^{N} w_n,
\tag{A.10}
$$

where w_n is the weight of its each surrounding point $\mathbf{x_n}$. In the inverse-distance weighted method proposed by Franke [51], the weight is defined based on the

distance r_n from the interpolation point $\mathbf{x}_p$ to each of its surrounding point $\mathbf{x_n}$ as

$$w_n = \left(\frac{R - r_n}{Rr_n}\right)^\rho,\tag{A.11}$$

where R is the maximum of r_n and a weighting power $\rho = 2$ is always used. This formulation can preserve local maxima and produce smooth interpolation, while its accuracy is well known to be less than second-order. For a pseudo-Laplacian weighted interpolation method, proposed by Holmes and Connell [76], one can get a fully second-order accurate method for two dimensional triangular cells. This method has been extended to three dimensional in Ref. [45] and the weights are constructed to satisfy the Laplacians,

$$
\begin{aligned}
L(x_p) &= \sum_{n=1}^{N} w_n(x_n - x_p) = 0,\\
L(y_p) &= \sum_{n=1}^{N} w_n(y_n - y_p) = 0,\\
L(z_p) &= \sum_{n=1}^{N} w_n(z_n - z_p) = 0,
\end{aligned}\tag{A.12}
$$

This is a desirable property since the Laplacian of a linear function is exactly zero. And the weights are determined using

$$w_n = 1 + \Delta w_n, \quad C = \sum_{n=1}^{N} (\Delta w_i)^2,\tag{A.13}$$

where C is the cost function. It is minimized by solving an optimization problem subject to the constrains of Eq. A.12. This optimization problem is solved by the method of Lagrange multipliers, and the Δw_n is given by

$$\Delta w_n = \lambda_x(x_n - x_p) + \lambda_y(y_n - y_p) + \lambda_z(z_n - z_p).\tag{A.14}$$

The solution to the constrained optimization problem yields the Lagrange multipliers in the following as

$$
\begin{aligned}
\lambda_x &= \left[-R_x(I_{xx}I_{zz} - I_{yz}^2) + R_y(I_{xy}I_{zz} - I_{xz}I_{yz}) - R_z(I_{xy}I_{yz} - I_{yy}I_{xz}) \right] / D, \\
\lambda_y &= \left[R_x(I_{xy}I_{zz} - I_{xz}I_{yz}) - R_y(I_{xx}I_{zz} - I_{xz}^2) + R_z(I_{xx}I_{yz} - I_{xy}I_{xz}) \right] / D, \\
\lambda_z &= \left[-R_x(I_{xy}I_{yz} - I_{yy}I_{xz}) + R_y(I_{xx}I_{yz} - I_{xy}I_{xz}) - R_z(I_{xx}I_{yy} - I_{xy}^2) \right] / D,
\end{aligned}
\tag{A.15}
$$

where

$$
\begin{aligned}
D &= I_{xx}(I_{yy}I_{zz} - I_{yz}^2) - I_{xy}(I_{xy}I_{zz} - I_{xz}I_{yz}) + I_{xz}(I_{xy}I_{yz} - I_{yy}I_{xz}), \\
R_x &= \sum_{n=1}^{N}(x_n - x_p), \quad R_y = \sum_{n=1}^{N}(y_n - y_p), \quad R_z = \sum_{n=1}^{N}(z_n - z_p), \\
I_{xx} &= \sum_{n=1}^{N}(x_n - x_p)^2, \quad I_{yy} = \sum_{n=1}^{N}(y_n - y_p)^2, \quad I_{zz} = \sum_{n=1}^{N}(z_n - z_p)^2, \\
I_{xy} &= \sum_{n=1}^{N}(x_n - x_p)(y_n - y_p), \\
I_{xz} &= \sum_{n=1}^{N}(x_n - x_p)(z_n - z_p), \\
I_{yz} &= \sum_{n=1}^{N}(y_n - y_p)(z_n - z_p).
\end{aligned}
\tag{A.16}
$$

These weights are constructed entirely from geometric information of the interpolation points, and can be computed once when initializing the simulation.

Appendix B

Coherent Structures Based

Damping Model

B.1   Modeling formulation

An adaptive coefficient formulation based on coherent structures [102, 103] can be constructed using

$$\boldsymbol{\sigma}_{i,j,k} = \sigma |F_{CS}|^{3/2} F_\Omega \boldsymbol{I}_{i,j,k}, \tag{B.1}$$

where $\boldsymbol{I}_{i,j,k}$ is the units vector of Cartesian coordinates, and

$$
\begin{aligned}
F_{CS} &= \frac{Q}{E}, \quad F_\Omega = 1 - F_{CS}, \\
Q &= \frac{1}{2} \left(\overline{W}_{ij} \overline{W}_{ij} - \overline{S}_{ij} \overline{S}_{ij} \right), \\
E &= \frac{1}{2} \left(\overline{W}_{ij} \overline{W}_{ij} + \overline{S}_{ij} \overline{S}_{ij} \right), \\
\overline{W}_{ij} &= \frac{1}{2} \left(\frac{\partial \overline{u}_j}{\partial x_i} - \frac{\partial \overline{u}_i}{\partial x_j} \right), \quad \overline{S}_{ij} = \frac{1}{2} \left(\frac{\partial \overline{u}_j}{\partial x_i} + \frac{\partial \overline{u}_i}{\partial x_j} \right),
\end{aligned}
\tag{B.2}
$$

where $\overline{S}_{ij}$ and $\overline{W}_{ij}$ are the velocity-strain tensor and the vorticity tensor of the resolved flow field, respectively. F_{CS} is the coherent-structure function defined as the second invariant normalized by the magnitude of the resolved velocity gradient tensor E. For incompressible flow, the second invariant $Q \propto x_2^2$ and $E \propto const$, therefore, the 3/2 power of F_{CS} scales the implicit SGS viscosity proportionally to x_2^3 near the wall.

B.2   Preliminary validation on TCF

In order to assess whether this model can obtain SGS dissipation, it is tested on the TCF at $Re_\tau = 395$ with the resolution of $32 \times 32 \times 32$, and at $Re_\tau = 590$ with the resolution of $48 \times 48 \times 48$, without any wall model. The wall-normal grid is stretched by the hyperbolic tangent function Eq. 4.1 with $C_G = 2.5$ for these two cases to increase resolution in the vicinity of the walls. In these coarse simulations, the scaled wall distance of first grid point x_2^+ is approximately 1.0. The wall layer cannot be well resolved. Periodic boundary conditions are applied in the streamwise and spanwise directions. At the wall, the no-slip condition is employed. The pressure Poisson solver uses a fast Fourier transform in the periodic directions, and direct tridiagonal matrix inversion in the wall-normal direction.

The mean velocity and Reynolds stresses profiles are compared with the results of DNS at the same friction Reynolds numbers accordingly, in Fig. B.1. It can be seen that the mean velocities and Reynolds stresses are predicted very well, and they exhibit good wall-asymptotic behavior, which indicates that this model can be used in the wall-modeling implicit LES.
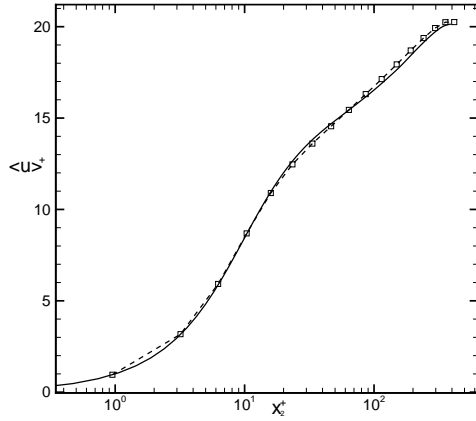
(a) Mean velocity at $Re_\tau = 395$.
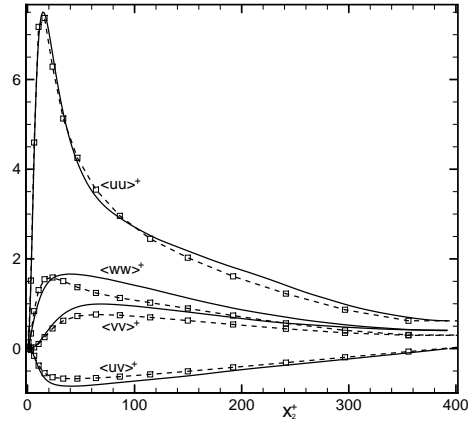
(b) Reynolds stresses $Re_\tau = 395$.
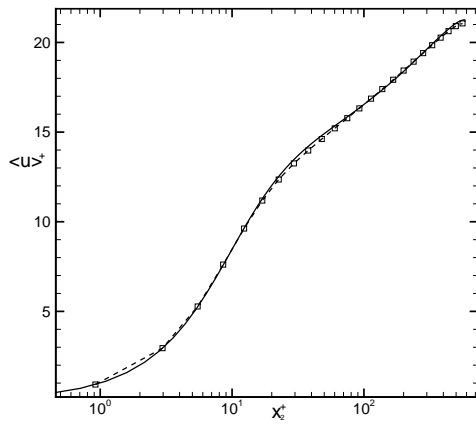
(c) Mean velocity $Re_\tau = 590$.

(d) Reynolds stresses $Re_\tau = 590$.

Figure B.1: Comparisons of mean velocity and Reynolds stresses of TCF at $Re_\tau = 395$ and 590. The solid line: DNS [126]; dashed line with square: LES with CS model.

References

[1] E. Achenbach. Distribution of local pressure and skin friction around a circular cylinder in cross-flow up to $Re = 5 \times 10^6$. *J. Fluid Mech.*, **34**:625–639, 1968. 127

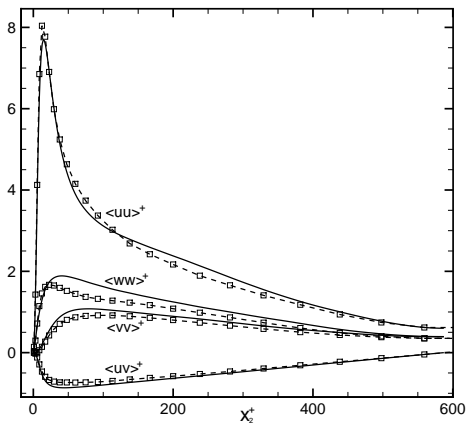[2] E. W. Adams and J. P. Johnstont. Flow structure in the near-wall zone of a turbulent separated flow. *AIAA J.*, **26**[8]:932–939, 1988. 86

[3] N. A. Adams, S. Hickel, and S. Franz. Implicit subgrid-scale modeling by adaptive deconvolution. *J. Comput. Phys.*, **200**:412–431, 2004. 16, 20, 21

[4] G. P. Almeida, D. F. G. Durao, and M. V. Heitor. Wake flows behind two-dimensional model hills. *Exp. Thermal Fluid*, **7**:87–101, 1993. 113

[5] A. E. Alving and H. H. Fernholz. Mean-velocity scaling in and around a mild, turbulent separation bubble. *Phys. Fluids*, **7**[8]:1956–1969, 1995. 9

[6] J. S. Baggett. Some modeling requirements for wall models in large eddy simulation. *CTR Annu. Res. Briefs*, pages 123–134, 1997. 11

[7] J. S. Baggett. On the feasibility of merging LES with RANS for the near-wall region of attached turbulent flows. *CTR Annu. Res. Briefs*, pages 267–277, 1998. 15

[8] J. S. Baggett, J. Jiménez, and A. Kravchenko. Resolution requirements in large-eddy simulation of shear flows. *CTR Annu. Res. Briefs*, pages 51–66, 1997. 6

[9] E. Balaras. Modeling complex boundaries using an external force field on fixed Cartesian grids in large-eddy simulations. *Computers & Fluids*, **33**:375–404, 2004. 31

[10] E. Balaras, C. Benocci, and U. Piomelli. Two-layer approximate boundary conditions for large-eddy simulations. *AIAA J.*, **34**:1111–1119, 1996. 13, 77

[11] B. S. Baldwin and H. Lomax. Thin Layer Approximation and Algebraic Model for Separated Turbulent Flows. *AIAA paper*, [78-257], 1978. 77

[12] T. J. Barth. Aspects of Unstructured Grids and Finite-Volume Solvers for the Euler and Navier-Stokes Equations. In *von Karman Institute for Fluid Dynamics, Lecture Series 1994-05*, pages 21–25, Rhode-Saint-Genèse, Belgium, 1994. 32

[13] M. J. Berger and P. Colella. Local adaptive mesh refinement for shock hydrodynamics. *J. Comput. Phys.*, **82**:64–84, 1989. 32

[14] A. Bernard, P. Dupont, J. Foucaut, and M. Stanislas. Decelerating boundary layer: a new scaling and mixing length model. *AIAA J.*, **41**[2]:248–255, 2003. 100

[15] A. Bhattacharya, A. Das, and R. D. Moser. A filtered-wall formulation for large-eddy simulation of wall-bounded turbulence. *Phys. Fluids*, **20**[115104], 2008. 16

[16] J. P. Boris, F. F. Grinstein, E. S. Oran, and R. L. Kolbe. New insights into large eddy simulation. *Fluid Dyn. Res.*, **10**:199–228, 1992. 20

[17] M. Breuer, B. Jaffrézic, and K. Arora. Hybrid LES-RANS technique based on a one-equation near-wall model. *Theor. Comput. Fluid Dyn.*, **22**:157–187, 2008. 114

[18] M. Breuer, B. Jaffrézic, S. Šarić, S. Jakirlić, G. Deng, and O. Chikhaoni. Issues in hybrid LES-RANS and coarse grid LES of separated flows. In *EUROMECH colloquium 469, Large-Eddy Simulation of complex flows*, TU Dresden, Germany, October 6-8, 2005. 114

[19] M. BREUER, B. KNIAZEV, AND M. ABEL, editors. *Development of wall models for LES of separated flows.* Direct and Large-Eddy Simulation VI. Springer, Netherlands, 2006. 10, 15

[20] M. BREUER, B. KNIAZEV, AND M. ABEL. Development of wall models for LES of separated flows using statistical evaluations. *Computers & Fluids*, **36**:817–837, 2007. 10, 114

[21] M. BREUER, N. PELLER, CH. RAPP, AND M. MANHART. Flow over periodic hills - Numerical and experimental study in a wide range of Reynolds numbers. *Computers & Fluids*, **38**:433–457, 2009. 114, 122

[22] M. H. BUSCHMANN AND M. GAD EL HAK. Recent developments in scaling of wall-bounded flows. *Prog. Aerosp. Sci.*, **42**:419–467, 2007. 9

[23] W. H. CABOT. Large-eddy simulations with wall models. *CTR Annu. Res. Briefs*, pages 41–50, 1995. 14

[24] W. H. CABOT. Near-wall models in large-eddy simulations of flow behind a backward-facing step. *CTR Annu. Res. Briefs*, pages 199–210, 1996. 14

[25] W. H. CABOT. Wall models in large eddy simulation of separated flow. *CTR Annu. Res. Briefs*, pages 97–106, 1997. 11, 83

[26] W. H. CABOT AND J. JIMÉNEZ. On wakes and near-wall behavior in coarse large-eddy simulation of channel flow with wall models and second-order finite-difference methods. *CTR Annu. Res. Briefs*, pages 343–354, 1999. 11

[27] W. H. CABOT AND P. MOIN. Approximate wall boundary conditions in the large-eddy simulation of high Reynolds number flows. *Flow Turbul. Combust.*, **63**:269–291, 1999. 11

[28] J. CARLIER AND M. STANISLAS. Experimental study of eddy structures in a turbulent boundary layer using particle image velocimetry. *J. Fluid Mech.*, **535**:143–188, 2005. 9

[29] P. W. CARPENTER, K. L. KUDAR, R. ALI, P. K. SEN, AND C. DAVIES. A deterministic model for the sublayer streaks in turbulent boundary layers for application to flow control. *Phil. Trans. R. Soc. A*, **365**:2419–2441, 2007. 9

[30] P. CATALANO, M. WANG, G. IACCARINO, AND P. MOIN. Numerical simulation of the flow around a circular cylinder at high Reynolds numbers. *Int. J. Heat Fluid Flow*, **24**:463–469, 2003. 126, 127

[31] T. CEBECI. *Turbulence models and their application: efficient numerical methods with computer programs.* Horizons Publishing Inc., 2004. 8

[32] D. R. CHAPMAN. Computational aerodynamics, development and outlook. *AIAA J.*, **17**[12]:1293–1313, 1979. 10

[33] E. F. CHARLTON AND K. G. POWELL. An octree solution to conservation-laws over arbitrary regions (OSCAR). *AIAA paper*, [97-0198], 1997. 32

[34] Z. L. CHEN, A. DEVESA, S. HICKEL, AND N. A. ADAMS. Wall Modelling for Implicit Large Eddy Simulation of Favourable and Adverse Pressure Gradient Flows. In *Progress in wall turbulence: understanding and modeling*, Lille, France, April 21-23, 2009. 55

[35] Z. L. CHEN, A. DEVESA, S. HICKEL, C. STEMMER, AND N. A. ADAMS. A wall model based on simplified thin boundary layer equations for implicit large eddy simulation of turbulent channel flow. In 16th *DGLR Symposium of STAB*, RWTH Aachen University, Germany, 2008. 55

[36] Z. L. CHEN, S. HICKEL, A. DEVESA, J. BERLAND, AND N. A. ADAMS. Wall modeling for implicit large-eddy simulation and immersed-interface methods. 2010. submitted. 55

[37] J. I. CHOI, R. C. OBEROI, J. R. EDWARDS, AND J. A. ROSATI. An immersed boundary method for complex incompressible flows. *J. Comput. Phys.*, **224**:757–784, 2007. 16, 56

[38] F. K. CHOW AND P. MOIN. A further study of numerical errors in large-eddy simulations. *J. Comput. Phys.*, **184**:366–380, 2003. 20

[39] P. Colella, D. T. Graves, B. J. Keen, and D. Modiano. A Cartesian grid embedded boundary method for hyperbolic conservation laws. *J. Comput. Phys.*, **211**:347–366, 2006. 31

[40] A. Cristallo and R. Verzicco. Combined Immersed Boundary/Large-Eddy-Simulations of Incompressible Three Dimensional Complex Flows. *Flow Turbul. Combust.*, **77**:3–26, 2006. 16, 56

[41] L. Davidson and S. Peng. Hybrid LES-RANS modelling: a one equation SGS model combinded with a $k-\omega$ model for predicting recirculating flows. *Int. J. Numer. Meth. Fluids*, **43**:1003–1018, 2003. 15

[42] J. C. del Alamo, J. Jiménez, P. Zandonade, and R. D. Moser. Scaling of the energy spectra of turbulent channels. *J. Fluid Mech.*, **500**:135–144, 2004. x, 66

[43] H. Van der Ven. A family of large eddy simulation (LES) filters with nonuniform filter widths. *Phys. Fluids*, **7**[5]:1171–1172, 1995. 19

[44] J. A. Domaradzkia, Z. Xiao, and P. K. Smolarkiewicz. Effective eddy viscosities in implicit large eddy simulations of turbulent flows. *Phys. Fluids*, **15**[12], 2003. 21

[45] Jae doo Lee. *Development of an efficient viscous approach in a Cartesian grid framework and application to rotor-fuselage interaction.* PhD thesis, Georgia Institute of Technology, 2006. 140

[46] D. Drikakis. Advances in turbulent flow computations using high-resolution methods. *Prog. Aerosp. Sci.*, **39**:405–424, 2003. 21

[47] A. A. Dunca. *Space Averaged Navier-Stokes Equations in the Presence of Walls.* PhD thesis, University of Pittsburgh, 2004. 42

[48] P. A. Durbin and G. Iaccarino. An Approach to Local Refinement of Structured Grids. *J. Comput. Phys.*, **181**:639–653, 2002. 32

[49] E. A. Fadlun, R. Verzicco, P. Orlandi, and J. Mohd-Yusof. Combined Immersed-Boundary Finite-Difference Methods for

Three-Dimensional Complex Flow Simulations. *J. Comput. Phys.*, **161**:35–60, 2000. 16, 31

[50] A. FERRANTE AND S. E. ELGHOBASHI. A robust method for generating inflow conditions for direct simulations of spatially-developing turbulent boundary layers. *J. Comput. Phys.*, **198**:372–387, 2004. 44

[51] R. FRANKE. Scattered data interpolation: Tests of some methods. *Math. Comput.*, **38**:181–200, 1982. 139

[52] J. FRÖHLICH, C. P. MELLEN, AND W. RODI. Highly resolved large-eddy simulation of separated flow in a channel with streamwise periodic constrictions. *J. Fluid Mech.*, **526**:19–66, 2005. xiv, 10, 114, 115, 117, 118, 119, 120

[53] J. FRÖHLICH AND D. VON TERZI. Hybrid LES/RANS methods for the simulation of turbulent flows. *Prog. Aerosp. Sci.*, **44**:349–377, 2008. 7, 15, 114

[54] C. FUREBY AND F. F. GRINSTEIN. Monotonically Integrated Large Eddy Simulation of Free Shear Flows. *AIAA J.*, **37**:544–556, 1999. 20, 21

[55] C. FUREBY AND F. F. GRINSTEIN. Large eddy simulation of high-Reynolds number free and wall-bounded flows. *J. Comput. Phys.*, **181**:68–97, 2002. 21

[56] E. GARNIER, M. MOSSI, P. SAGAUT, AND M. DEVILLE. On the use of shock-capturing schemes for large-eddy simulation. *J. Comput. Phys.*, **153**:273–311, 1999. 21

[57] T. B. GATSKI, C. L. RUMSEY, AND R. MANCEAU. Current trends in modelling research for turbulent aerodynamic flows. *Phil. Trans. R. Soc. A*, **365**:2389–2418, 2007. 4

[58] L. GE AND F. SOTIROPOULOS. A numerical method for solving the 3D unsteady incompressible Navier-Stokes equations in curvilinear domains with complex immersed boundaries. *J. Comput. Phys.*, **225**:1782–1809, 2007. 32

[59] W. K. GEORGE. Is there a universal log law for turbulent wall-bounded flows? *Phil. Trans. R. Soc. A*, **365**:789–806, 2007. 9

[60] S. GHOSAL. An Analysis of Numerical Errors in Large-Eddy Simulations of Turbulence. *J. Comput. Phys.*, **125**:187–206, 1996. 20

[61] S. GHOSAL AND P. MOIN. The basic equations for the large-eddy simulation of turbulent flows in complex geometry. *J. Comput. Phys.*, **118**:24–37, 1995. 19

[62] D. GOLDSTEIN, R. HANDLER, AND L. SIROVICH. Modeling a no-slip flow boundary with an external force field. *J. Comput. Phys.*, **105**:354–366, 1993. 31

[63] F. F. GRINSTEIN AND C. FUREBY. From canonical to complex flows: Recent progress on monotonically integrated LES. *Comp. Sci. Eng.*, **6**:36–49, 2004. 16, 21

[64] F. F. GRINSTEIN, L.G. MARGOLIN, AND W.J. RIDER. *Implicit Large Eddy Simulation*. Cambridge University Press, 2007. 16, 20

[65] G. GRÖTZBACH. *Direct numerical and large eddy simulation of turbulent channel flows*. Encyclopedia of Fluid Mechanics. West Orange NJ, 1987. 13

[66] M. HAHN AND D. DRIKAKIS. Implicit Large-Eddy Simulation of Swept-Wing Flow Using High-Resolution Methods. *AIAA J.*, **47**:618–630, 2009. 21

[67] F. HAMBA. Log-layer mismatch and commutation error in hybrid RANS/LES simulation of channel flow. *Int. J. Heat and Fluid Flow*, **30**:20–31, 2009. 15

[68] S. HICKEL AND N. A. ADAMS. Efficient implementation of nonlinear deconvolution methods for implicit Large-Eddy Simulation. In *High Performance Computing in Science and Engineering*, pages 293–306. Springer, Berlin, 2007. 29, 60

[69] S. HICKEL AND N. A. ADAMS. On implicit subgrid-scale modeling in wall-bounded flows. *Phys. Fluids*, **19**[105106], 2007. 28, 29, 48, 68

[70] S. HICKEL AND N. A. ADAMS. Implicit LES applied to zero-pressure-gradient and adverse-pressure-gradient boundary-layer turbulence. *Int. J. Heat and Fluid Flow*, **29**[3]:626–639, 2008. 29

[71] S. HICKEL, N. A. ADAMS, AND J. A. DOMARADZKI. An adaptive local deconvolution method for implicit LES. *J. Comput. Phys.*, **213**:413–436, 2006. 21, 27, 29

[72] S. HICKEL, N. A. ADAMS, AND N. N. MANSOUR. Implicit subgrid-scale modeling for large-eddy simulation of passive-scalar mixing. *Phys. Fluids*, **19**[095102], 2007. 29

[73] S. HICKEL, T. KEMPE, AND N. A. ADAMS. Implicit large-eddy simulation applied to turbulent channel flow with periodic constrictions. *Theor. Comput. Fluid Dyn.*, **22**:227–242, 2008. 29

[74] S. HICKEL, D. V. TERZI, AND J. FRÖHLICH. An adaptive local deconvolution method for general curvilinear coordinate systems. *Advances in Turbulence XII*, 2009. 38

[75] G. HOFFMAN AND C. BENOCCI. Approximate wall boundary conditions for large-eddy simulations. In R. BENZI, editor, *Advances in Turbulence V*, pages 222–228. Dordrecht, Kluwer, 1995. 54

[76] D.G. HOLMES AND S.D. CONNELL. Solution of the 2D Navier-Stokes Equations on Unstructured Adaptive Grids. *AIAA paper*, [89-1932-CP], 1989. 140

[77] S. HOYAS AND J. JIMÉNEZ. Scaling of the velocity fluctuations in turbulent channels up to Re_τ=2003. *Phys. Fluids*, **18**[011702], 2006. x, xi, 5, 66, 68, 70, 71, 72, 73

[78] X. Y HU, B.C. KHOO, N. A. ADAMS, AND F. L. HUANG. A conservative interface method for compressible flows. *J. Comput. Phys.*, **219**:553–578, 2006. 35

[79] N. Hutchins and I. Marusic. Large-scale influences in near-wall turbulence. *Phil. Trans. R. Soc. A*, **365**:647–664, 2007. 9

[80] A. G. Hutton. The emerging role of large eddy simulation in industrial practice: challenges and opportunities. *Phil. Trans. R. Soc. A*, **367**:2819–2826, 2009. 4

[81] G. Iaccarino and R. Verzicco. Immersed boundary technique for turbulent flow simulations. *Appl. Mech. Rev.*, **56**[3]:331–347, 2003. 16, 30

[82] M. Ilicak, T. M. Özgökme, H. Peters, H. Z. Baumert, and M.Iskandarani. Very large eddy simulation of the Red Sea overflow. *Ocean Modelling*, **20**:183–206, 2008. 7

[83] S. Jakirlić, R. Jester-Züker, and C. Tropea. 9th ERCOFTAC/IAHR/COST workshop on refined flow modeling. Darmstadt University of Technology, Germany, October 4-5 2001. 4, 113

[84] N. Jarrin, S. Benhamadouche, D. Laurence, and R. Prosser. A synthetic-eddy-method for generating inflow conditions for large-eddy simulations. *Int. J. Heat and Fluid Flow*, **27**:585–593, 2006. 45

[85] J. Jeong, F. Hussain, W. Schoppa, and J. Kim. Coherent structures near the wall in a turbulent channel flow. *J. Fluid Mech.*, **332**:185–214, 1997. 6

[86] J. Jiménez. Computing high-Reynolds-number turbulence: will simulations ever replace experiments? *J. Turbul.*, **4**[022], 2003. 4, 6

[87] J. Jiménez, O. Flores, and M. G. Villalba. The large-scale organization of autonomous turbulent wall regions. *CTR Annu. Res. Briefs*, pages 317–327, 2001. 9

[88] J. Jiménez and R. D. Moser. What are we learning from simulating wall turbulence? *Phil. Trans. R. Soc. A*, **365**:715–732, 2007. 9

[89] J. JIMÉNEZ AND C. VASCOL. Approximate lateral boundary conditions for turbulent simulations. *CTR, ARTICLE of the Summer Program*, pages 399–412, 1998. 11

[90] S. JOVIC. An Experimental Study of a Separated/Reattached Flow Behind a Backward-Facing Step. Re_h=37,000. *NASA TM 110384*, 1996. 87

[91] S. JOVIC AND D. M. DRIVER. Backward-Facing Step Measurements at Low Reynolds Number, $Re_h = 5000$. *NASA TM 108807*, 1994. xii, 59, 82, 84, 87, 95

[92] G. KALITZIN, G. MEDIC, G.IACCARINO, AND P. DURBIN. Near-wall behavior of RANS turbulence models and implications for wall functions. *J. Comput. Phys.*, **204**:265–291, 2005. 9

[93] H. J. KALTENBACH, M. FATICA, R. MITTAL, T. S. LUND, AND P. MOIN. Study of flow in a planar asymmetric diffuser using large-eddy simulation. *J. Fluid Mech.*, **390**:151–185, 1999. 44

[94] H. J. KALTENBACHA. A priori testing of wall models for separated flows. *Phys. Fluids*, **15**[10]:3048–3064, 2003. 9

[95] S. KANG, G. IACCARINO, AND P. MOIN F. HAM. Prediction of wall-pressure fluctuation in turbulent flows with an immersed boundary method. *J. Comput. Phys.*, **228**:6753–6772, 2009. 16

[96] S. KANG, G. IACCARINO, AND P. MOIN. Accurate and efficient immersed-boundary interpolations for viscous flows. *CTR Annu. Res. Briefs*, pages 31–43, 2004. 16

[97] A. KEATING AND U. PIOMELLI. A dynamic stochastic forcing method as a wall-layer model for large-eddy simulation. *J. Turbul.*, **7**[12]:1–24, 2006. 15

[98] A. KEATING, U. PIOMELLI, E. BALARAS, AND H. J. KALTENBACH. A priori and a posteriori tests of inflow conditions for large-eddy simulation. *Phys. Fluids*, **16**[12]:4696–4712, 2004. 43, 44, 45

[99] J. KIM, D. KIM, AND H. CHOI. An Immersed-Boundary Finite-Volume Method for Simulations of Flow in Complex Geometries. *J. Comput. Phys.*, **171**:132–150, 2001. 16

[100] M. P. KIRKPATRICK, S. W. ARMFIELD, AND J. H. KENT. A representation of curved boundaries for the solution of the Navier-Stokes equations on a staggered three-dimensional Cartesian grid. *J. Comput. Phys.*, **184**:1–36, 2003. 31

[101] M. KLEIN, A. SADIKI, AND J. JANICKA. A digital filter based generation of inflow data for spatially developing direct numerical or large eddy simulations. *J. Comput. Phys.*, **186**:652–665, 2003. 45

[102] H. KOBAYASHI. The subgrid-scale models based on coherent structures for rotating homogeneous turbulence and turbulent channel flow. *Phys. Fluids*, **17**[045104], 2005. 70, 142

[103] H. KOBAYASHI, F. HAM, AND X. WU. Application of a local SGS model based on coherent structures to complex geometries. *Int. J. Heat and Fluid Flow*, **29**[3]:640–653, 2008. 70, 142

[104] A. G. KRAVCHENKO AND P. MOIN. On the Effect of Numerical Errors in Large Eddy Simulations of Turbulent Flows. *J. Comput. Phys.*, **131**:310–322, 1997. 20

[105] A. G. KRAVCHENKO, P. MOIN, AND R. MOSER. Zonal Embedded Grids for Numerical Simulations of Wall-Bounded Turbulent Flows. *J. Comput. Phys.*, **127**:412–423, 1996. 6

[106] C. DE LANGHE, B. MERCI, AND E. DICK. Very Large Eddy Simulation and RNG Turbulence Models. In *31st AIAA Fluid Dynamics Conference Exhibit*, number AIAA-2001-3041, Anaheim, CA, June 11-14 2001. 7

[107] J. P. LAVAL. Comparison of LES of converging diverging channel flow with DNS. Progress in wall turbulence: understanding and modeling D5.9 WT-090109-TR-LML-1, Laboratoire de Mćanique de Lillee, Lille, France, Jan 2009. xiii, 100, 102, 103, 104, 108, 109

[108] H. Le, P. Moin, and J. Kim. Direct numerical simulation of turbulent flow over a backward-facing step. *J. Fluid Mech.*, **330**:349–374, 1997. 10, 45, 47, 83, 87

[109] S. Lee, S. Lele, and P. Moin. Simulation of spatially evolving compressible turbulence and the application of taylor's hypothesis. *Phys. Fluids A*, **4**:1521–1530, 1992. 45

[110] N. Li, E. Balaras, and U. Piomelli. Inflow conditions for large-eddy simulations of mixing layers. *Phys. Fluids*, **12**[4]:935–938, 2000. 44

[111] N. S. Liu and T. H. Shih. Turbulence modeling for very large-eddy simulation. *AIAA J.*, **44**:687–697, 2006. 7

[112] O. Lödberg, K. Angele, and P. H. Alfredsson1. On the scaling of turbulent separating boundary layers. *Phys. Fluids*, **20**[075104], 2008. 9

[113] T. Lund, X. Wu, and D. Squires. Generation of turbulent inflow data for spatially-developing boundary layer simulations. *J. Comput. Phys.*, **140**:233–258, 1998. 44, 47

[114] S. Majumdar, G. Iaccarino, and P. A. Durbin. RANS solver with adaptive structured boundary non-conforming grids. *CTR Annu. Res. Briefs*, pages 353–366, 2001. 31

[115] R. Manceau, J.P. Bonnet, M.A. Leschziner, and F. Menter. 10th joint ERCOFTAC(SIG-15)/IAHR/QNET-CFD workshop on refined flow modeling. Université de Poitiers, France, October 10-11 2002. 4, 113

[116] N. Marati, C. M. Casciola, and R. Piva. Energy cascade and spatial fluxes in wall turbulence. *J. Fluid Mech.*, **521**:191–215, 2004. 9

[117] M. Marquillie, J. P. Laval, and R. Dolganov. Direct numerical simulation of a separated channel flow with a smooth profile. *J. Turbulence*, **9**[1]:1–23, 2009. 100

[118] I. Marusic, R. Mathis, and N. Hutchins. High Reynolds number effects in wall turbulence. *Int. J. Heat and Fluid Flow*, **31**[3]:418–428, 2010. 9

[119] G. Medic, J. A. Templeton, and G. Kalitzin. A formulation for near-wall RANS/LES coupling. *Int. J. Eng. Sci.*, **44**:1099–1112, 2006. 11

[120] C. P. Mellen, J. Fröhlich, and W. Rodi. Large-eddy simulation of the flow over periodic hills. In M. Deville and R. Owens, editors, *Proceedings of 16th IMACS world congress*, Lausanne, Switzerland, 2000. 113, 114

[121] M. Meyer, A. Devesa, S. Hickel, X. Y. Hu, and N. A. Adams. A Conservative Immersed Interface Method for Large-Eddy Simulation of Incompressible Flows. *J. Comput. Phys.*, **229**:6300–6317, 2010. 16, 31, 32, 34, 38, 40

[122] M. Meyer, S. Hickel, and N. A. Adams. Assessment of Implicit Large-Eddy Simulation with a Conservative Immersed Interface Method for Turbulent Cylinder flow. *Int. J. Heat and Fluid Flow*, **10**[3]:368–377, 2010. 38, 40

[123] R. Mittal and G. Iaccarino. Immersed boundary methods. *Annu. Rev. Fluid Mech.*, **37**:239–261, 2005. 16, 30

[124] B. Mohammadi and G. Puigt. Wall functions in computational fluid mechanics. *Comput. Fluids*, **35**:1108–1115, 2006. 9

[125] J. Mohd-Yusof. Combined immersed-boundary/B-spline methods for simulations of flow in complex geometries. *CTR Annu. Res. Briefs*, pages 317–327, 1997. 16, 31

[126] R. D. Moser, J. Kim, and N. N. Mansour. Direct numerical simulation of turbulent channel flow up to Re_τ=590. *Phys. Fluids*, **11**[4]:943–945, 1999. ix, x, xv, 61, 63, 66, 70, 71, 90, 144

[127] Y. Na and P. Moin. Direct numerical simulation of a separated turbulent boundary layer. *J. Fluid Mech.*, **374**:379–405, 1998. 47

[128] F. Nicoud, J. S. Baggett, P. Moin, and W. Cabot. Large eddy simulation wall-modeling based on suboptimal control theory and linear stochastic estimation. *Phys. Fluids*, **13**[10]:2968–2984, 2001. 11, 12, 14

[129] F. Nicoud, G. Winckelmans, D. Carati, J. Baggett, and W. Cabot. Boundary conditions for LES away from the wall. *CTR, ARTICLE of the Summer Program*, pages 413–422, 1998. 11

[130] N. Nikitin. Spatial periodicity of spatially evolving turbulent flow caused by inflow boundary condition. *Phys. Fluids*, **19**[091703], 2007. 44

[131] N. V. Nikitin, F. Nicoud, B. Wasistho, K. D. Squires, and P. R. Spalart. An approach to wall modeling in large-eddy simulations. *Phys. Fluids*, **12**[9]:1629–1632, 2000. 14, 15

[132] I. Orlansi. A simple boundary condition for unbounded hyperbolic flows. *J. Comput. Phys.*, **21**:251–269, 1976. 47

[133] M. Pamiès, P. É. Weiss, E. Garnier, S. Deck, and P. Sagaut. Generation of synthetic turbulent inflow data for large eddy simulation of spatially evolving wall-bounded flows. *Phys. Fluids*, **21**[045103], 2009. 45

[134] R. L. Panton. Overview of the self-sustaining mechanisms of wall turbulence. *Prog. Aerosp. Sci.*, **37**:341–383, 2001. 6, 9

[135] L. L. Pauley, P. Moin, and W. C. Reynolds. A numerical study of unsteady laminar boundary layer separation. In *Rep.*, number TF-34, Thermosciences Division, Dept. of Mech. Engng, Stanford University., 1986. 47

[136] C. S. Peskin. Flow patterns around heart valves: a numerical method. *J. Comput. Phys.*, **10**:220–52, 1972. 31

[137] U. Piomelli. Large-eddy simulation: achievements and challenges. *Prog. Aerosp. Sci.*, **35**:335–362, 1999. 4

[138] U. Piomelli. Wall-layer models for large eddy simulations. *Prog. Aerosp. Sci.*, **44**:437–446, 2008. 7, 11

[139] U. PIOMELLI AND E. BALARAS. Wall-layer models for Large-Eddy Simulations. *Annu. Rev. Fluid Mech.*, **34**:349–374, 2002. 7, 10

[140] U. PIOMELLI, E. BALARAS, AND A. PASCARELLI. Turbulent structures in accelerating boundary layers. *J. Turbul.*, **1**[1], 2000. 44

[141] U. PIOMELLI, E. BALARAS, H. PASINATO, K. D. SQUIRES, AND P. R. SPALART. The inner-outer layer interface in large-eddy simulations with wall-layer models. *Int. J. Heat and Fluid Flow*, **24**:538–550, 2003. 15

[142] U. PIOMELLI, J. FERZIGER, P. MOIN, AND J. KIM. New approximate boundary conditions for large eddy simulations of wall-bounded flows. *Phys. Fluids A*, **1**[6], 1989. 13

[143] S. B. POPE. *Turbulent Flows*. Cambridge University Press, 2000. ix, 3, 5, 8, 120

[144] L. PRANDTL. Uber Flussigkeits bewegung bei sehr kleiner Reibung. In *Verhaldlg III Int. Math. Kong.*, pages 484–491, Teubner, Heidelberg, 1904. 8

[145] C. RAPP, M. BREUER, M. MANHART, AND N. PELLER. 2D Periodic Hill Flow. *http://qnet.cfms.org.uk*, 2010. xiv, 116, 117, 122, 123

[146] L. F. RICHARDSON. *Weather Prediction by Numerical Process*. Cambridge University Press, 1922. 2

[147] S. K. ROBINSON. An Experimental Search for Near-Wall Boundary Conditions for Large Eddy Simulation. In *AIAA/ASME 3rd Joint Thermophysics, Fluids, Plasma and Heat Transfer Conference*, number AIAA-82-0963, St. Louis, Missouri, June 7-11 1982. 12

[148] R. S. ROGALLO AND P. MOIN. Numerical simulation of turbulent flows. *Annu. Rev. Fluid Mech.*, **16**:99–137, 1984. 7

[149] F. ROMAN, V. ARMENIO, AND J. FRÖHLICH. A simple wall-layer model for large eddy simulation with immersed boundary method. *Phys. Fluids*, **12**[101701], 2009. 16, 57

[150] F. ROMAN, E. NAPOLI, B. MILICI, AND V. ARMENIO. An improved immersed boundary method for curvilinear grids. *Computers & Fluids*, **38**:1510–1527, 2009. 32

[151] S. G. SADDOUGHI AND S. V. VEERAVALI. Local isotropy in turbulent boundary layers at high Reynolds numbers. *J. Fluid Mech.*, **268**:333–372, 1994. ix, 7

[152] P. SAGAUT. *Large Eddy Simulation for Incompressible Flows: An Introduction.* Cambridge University Press, 2005. 4, 20

[153] H. SCHLICHTING. *Boundary-layer theory.* McGraw-Hill Book Company, 1979. 8

[154] U. SCHUMANN. Subgrid-scale model for finite difference simulation of turbulent flows in plane channels and annuli. *J. Comput. Phys.*, **18**:376–404, 1975. 12, 111

[155] S. E. SHERER AND M. R. VISBAL. Multi-resolution implicit large eddy simulations using a high-order overset-grid approach. *Int. J. Numer. Meth. Fluids*, **55**:455–482, 2007. 6

[156] T. H. SHIH, L. A. POVINELLI, AND N. S. LIU. Application of generalized wall function for complex turbulent flows. *J. Turbul.*, **4**[15], 2003. 9, 50

[157] W. C. L. SHIH, C. WANG, D. COLES, AND A. ROSHKO. Experiments on flow past rough circular cylinders at large Reynolds numbers. *J. Wind Eng. Indust. Aerodyn.*, **49**:351–368, 1993. 126

[158] C. W. SHU. Essentially non-oscillatory and weighted essentially non-oscillatory schemes for hyperbolic conservation laws. In *Tech. Rep.*, number 97-65, NASA Langley Research Center, Hampton, VA, 1997. 24, 25

[159] R. L. SIMPSON. A model for the backflow mean velocity profile. *AIAA J.*, **21**[1]:142–143, 1983. 9

[160] R. L. SIMPSON. Aspects of turbulent boundary-layer separation. *Prog. Aerospace Sci.*, **32**:457–521, 1996. 4, 13

[161] D. L. SONDAK AND R. H. PLETCHER. Application of Wall Functions to Generalized Nonorthogonal Curvilinear Coordinate System. *AIAA J.*, **33**[1]:33–41, 1995. 56

[162] P. R. SPALART. Direct simulation of a turbulent boundary layer up to $Re_\theta = 1410$. *J. Fluid Mech.*, **187**:61–98, 1986. 44

[163] P. R. SPALART, W. H. JOU, M. K. STRELETS, AND S. R. ALLMARAS. Comments on the feasibility of LES for wings, and on a hybrid RANS/LES approach. pages 137–148, 1997. 15

[164] P. R. SPALART AND J. H. WATMUFF. Experimental and numerical study of a turbulent boundary layer with pressure gradients. *J. Fluid Mech.*, **249**:337–371, 1993. 44

[165] D. B. SPALDING. A single formula for the law of the wall. *ASME J. Appl. Mech.*, **28**:455–458, 1961. 9, 51

[166] C. G. SPEZIALE. Turbulence modeling for time-dependent RANS and VLES: a review. *AIAA J.*, **36**:173–184, 1998. 7

[167] M. STANISLAS, J. M. FOUCAUT, AND J. KOSTAS. Investigation of near wall turbulence structure of an APG TBL using double SPIV. Technical report, Laboratoire de Mćanique de Lillee, 2008. 100

[168] S. STOLZ AND N. A. ADAMS. An approximate deconvolution procedure for large-eddy simulation. *Phys. Fluids*, **11**[4]:1699–1701, 1999. 16, 21

[169] L. TEMMERMAN, M. HADZIABDIC, M. LESCHZINER, AND K. HANJALIC. A hybrid two-layer URANS-LES approach for large eddy simulation at high Reynolds numbers. *Int. J. Heat and Fluid Flow*, **26**:173–190, 2005. 15

[170] L. TEMMERMAN AND M. A. LESCHZINER. Large-eddy simulation of separated flow in a streamwise periodic channel constriction. In A.LINDBORG, E. JOHANSSON, J. EATON, J. HUMPHREY, N. KASAGI, M. LESCHZINER, AND M. SOMMERFELD, editors, *Second international symposium turbulence and shear flow phenomena*, pages 399–404, Stockholm, Sweden, June 27-29, 2001. 114

[171] L. Temmerman, M. A. Leschziner, C. P. Mellen, and J. Fröhlich. Investigation of wall-function approximations and subgrid-scale models in large-eddy simulation of separated flow in a channel with periodic constrictions. *Int. J. Heat Fluid Flow*, **24**:157–180, 2003. 52, 114

[172] J. A. Templeton, M. Wang, and P. Moin. An efficient wall model for large-eddy simulation based on optimal control theory. *Phys. Fluids*, **18**[025101], 2006. 12, 14

[173] J. A. Templeton, M. Wang, and P. Moin. A predictive wall model for large-eddy simulation based on optimal control techniques. *Phys. Fluids*, **20**[065104], 2008. 12, 14

[174] H. Tennekes and J. L. Lumley. *A First Course in Turbulence*. MIT Press, 1972. 51

[175] F. Tessicini, G. Iaccarino, M. Wang, and R. Verzicco. Wall modeling for large-eddy simulation using an immersed-boundary method. *CTR Annu. Res. Briefs*, pages 181–187, 2002. 16, 56

[176] F. Tessicini, N. Li, and M.A. Leschziner. Large-eddy simulation of three-dimensional flow around a hill-shaped obstruction with a zonal near-wall approximation. *Int. J. Heat and Fluid Flow*, **28**:894–908, 2007. 14

[177] P. G. Tucker and L. Davidson. Zonal κ - ℓ based large eddy simulations. *Comput. Fluids*, **33**:267–287, 2004. 15

[178] S. Šarić, S. Jakirlić, M. Breuer, B. Jaffrézic, G. Deng, and O. Chikhaoni. Evaluation of detached-eddy simulations for predicting the flow over periodic hills. In Eric Cancès and Jean-Frédéric Gerbeau, editors, *ESAIM Proceedings CEMRACS 2005: Computational aeroacoustics and computational fluid dynamics in turbulent flows*, Marseille, France, July 18 - August 26, 2005. 114

[179] S. V. Utyuzhnikov. Generalized wall functions and their application for simulation of turbulent flows. *Int. J. Numer. Meth. Fluids*, **47**:1323–1328, 2005. 9

[180] O. Vasilyev, T. S. Lund, and P. Moin. A general class of commutative filters for LES in complex geometries. *J. Comput. Phys.*, **146**:82–104, 1998. 20

[181] M. Wang and P. Moin. Dynamic wall modeling for large-eddy simulation of complex turbulent flows. *Phys. Fluids*, **14**[7]:2044–2051, 2002. 13, 14, 54

[182] H. Werner and H. Wengle. Large-eddy simulation of turbulent flow over and around a cube in a plate channel. In 8th *Symposium on Turbulent Shear Flows*, pages 155–168, 1991. 9, 13, 52, 53

[183] D. C. Wilcox. *Turbulence Modeling for CFD*. DCW Industries, Inc., 1994. 4

[184] X. Wu and K. D. Squires. Prediction of the three-dimensional turbulent boundary layer over a swept bump. *AIAA J.*, **36**[4]:505–514, 1998. 13

[185] J. Yang and E. Balaras. An embedded-boundary formulation for large-eddy simulation of turbulent flows interacting with moving boundaries. *J. Comput. Phys.*, **215**:12–40, 2006. 31

[186] T. Ye, R. Mittal, H. S. Udaykumar, and W. Shyy. An Accurate Cartesian Grid Method for Viscous Incompressible Flows with Complex Immersed Boundaries. *J. Comput. Phys.*, **156**:209–240, 1999. 31

[187] M. M. Zdravkovich. *Flow Around Circular Cylinders. Fundamentals, vol. 1*. Oxford University Press, 1997. Chapter 6. 126, 127